Control of Lithium-Ion Battery Warm-up from Sub-zero Temperatures

by

Shankar Narayan Mohan

A dissertation submitted in partial fulfillment
of the requirements for the degree of
Doctor of Philosophy
(Electrical Engineering : Systems)
in The University of Michigan
2017

Doctoral Committee:

Professor Anna G. Stefanopoulou, Chair
Assistant Professor Johanna Mathieu
Assistant Research Scientist Jason B. Siegel
Professor Jing Sun
Assistant Professor Ram Vasudevan

ACKNOWLEDGEMENTS

This dissertation is a compendium of my research during my years at the University of Michigan. This work will not have been possible without the friends and acquaintances I've made at this institution. I am particularly indebted to the following individuals.

Had it not been for my advisor Prof. Anna Stefanopoulou, this document would not exist. For having taken a chance on me; her guidance and generosity; indulging in my whims; I thank her. Dr. Jason Siegel, one of the pillars of the Powertrain Control Lab (PCL), has been of immense assistance while performing experiments. In addition, despite having been a sounding-board for my grievances and ideas, he kindly accepted to serve as a member of my dissertation committee. I would like to thank Prof. Ram Vasudevan for the many *protracted* discussions we've had on *obscure* ideas, for stepping-forward to serve on my dissertation committee, and for his general guidance and mentorship. I owe a debt of gratitude to Profs. Jing Sun and Johanna Mathieu for joining my dissertation committee, and for the fruitful encounters that we've shared.

Assistance, in the form of financial support, for the research that I've undertaken was provided by the U.S. Army Tank Automotive Research, Development and Engineering Center. Drs. Yi Ding and Matthew Castanier (TARDEC) have had a significant influence on this work; their routine and thorough feedback has helped ground the problems and methods on the needs of practice. Moreover, during my internship at NEC Laboratories America (Cupetino), my interest in large-scale energy systems was re-kindled via my communications with Ratnesh Sharma, Ali Hooshmand, Seyyed Ali Pourmousavi Kani, and Rakesh Patil.

Needless to say, the years in school would not have been half as enjoyable were it not for the company I shared. I am especially thankful for the collaboration with all members of PCL; especially with Drs. Xinfan Lin, Youngki Kim and Nassim A. Samad. Over the past two years, I have had the opportunity to interact with members of the ROAHM lab; I will cherish the fun times we've spent.

Kathie Wolney, William Lim, Melissa McGeorge, José-Antonio Rubio and Steven Pejuan have been immeasurably helpful in all matters administrative. Their organizational ability and response to calls-for-assistance that have made cruising through school seem easy.

Sometimes, it is good to save the best for last. The English language has not words adequate to do justice to the extent of patience afforded to me by my family. To my parents, brother and sister-in-law, my gratitude and allegiance are eternal.

TABLE OF CONTENTS

CHAPTER

LIST OF FIGURES

Figure

LIST OF TABLES

Table

ABSTRACT

Control of Lithium-Ion Battery Warm-up from Sub-zero Temperatures
by
Shankar Mohan

Chair: Anna G. Stefanopoulou

The archetype of rechargeable technology, Li-ion batteries have over the last decade benefited from improvements in material science through increased energy and power density. Although widely adopted, these batteries suffer from significant performance degradation at low temperatures, posing a challenge for automotive applications, especially during vehicle start-up.

This begs the question: if one was to seek an energy optimal warm-up strategy, how would it look? Moreover, if as much as 22% of reduction in range of electric vehicles is attributable to onboard battery heating systems, would an optimal heating strategy alleviate this energy drain and at what drawback? This thesis addresses these questions. To that end, we pose and solve two energy-optimal warm-up strategies in addition to developing tools that will enable one to make prudent decisions on whether warm-up is feasible if the battery energy state falls too low.

In this dissertation, we address the four main aspects of control design modeling, control, verification and adaptation. There are two primary control strategies that are designed in this dissertation and tools to analyze them are developed. The first warm-up scenario involves a receding horizon optimal control problem whose objective trades-offs increase in battery's temperature by self-heating against energy expended. The shape of battery current is restricted to be bi-directional pulses that charge and discharge the cell at relatively high frequencies via an external capacitor. The optimal control problem solves for the amplitude of the pulse train and the results clarify issues associated with capacitor size, time and lost energy stored. The second control policy is deduced by solving an optimal discharge control problem for the trajectory of power that could self-heat the cell and at the same time feed an external heater whilst minimizing the loss in state of charge.

Batteries inevitably age as they are used and consequently their dynamics also change. Since both proposed methods are model based, the last of part of this dissertation proposes a novel augmented-state-space partitioning technique which can be used to design cascaded nonlinear estimators. Using this partitioning technique, the relative average estimability of the different states of the electrical and thermal model is studied and Dual Extended Kalman Filters are built and validated in simulations.

All the methods developed are demonstrated via a combination of simulation and experiments on Iron Phosphate or Nickel Manganese Cobalt Li-ion battery cell which have high power capability and could be used in replacement of 12V starter batteries or 48V start-stop applications.

CHAPTER I

Introduction

Access to energy, it might as well be a fundamental human right. There is no downplaying the importance and influence of energy in shaping the landscape of society and technology. In the developed and fast developing countries, this tremendous transformation has been fueled by derivatives of fossilised bio-material for the better part of the last century. Since not-too-long in the past, we have recognized that the over-reliance on these non-renewable energy sources can have two main impacts: supply uncertainty and, more importantly, long-term climatic and ecological damage. The world has started to make a move towards alternative energy and efficient systems.

There are two perspectives to the energy market – supply and demand. On the supply side, alternates to fossil fuels such as nuclear, hydro and renewable power sources have attracted notable attention. The most promising class of energy sources in the category of alternate energy sources is renewables. In fact, it has been suggested that Africa could meet all its energy needs using a combination of wind and solar power [4].

The power output of renewables is not consistent; they in general cannot serve base loads. However, they can benefit from being paired with Energy Storage Systems (ESS) to smoothen their power output [5]. Energy storage systems can serve other purposes in the grid because of their fast dynamics; for example, they can be used in frequency regulation and load shifting. Lithium-ion batteries are one of the more recent entrants to the ESS space and are showing much promise [6].

From the demand-side, stringent regulations on emissions, and optimistic goals for fuel economy, have brought vehicular electrification to the head-of-the-line of problems to be addressed in the automotive sector. The basket of electrified vehicles is constituted by various classifications based on the proportion of contribution of battery towards propulsion, and the many topologies of hybrid electric vehicles. Common to every class is the need for an energy storage element. Presently, Lithium-ion battery technology is the darling child of a few industrial sectors.

It is not hard to spot a device that utilizes a Li-ion battery. Most portable personal computing resources and communication systems are powered by Lithium-ion batteries. On a slightly larger scale — nudged by stringent fuel economy standards — more automotive manufacturers are embracing the idea hybrid drive-trains and battery electric vehicles. On a larger scale, the growth of distributed generation sources has seen the genesis of the household energy-reservoir market (ex. Tesla Powerwall). Even the armed forces and the naval fleets are looking favourably at Li-ion batteries as a drop-in replacement for existing Lead acid 6T starter batteries.

With its increasing prevalence, some of the shortcomings of Li-ion batteries are surfacing. Sometimes in rather unpleasant ways. Reports of self-combusting E-Cigarettes, phones, personal transportation devices (hoverboards) and cars, have raised concerns about the quality control of manufacturing processes, and safety and reliability of Li-ion batteries. Battery/device immolation aside, there is the issue of extreme weather performance. It has been reported that Li-ion batteries are less functional in cold weather. Mobile phones discharge quicker and or turn off unexpectedly. Electrified vehicles suffer from reduced effective range, by as much as 40% [7].

1.1 Background of Lithium-ion Batteries

Lithium-ion batteries (Li-ion), first developed at Sony Corporation in 1991, offer superior performance in terms of their energy and power densities than conventional battery technology; and they do so at higher output voltage levels [8–11].

A typical Li-ion cell consists of two electrodes that are separated by a separator; this sandwich is held between current collectors, and the entire layered structure is immersed in an electrolyte bath; Figure 1.1 presents a schematic of a Li-ion battery. The electrodes that constitute a cell are usually graphitic carbon and some other oxide (such as Iron Phosphate). When an electrostatic potential is applied across the terminals, a current flows through the external leads and Li^+ ions flow through the electrolyte. As the battery is charged, this ion flow is towards the anode (graphite); ions intercalate into the graphite lattice; during discharge, the Li^+ ions de-intercalate from the anode and flow to the cathode, where they intercalate. Concomitant with the chemical reactions that occur at each electrode, heat is generated; this generated heat plays a critical role in the material discussed in this dissertation.

The behavior of the Li-ion cell and its life is impacted by the temperature at which it operates. At temperatures above 40 °C, the rate of adverse side-reactions increases; these reactions could result in the break-down of the electrolyte and eventually in thermal run-away, or increase the rate of degradation of battery life [12]. At low temperatures (below 0 °C), the battery operational mechanism encounters a slightly different problem. At low temperatures, the following reasons are believed to be the primary limiting factors: (1) electrolyte conductivity; (2) solid phase diffusion; (3) electrode thickness; (4) and separator porosity. The afore stated reasons all manifest themselves as increased battery resistance.

Recall that inside the Li-ion battery, ion transport is facilitated by the electrolyte. At

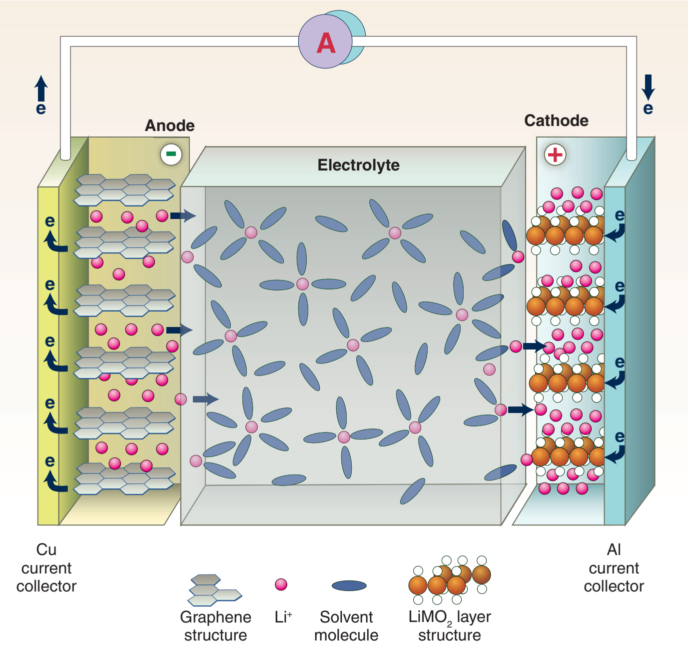

Figure 1.1: Schematic of a Lithium-ion battery. The anode is typically graphitic carbon while the cathode is some oxide (ex. Iron Phosphate, Manganese Oxide). The electrode are separated by a porous medium – the separator. A non-aqueous electrolyte helps transport Li^+ ions between the electrodes. Graphic adopted from [1].

room temperatures, it is often assumed, for simplicity, that the electrolyte has infinite conductivity; i.e. if an ion enters the electrolyte at one electrode, an ion is immediately available for intercalation into the other electrode. The electrolyte's conductivity increases with temperature. At low temperatures, ion mobility is impaired and this is perceived as increased internal resistance.

The contribution of decreased electrolyte conductivity to the total decreased performance of Li-ion batteries is still being debated. At the electrode, electrolyte boundary, the concentrations reach an equilibrium, there is ion exchange between the two mediums. For example, when the battery is being charged, ions move from the electrolyte into the lattice structure of the anode (intercalation). Associated with this ion transfer is a certain potential drop; this is attributed to a charge-transfer resistance. The authors in [13–15] suggest that high charge-transfer resistance is more influential.

The rate at which ions can intercalate into the lattice is related to the diffusion constant of the solid-phase. It has been suggested that the solid-phase diffusion coefficient is temperature dependent, and that the anode is more adverse affected by low temperature operation [16]. At low temperatures, the anode would rather provide than accept Li^+ ions. The decreased ion mobility inside the anode can result in a decrease of local potential at the anode-electrolyte interface. When this happens, solid lithium is deposited on the electrode surface.

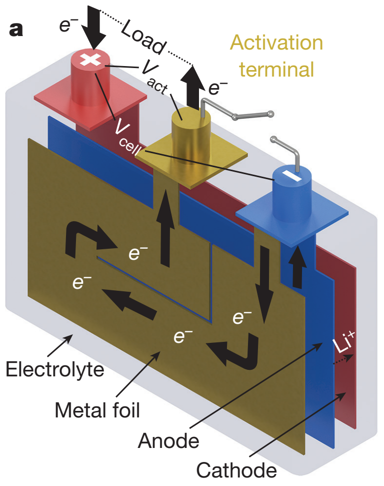

Figure 1.2: Schematic of the novel self-heating battery proposed in [2]. Graphic adopted from [2].

This reduces the amount of available Li^+ in the system and reduces the cell capacity; additionally, it reduces the surface area between the electrode and electrolyte making ion transfer harder [12, 17].

The reduced diffusion rates of the electrodes has another effect; this one is easily observable. Suppose the electrode of the battery are of thickness in excess of the diffusion length at low temperatures. During fast discharge, Li^+ ions will be withdrawn from the regions adjacent to the anode-electrolyte interface at rates quicker than ions get transferred inside the anode. Thus, the interface/surface of the electrode particles can get depleted; this results in a perceived increase in total cell resistance as the voltage drops very quickly.

If one was to use the battery within safe operational voltage limits, the above factors result in a decrease in the maximum current that can be drawn; and hence power output of the battery. As a consequence of this reduction in performance at low temperatures, it is suggested that the range of electric vehicles can be reduced by somewhere between 40% and 60% in cold weather [7, 18]. It should be noted that the increased resistance inside the cell, whilst decreasing the cell's power capability, also helps generate heat.

1.2 Countering the Influence of Cold-temperatures

Earlier methods to improve the low temperature performance of electrochemical energy systems can be categorised as follows: (1) those that alter the energy storage element; (2) those that make it possible for existing elements to perform better. In the former category, [13, 19–21] have explored the development of electrolytes that have high conductivities and are less prone to freezing at low temperatures. In works such as [22–24], the impact of electrode geometry on low temperature behavior of Li-ion cell has been studied.

In the latter category, the primary approach has been to warm-up batteries and electrochemical systems [2, 11, 25–30]. In [11], various methods that convectively heat cells/packs using air and Phase Change Materials (PCM) is surveyed. The use of PCM as a heat source that releases energy when the cell's temperature drops below its melting point was suggested in [31]. The authors of [25] compute and compare the energy requirement to warm NiMH battery packs using both internal and external heating techniques. The authors in [30] use power electronics to place air heaters in parallel (power) to the motors in Electric Vehicles (EVs) to warm the battery pack.

Stuart *et. al.* in [26] present a method of battery warm-up that uses AC currents to effect internal heating. Using high frequency currents has the following advantage: it does not excite the slower dynamics associated with charge-transfer and diffusion, and hence can effect Joule heating without having a detrimental effect of the battery. Muller *et. al.* in [27] present an optimal method to simultaneously warm-up a fuel cell whilst meeting power-flow constraints. The authors in [28] compare a variety of warm-up techniques and conclude that internal warm-up is the most *efficient*.

More recently, Wang *et. al.* in [2] present a novel battery design that incorporates a Nickel foil of a measured resistance inside a Li-ion cell for accelerated warm-up (shown in Fig. 1.2). With this battery, before providing power to external loads, the incorporated foil is connected across the terminals and driven as a low resistance load; this effects internal heating. While this battery structure is decidedly more energy efficient than any others presented before, there are questions about its use in packs that remain unanswered. In this dissertation, we restrict ourselves to batteries that are now commercially available; however, it is an exciting time to be working on means to counter the impact of cold weather using futuristic batteries.

Common to every work described above that seeks to heat batteries-up is the nature of the specification that determines when the battery is warmed-up. Specifically, they all seek to warm batteries until they reach a pre-specified temperature. Now, recognize that batteries are energy storage elements that serve as power sources. Unless there is a direct correlation between power capability and temperature, a more natural specification for warm-up is its power capability – the maximum power that the battery can provide without self-inflicting damage. To determine the power capability of batteries, and hence to assess its dependence on temperature, we need a model of the battery's behavior.

1.3 Battery Models

Every Li-ion battery can be thought of as being constituted by three sub-systems: (1) electrical sub-system, (2) thermal sub-system, (3) aging mechanism; all these sub-systems are coupled and each has been studied in detail in literature.

Models of batteries presented in literature vary in their complexity and fidelity. On the more complex end of the spectrum are electrochemical models that are based on concentration flow; introduced by the pioneering work by Fuller *et. al.* in [32]; arguably the most accurate, albeit hard to parameterize description of the internal workings of Li-ion batteries [33]. This model, and the many derived from the same, assume that each electrode is constituted by numerous identical microscopic particles [34]. The dynamics is described by a family of coupled linear, parabolic and elliptic PDEs, and hence these models are relegated to design optimization and offline studies. Recently, the authors in [23] presented a version of the electrochemical model that is capable of predicting the battery's output at sub-zero temperatures in which the parameters were adapted based on temperature. Despite adopting this adaptation scheme, the performance of the proposed method at current rates above 2C was less than spectacular.

For control applications, the electrochemical model was reduced to a family of ODEs by making simplifying assumptions in [35, 36] to produce the single particle model (SPM), a model assumes that each electrode is a single particle. These models usually have more than 10 states that represent the concentration in different slices of the particle and strike a delicate balance between accuracy and complexity. In [37], the SPM as expanded to include temperature and electrolyte effects. Using this model, it was noted that sub-zero temperatures, the error in predicting the terminal voltage of the battery can be expected to be in excess of 10%.

Towards the lower, and more phenomenological, end of the complexity scale, we find coupled electro-thermal linear parameter varying and equivalent circuit models [38–41]. These models are, at room temperatures, reasonably accurate in capturing the dynamics of the battery. At low temperatures, their performance can be tuned for specific drive-cycles or adapted using online schemes.

1.4 Contributions and Organization

As described above, a viable strategy to improve the low temperature performance of Li-ion batteries is to heat them. According to information collected by fleetcarma, a Canadian fleet management company, about 22% of the reduction in reduction in range of electric vehicles is attributable to onboard battery heating systems [42]. This begs the question: if one was to seek an energy optimal warm-up strategy, how would it look? We seek to answer this question; and to that end, we pose and solve two energy-optimal warm-up strategies.

Suppose you live in a frigid place, drive a Battery Electric Vehicle (BEV), and that your vehicle is parked away from a charging station and home. You seek to estimate the effective range of the long-parked car. To be able to drive the car, the battery has to be warm-ed up; battery warm-up will result in a loss of energy, and by extension, range. Is is possible to assess a priori, how much energy would be required for battery warm-up. Alternatively, if you knew the amount of energy required for the trip, how much would you have to have remaining before warm-up to be able to reach the destination?

In this dissertation, we address the four main aspects of control design – modeling, control, verification and adaptation. There are two primary control strategies that are designed in this dissertation and tools to analyze them are developed. For completeness, each chapter is designed to be self-sufficient.

The methodologies adopted and developed in this dissertation are model based. Usually, when representing a battery in an electric circuit, the go-to model consists of a constant voltage source and a series resistor. While this idealization of the battery may be passable when the battery is not used for high-power applications over prolonged periods at room temperatures, it is inadmissable at sub-zero temperatures. In Chapter V, a simplified control oriented model of the electrical and thermal dynamics of a Lithium-ion (Li-ion) Iron Phosphate ($LiFePO_4$) is presented, parameterized and validated. This model is used in the subsequent chapters, where appropriate.

The second part of Chapter V, and Chapter II are dedicated to addressing the problem of energy-optimal battery warm-up from deep-in-the-cold. The methods described therein differ in terms of the hardware that they assume is available and the constraints that are enforced on the control trajectory. On the flip-side they are similar in that they both ensure that the battery operation strictly adheres to the manufacturer's definition of safe-operation.

In Chapter II, the notion of *productive warm-up* – warming-up such that the battery is capable of doing work after warm-up, is introduced. Unlike Chapter V, Chapter II uses a battery-powered external heater to warm the battery. A temperature terminated energy-optimal warm-up problem is formulated, analysed and numerically solved using pseudospectral collocation. In the interest of practical implementation, feedback, approximate solutions to the optimal control problem are synthesized using newly generated results in reachability verification. The closeness of the approximate solution to the true global optimal solution is evaluated.

The condition utilised to terminate battery warm-up in Chapters V and II were different. In literature, problems on battery warm-up have almost exclusively utilize temperature as the indicator for warm-up. In Chapter III, we seek to answer the question of whether using power as terminal constraint is indeed better than temperature. This comparison is performed by assessing the sensitivity of the energy consumed by the approximate solutions (as deduced in Chapter II) to uncertainties in the parameter values of the electrical sub-dynamics. It is found that with a power capability target specification the cost is more sensitive to parameter uncertainty. Moreover, it is established that under some assumptions, the minimum-time warm-up problem, and problems that use either power or temperature as stopping conditions are equivalent.

The methodology presented in Chapters V–III rely on knowledge of the behavior of the battery; the result in Chapter III alerts for the need for better parameter estimates. Chapter IV presents the derivation of an expression for the power capability of Lithium-ion batteries. In addition, a novel method to partition the augmented-state-space consisting of states and parameters to be estimated is presented. The partitioning is performed by assigning to each dimension of the augmented state-space, a relative significance metric inspired by Principal Component Analysis. Subsequently, each partition is endowed with an estimator, and the estimators are updated in sequence (cascaded arrangement). The proposed cascaded estimator structure is tested through simulations.

In Chapter V, a second power capability is proposed as a more reasonable choice for terminating battery warm-up. Subsequently, a receding horizon optimal control problem whose objective trades-off increase in battery's temperature against energy expended if formulated and solved. The shape of battery current is restricted to be bi-directional pulses at relatively high frequencies to avoid irreparable damage to the battery due to electrochemical side-reactions, and the optimal control problem solves for the amplitude of the pulse train. A bi-directional current mandates the presence of a external power source/sink; it is assumed that an ultra-capacitor serves this role. Through simulations, it is noted that it is possible to reduce the energy consumed during warm-up by ~ 10% as compared to when one draws the maximum admissible voltage limited current until the desired power capability is reached; however, this comes at the expense of increased warm-up time (doubling).

The material presented in this dissertation have been wholly or in-part presented in the following publications:

Journals:

[J1] Kim, Y.; Mohan, S.; Siegel, J.B.; Stefanopoulou, AG.; Ding, Y., *The Estimation of Temperature Distribution in Cylindrical Battery Cells Under Unknown Cooling Conditions*, IEEE Transactions on Control Systems Technology, 2014

[J2] Mohan, S.; Kim, Y.; Siegel, J.B.; Samad, N.A., Stefanopoulou, A.G., *A Phenomenological Model of Bulk Force in a Li-ion battery pack and its Application to State of Charge Estimation*, Journal of The Electrochemical Society, 2014

[J3] Mohan, S.; Kim, Y.; Stefanopoulou, A.G., *Energy-conscious warm-up of Li-ion cells from Sub-zero Temperatures*, IEEE Transactions on Industrial Electronics, 2016

[J4] —, A.G., *Estimating the Power Capability of Li-ion Batteries using Informationally Partitioned Estimators*, IEEE Transactions on Control Systems Technology, 2016

[J5] Mohan, S.; Shia, V.; Vasudevan, R. *A Convex Technique to Compute the Reachable Set of Uncertain Polynomial Hybrid Systems*, Under review

[J6] Mohan, S; Siegel, J.B.; Stefanopoulou, A.G., *Ancillary Results on Energy-Optimal Battery Warm-up*, In preparation

[J7] Mohan, S.; Siegel, J.B.; Stefanopoulou, A.G.; Vasudevan, R., *An Energy-Optimal Warm-up Strategy for Li-ion Batteries and its Approximations*, Under review

CHAPTER II

Optimal Warm-Up Using an External Heater that is Battery-Powered

Chapter V introduced the idea of energy-efficient and used a receding horizon controller to shuttle energy between the battery pack and ultracapacitor pack, with an aim of improving the power capability of Li-ion cells until a pre-specified power threshold was reached using internal heating.

In this chapter, the warm-up of Li-ion batteries in the presence of an integrated (external to the battery) heater until the batteries' temperature reaches a preassigned value is studied. Particularly, the feasibility of energy-optimal warm-up of batteries (energy measured in State of Charge) is investigated. The external heater is powered by the battery pack and transfers heat energy to the battery via a medium such as air; that is, the battery is heated from inside by Joule heating and from outside via convection. This process is assisted by a fan that maintains circulation inside the battery chamber. Figure 2.1 presents a schematic of a 6-cell pack with an internal heater, similar to commercially available packs [53]. It is one such system that is under consideration in this chapter.

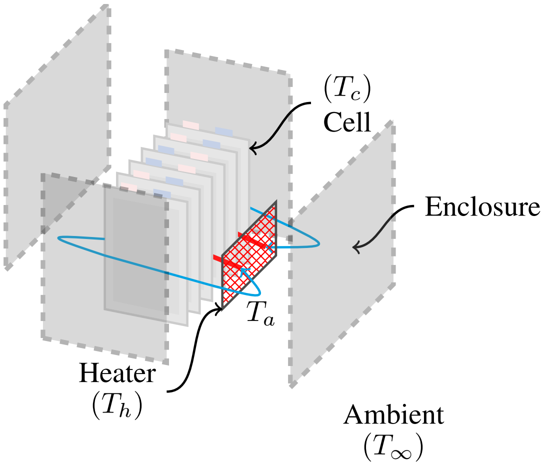

Figure 2.1: An expanded view of a 6-cell pack with a heater and enclosure.

With practical application in mind, there are a few aspects of the problem that deserve emphasis. The dynamics of the battery system is nonlinear because of the strong dependence of the model parameters on states of the system; this is true regardless of the complexity of the model. For example, the ohmic resistance, diffusivity and conductivity of the solid and electrolyte phases depend nonlinearly on temperature [37, 45, 54, 55]. Solving for a *global* feedback optimal policy involving a high-dimensional nonlinear system is non-trivial. Additionally, because of the lack of a high degree of confidence in available models, and the proclivity of batteries, it is a robust/adaptable strategy is sought. In this chapter, two rule-based feedback laws that are approximations of the optimal policy as synthesized.

To derive the approximations of the optimal solutions, we numerically solve the optimal control problem and justify the observations by way of the first order sufficiency conditions. It is observed that *optimal* solution, simplistically, consists of three distinct phases namely constant current (CC), constant voltage (CV) and rest, and the optimal policy is to switch between them. These phases are stitched to construct approximations of the optimal solution; this is performed by identifying the switching conditions between operation phases.

The switching conditions that dictate transition between solution phases is related to the *backwards reachable set*. The backwards reachable set is the set of initial configurations from which the system, under its dynamics, can reach a prescribed terminal set, by a specified time [56, 57]. The backwards reachable can additionally be used to ascertain the proximity of the approximate solution to the true *global* optimal solution. In this chapter, using new tools in algebraic geometry, techniques to estimate the backwards reachable set are developed; details can be found in Appendix A.

This chapter is organized as follows: Section 2.1 presents the models used in this study. Section 2.2 presents the formulation of the optimal control problem, and its analysis to identify a characteristic of the optimal solution. In addition, a methodology to numerically solve the OCP is presented; an example is solved and its solution is interpreted. Section 2.3 uses the derived and observed characteristics of the optimal solution to present two rule based approximations of the optimal policy. In Section 2.4, the quality of the approximate solutions is assessed in terms of the relative size of the domain of initial conditions from which the optimal warm-up problem is feasible. Lastly, Section 2.5 summarizes observations/results and presents directions for future extensions alongside conclusions.

Proofs to the statements that appear in the body of the chapter are presented in Appendix 1.1; and Appendix 1.2 develops the BRS estimation methodologies employed.

2.1 Modelling

In this section, the dynamics of an Iron Phosphate ($LiFePO_4$) cell produced by A123 and classified by size 26650 is modeled by a coupled electro-thermal and is described.

2.1.1 Electrical dynamics

The representation of the electrical sub-system of the battery is constituted by a two-state model, one that corresponds to the State of Charge (z) and the other corresponding to bulk polarization voltage (v_1).

$$\begin{aligned}
\dot{z} &= -\frac{I}{3600 \cdot Q} \\
\dot{v}_1 &= -\frac{v_1}{\tau(T_c)} + \frac{I}{C_1(T_c)} \\
v_t &= v_{oc}(z) - v_1 - I \cdot R_s(T_c),
\end{aligned} \tag{2.1}$$

where I is the current in Amperes, Q is the capacity of the battery in Ampere-hours, temperature dependent real functions τ, C_1, R_s represent the time constant of the overpotential and ohmic drop respectively, and T_c is the battery's temperature. Polynomial approximations of these functions, derived from the data in [58], is presented in Eqn. (2.2).

2.1.2 Thermal dynamics

In this work, we assume that the battery is placed inside an enclosure that has an air re-circulation system built-in (refer Fig. 2.1). Further, a heater is located in the return path of circulated air; this heater is powered by the battery through a power electronic converter.

The thermal dynamics of the cylindrical cell is modeled by a single state representing the linear average temperature across the radius of the cell. This model was derived by reducing the two-state model presented in [41, 59, 60].

The coupled dynamics of all elements in the thermal loop is given by the following:

$$\begin{aligned}
\dot{T}_c &= \alpha_1 \cdot P_{Joule} + \alpha_2 \cdot T_a + \alpha_3 \cdot T_c, \\
\dot{T}_h &= \beta_1 \cdot P_{heater} + \beta_2 \cdot (T_a - T_h), \\
\dot{T}_a &= \gamma_1 \cdot (T_c - T_a) + \gamma_2 \cdot (T_h - T_a) - \gamma_3 \cdot (T_\infty - T_a),
\end{aligned} \tag{2.3}$$

where T_∞, T_a, T_c, T_h are the temperatures of the atmosphere, air inside the enclosure, cell, and the heater respectively. The values of the different parameters in the dynamics are as

---

$$\begin{aligned}
R_s(T_c) &= -6.833 \times 10^{-7} T_c^3 + 5.477 \times 10^{-5} T_c^2 - 1.468 \times 10^{-3} T_c + 0.02421 \\
\tau(T_c) &= 1.088 \times 10^{-5} T_c^4 - 6.002 \times 10^{-4} T_c^3 - 1.961 \times 10^{-3} T_c^2 - 0.116 T_c + 47.57 \\
C_1(T_c) &= -1.186 \times 10^{-3} T_c^3 - 0.144 T_c^2 + 45.63 T_c + 1360 \\
v_{oc}(z) &= 1.528 z^3 - 2.264 z^2 + 1.193 + 3.091 \\
v_{min} &= 2 \text{ V}, Q = 2.3 \text{ Ahrs}, T^c_{max} = 35 \text{ °C}, T^c_{min} = T_{min} = -20 \text{ °C}, T_{max} = 150 \text{ °C} \\
I_{max} &= 25 \text{ A}, v_{max} = 3.6 \text{ V}
\end{aligned} \tag{2.2}$$

Parameter	α_1	α_2	α_3	β_1
Value	0.0214	0.0035	−0.0029	0.2331
Parameter	β_2	γ_1	γ_2	γ_3
Value	-0.1166	-4.6913	-7.1073	variable

Table 2.1: Parameters of the thermal model

listed in Tab. 2.1. Lastly, the power terms in the dynamics are defined as:

$$P_{Joule} = I^2 \cdot R_s(T_c) + v_1^2 \frac{C_1(T_c)}{\tau(T_c)}, \tag{2.4a}$$

$$P_{heater} = v_t \cdot I. \tag{2.4b}$$

Note that the equation of P_{Joule} consists of two terms – Ohmic heating $(I^2 R_s)$ and heating because of built-in polarization $(v_1^2 C_1/\tau)$. At low temperatures, based on the parameters in Eqn. 2.2, the time constant of the bulk polarization dynamics and the its maximum achievable voltage are larger. In a physics based model, this bulk polarization reflects the impact of electrolyte and solid-phase over-potentials, and these build-up significantly at low temperatures [55]. Thus, low temperature operation results in the build-up of bulk polarization which in turn generates significant heat.

We ignore the impact of entropic heating from the expression for the following two reasons: (1) for large currents, the contribution of Ohmic and polarization based heating eclipses that of based on entropy; (2) the functional representation of entropic heating is nonlinear and adds to the complexity of the problem without being significant.

Observe that in the model under consideration, the ambient/atmospheric temperature affects the dynamics of only the air inside the enclosure. The material of the encasement affects the conductive losses between T_a and T_∞, and is a parameter whose influence on solutions will be studied in the ensuing presentation. It should be noted that despite assuming that a fan is present in the thermal loop—to enable better convective transfer of heat—the power delivered to the same is not explicitly modeled.

2.2 Problem, Analysis and Numerical Solution

In this section, the optimal control problem is formulated and analyzed to identify characteristics of the optimal policy. Subsequently, the problem is numerically solved for an example and the results are interpreted.

2.2.1 The optimal control problem

The objective of this chapter is to determine an energy-optimal warm-up (to a pre-specified temperature) strategy for batteries from sub-zero temperatures, without violating operating constraints. In the ensuing presentation, the mathematical formulation of the problem considered in the remainder of this paper is presented.

$$\begin{aligned}
&\min_{I \in L^2([0,t_f])} z(t_0) - z(t_f) && (OCP) \quad (2.5a)\\
&\text{st.}\, Eqns.\ (2.1) - (2.4), && (2.5b)\\
&\quad I(t) \in [0,\, I_{max}], && \forall t \in [0,\, t_f] \quad (2.5c)\\
&\quad v_t(t) \in [v_{min},\, v_{max}], && \forall t \in [0,\, t_f] \quad (2.5d)\\
&\quad T_c(t) \in [T^c_{min}, T^c_{max}], && \forall t \in [0,\, t_f] \quad (2.5e)\\
&\quad T_h(t), T_a(t) \in [T_{min}, T_{max}], && \forall t \in [0,\, t_f] \quad (2.5f)\\
&\quad x(t_0) = x_0, && (2.5g)\\
&\quad T_c(t_f) = T_{des}, && (2.5h)\\
&\quad t_f = t_{max}, && (2.5i)\\
&\quad z(t_f) \geq z_{limit}, && (2.5j)
\end{aligned}$$

where $I : [0, t_f] \to [0, I_{max}]$, $x = [z,\, v_1,\, T_c,\, T_h,\, T_a]'$; T_{des} is the desired cell temperature set-point; I_{max} is the maximum discharge current; and v_{min} and v_{max} are the minimum and maximum terminal voltages of the battery.

Herein, energy is measured in terms of SOC, and hence the objective function in Eqn. (2.5a) represents the energy expended over the period $[0, t_f]$, where t_f is the maximum time for warm-up as defined by the constraint in Eqn. (3.14). Equations (2.5c) & (2.5d) enforce constraints on the current and terminal voltage as specified by the manufacturer's specifications. Observe that in this case, the current is stipulated to be discharging in nature due to the lack of an external energy source (Eqn. (2.5c)). Additionally, the temperatures of the battery, heater and the air inside the enclosure are restricted in the interest of safety as depicted in Eqns. (2.5f). Finally, the constraint in Eqn. (2.5h) enforces, as required, a terminal state constraint on the battery temperature.

Serving as a power source, the battery is an energy storage device; and battery warm-up consumes energy (measured in SOC). If the battery is able to perform work after warm-up; i.e. if there is adequate energy remaining, the warm-up is deemed as having been *productive*. Suppose the minimum energy required at the end of warm-up is z_{limit} and that $I^* : [0, t_f] \to [0, I_{max}]$ is an optimal solution to (OCP), and $z^* : [0, t_f] \to [0, 1]$ is the resulting optimal SOC trajectory; then determining the feasibility of *productive warm-up* is equivalent to checking the condition $z^*(t_f) \geq z_{limit}$. In (OCP), the constraint enforced in Eqn. (2.5j) serves this purpose. Problem (OCP) returns infeasible when *productive warm-up* is infeasible, otherwise returning the optimal warm-up policy.

2.2.2 Numerical solution

In this section, the optimal control problem (OCP) presented in Sec. 2.2.1 is numerically solved for some feasible initial system configuration. The OCP under consideration is nonlinear in dynamics (parameters are non-linear functions of temperature) and constraints (terminal voltage is a nonlinear function of SOC) and are not amenable to solve analytically. Additionally, since the dynamics has five states and one control, the use of Dynamic Programming approach is not computationally tractable. Alternatively, one could employ the technique developed in [61] to derive a polynomial approximation of the global optimal solution.

In this section, we use pseudospectral collocation[1] to solve the OCPs (non-hybridized) using an off-the-shelf solver (IPOPT) using GPOPS2 as the problem parser [63].

To investigate the performance of the pseudospectral method, the following example is solved using both Dynamic Programming (DP) and pseudospectral methods.

Example II.1. Warm-up the battery in Sec. 2.1 when it is initially in thermal (with the atmosphere) and electric equilibrium, in an un-insulated enclosure with the atmosphere at -20 °C. The desired terminal temperature is 5 °C, and the battery initial SOC is 0.6.

To solve the DP version of (OCP) in Sec. 2.1, in the interest of computation time and memory, the model of the system is simplified. As the battery under consideration is a Iron Phosphate cell which has a flat OCV curve, the change in terminal voltage with SOC is insignificant in the middling SOCs; for this problem, as along as the SOC-state remains in [0.4,0.6], it is fair to assume that the OCV is constant. In the model of the battery, the SOC-state impacts only the OCV; with the above assumption, the SOC-state is dropped.

In addition, it is assumed that since the enclosure is un-insulated, the air temperature is identical to that of the atmosphere; i.e. the states corresponding to T_a and T_h can be dropped. The final model employed only has two states: v_1 and T_c. Using a 1001×1001 uniform grid of $[0,1] \times [-20,5]$, and a discreteized grid with 151 points for the space of controls ($[0,25]$), the optimal solution was computed on a computer with four Intel Xeon E7-8867V4 processors and 1TB of RAM, and is depicted in Fig. 2.2.

The solution using the pseudospectral method was computed without making reductions to the size of the problem (i.e. with five states) on a computer with an Intel Xeon E5-2660v3 processor and 48GB of RAM.

Comparing the '*optimal*' policy and state trajectories three things are evident: (1) The shape of the optimal solutions are almost identical; (2) the DP is marginally more efficient—as is to be expected—than the pseudospectral method with the energy consumed

---

[1] Pseudospectral optimal control is an approximate method for solving optimal control problems in which the state trajectory is approximated by polynomials. Typically, Lagrange polynomials. The decision variables in this approach is the value of states and control at discrete node points (in the time domain). Under certain assumptions on the dynamics of the system and the problem description, these approximations converge to the true solution. See [62] for a concise introduction to this approach.

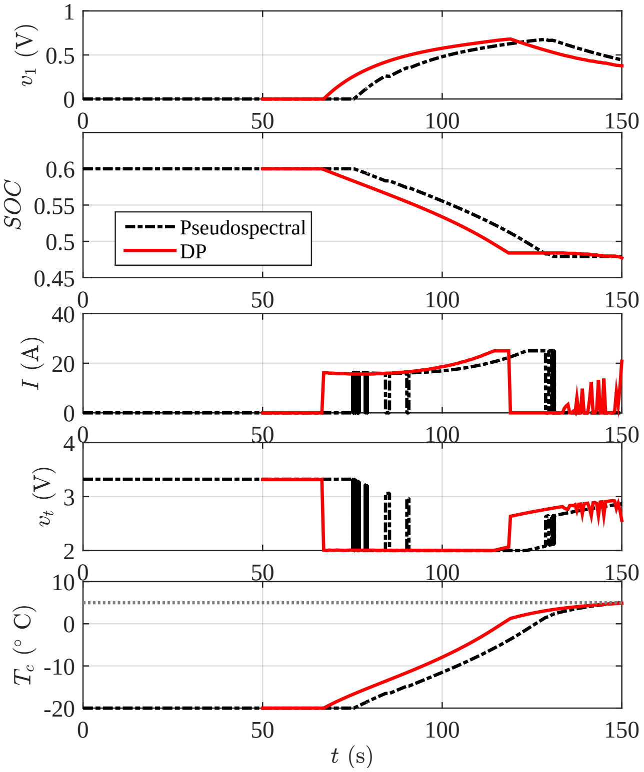

Figure 2.2: A comparison of the solutions to the warm-up problem as obtained by using pseudospectral collocation and dynamic programming.

being 0.004 less; (3) the pseudospectral method is more computationally efficient. Using a time horizon of 100 seconds with 10 Hz temporal discretization[2], it took about eight hours to produce the result. The pseudospectral method took ~10 mins to produce the result.

Given that the pseudospectral method retains the key characteristics of the solution, in the remainder of this chapter, we utilize this method to approximate the optimal solution.

Example II.2. Determine the optimal trajectory of current that consumes the least energy (in SOC) and is capable of increasing the battery's temperature (in thermal equilibrium with the air/heater/atmosphere and initial SOC, 0.6) from −20 °C to 20 °C within 150 s such that the SOC after warm-up is greater than 0.35.

Figures 2.3 and 2.4 provide the results of solving and simulating the model for this example when the values of $\gamma_3 \in \{0, 30\}$. Recall that when γ_3 increases, the losses to the atmosphere increases; i.e. when $\gamma_3 = 0$, the battery enclosure is insulated from the atmosphere and when $\gamma_3 = 30$, the enclosure is a medium through which heat is lost to the atmosphere. Other constraints are set as provided in Eqn. (2.2). From Fig. 2.3, it is noted that the optimal current attains, at each instant, one of either the maximum or minimum

---

[2] Note that the trajectory of SOC as resulting from DP, as shown in Fig. 2.2, was deduced using Coulomb Counting assuming that the initial SOC was as provided in the given data.

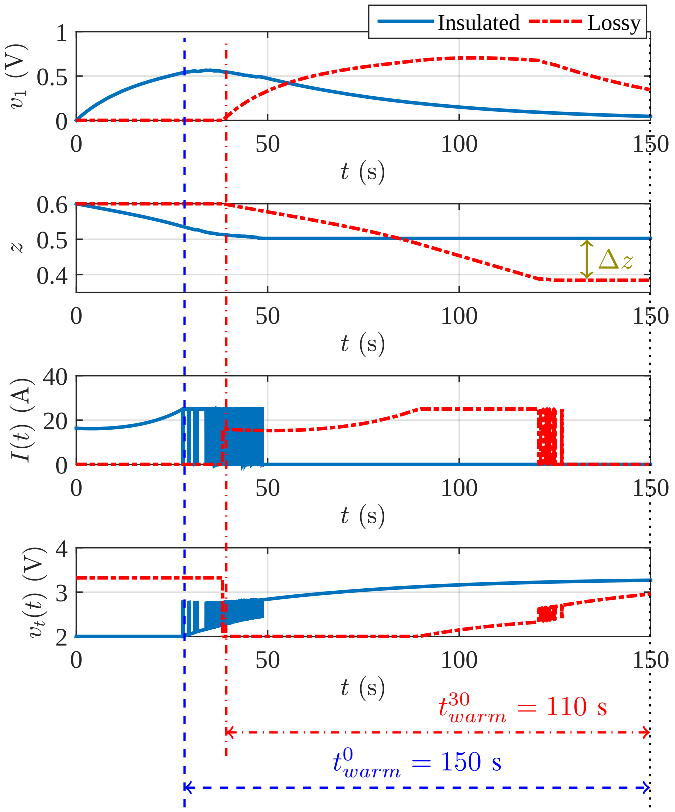

Figure 2.3: Trajectories of states and output of the electrical subsystem as a consequence of applying the optimal policy; insulated ($\gamma_3 = 0$), lossy ($\gamma_3 = 30$). Observe that the optimal policy has three distinct phases – constant voltage, constant current and rest.

admissible current. This results in the solution resembling a sequence of constant voltage (CV), constant current (CC) and rest phases.

The observed rest phase can be justified as follows. Working backwards from the terminal time, the rest phase that is observed is thought to be in place to exploit the built-up polarization inside the battery. Recall that the expression for heat generation in Eqn. (2.4a) includes the term v_1^2/R_1; when the value of heat generated in the R-C pair exceeds that of the heat lost to air, the optimal decision is to set $I = 0$.

The switching pattern observed in the optimal current can be explained in three ways – (1) the high frequency switching serves as a PWM sequence that essentially regulates the root-mean-square current to a certain value that is not an extreme point of the set of admissible control values without taking that value explicitly; (2) the size of mesh intervals and/or the tolerance of the solver is not adequately tight; (3) some state constraint is being violated. Based on the analysis presented earlier in this section, it is suggested that possibility (1) can be ruled-out. In Fig. 2.3, when the $\gamma_3 = 0$, the heater's temperature T_h reaches a maximum of ~ 150° C, the boundary of the state constraint; by comparing Figs. 2.3

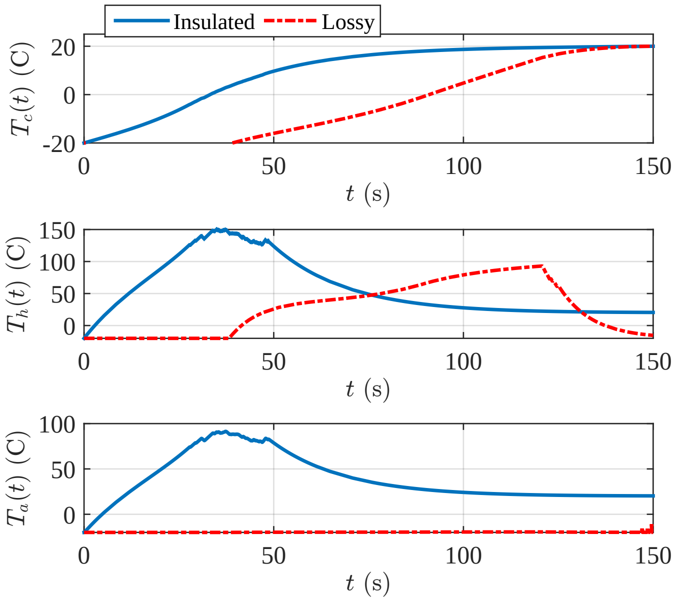

Figure 2.4: Trajectories of states and output of the thermal subsystem as a consequence of applying the optimal policy; insulated ($\gamma_3 = 0$), lossy ($\gamma_3 = 30$)

and 2.4 around the time when the heater temperature hits its constraint, it is indeed noted that the switching behavior is pronounced. Thus, it is suggested that the switching observed in the trajectory of current corresponding to the case when $\gamma_3 = 30$ (lossy) is not because of any state constraint being violated, and could be an artifice of the numerical method employed.

Figures 2.3 and 2.4 also highlight the influence of losses to the atmosphere through conduction losses. If the air-path is perfectly insulated ($\gamma_3 = 0$), then the optimal solution includes a rest phase following what appears to be CV-CC phases until the polarization voltage reduces to zero and the heater, air and cell are at thermal equilibrium at the desired temperature. On the other hand, if the air return path is made of a relatively highly conductive material such as aluminium, then the heat generated in the heater and transferred to air is wicked by the cold-air outside and the heating mechanism becomes ineffective. This particular case devolves into the standalone warm-up case discussed in [58].

In Fig. 2.3, the duration of warm-up, $t_{warm}^{\gamma_3}$—defined as the time duration between the first instance when current is drawn and 150 s—when the loss coefficient is γ_3, is shown for the two values of γ_3. Comparing the resultant trajectories for the two values of γ_3, observe that t_{warm}^{30} is shorter than t_{warm}^{0}, and that the rest phases following the CC phase is shorter when $\gamma_3 = 30$. The observation about the rest phase can be explained by recalling the previous discussion on the net heat generation in the cell being zero at $t = 150$ s; this can also be used to explain the rest before the CV phase. Secondly, observe that as a consequence of an increase in the value of γ_3, the SOC lost during warm-up increases by 11% (true),

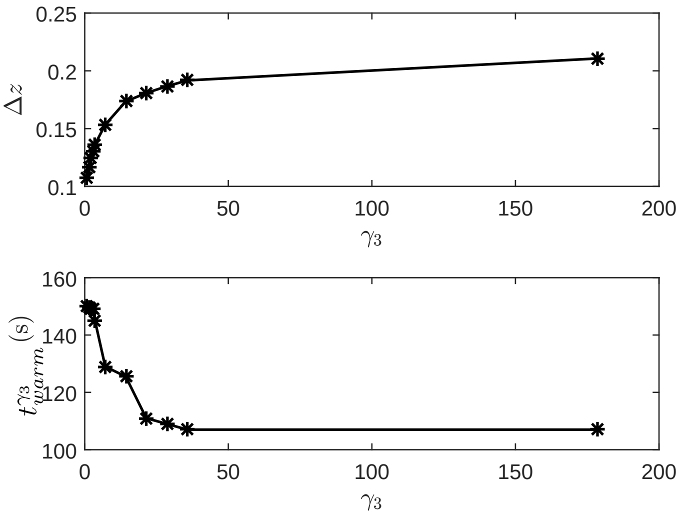

Figure 2.5: Impact of changes to the value of γ_3 on the total SOC lost and the time for warm-up, T_{warm}. As the value of the loss coefficient increases, observe that the energy expended increases and the warm-up time decreases.

and the terminal SOC now is 39%; i.e. increased conduction losses increases the energy consumed during warm-up, as is to be expected.

To highlight the influence of conductive losses, Fig. 2.5 collates key metrics that can be used to study their influence on loss in SOC during warm-up and warm-up time $t_{warm}^{\gamma_3}$. Note that as γ_3 increases, the total loss in SOC (read as energy) during warm-up increases to reach an asymptote. Associated with this increasing value of γ_3, the duration of warm-up decreases; this observation is in line with our expectation as elucidated in the preceding discussion on the rest phase.

2.2.3 Generalization

In the previous section, it was noted that the trajectory of the optimal policy has a distinct shape regardless of the value of the loss coefficient. This characteristic is not unique to the chosen initial condition. The following result establishes that the optimal policy involves either drawing the maximum or minimum admissible current at every instant.

Theorem II.3. *The current trajectory that is optimal with respect to* (OCP) *takes an extreme value of the admissible set at every instant. That is,*

$$I^*(t) \in \left\{0, \min\left\{I_{max}, \frac{v_{oc}(z) - v_1 - v_{min}}{R_s(T_c)}\right\}\right\} \tag{2.6}$$

To summarize, the fundamental characteristic that is shared by the optimal solutions to (OCP) is the following: (1) the optimal current attains only extreme values from the admissible set at any instance; (2) the optimal solution transitions through what could be approximated by a Constant Voltage (CV) and Constant Current (CC) phases; (3) the optimal solution includes a period of rest—the duration of which depends on the loss coefficient—towards the end of warm-up. These observations will be leveraged in the subsequent section to derive approximate solutions to optimal warm-up problem which can be implemented without the need for extensive computation.

Remark II.4. Recall that in the mathematical formulation of (OCP), the explicit constraints on I are independent of temperature. Relaxing this constraint to allow for a temperature dependent current constraint is not expected to change the primary deductions about the optimal solution.

2.3 Synthesizing Approximate Solutions

In Sec. 2.2, the optimal control problem (OCP) was solved numerically and it was noted that the energy-optimal policy resembles a sequence of phases, although not perfectly. To be able to apply the *exact* optimal solution in practice, one would need to solve (OCP) first to determine the *exact* policy, an action that is computationally intensive. To solve Example II.2, it takes ~ 9 mins on a computer with an Intel Xeon E5-1620 processor and 48GB of RAM. Alternatively, one could employ a receding horizon controller similar to that employed in [58], or use a rule-based feedback control. In this section, we first present two rule-based approximations of the optimal solution by leveraging our observations in Sec. 2.2. Subsequently, the performance of these approximations will be compared using an example.

2.3.1 Approximation one: CV-CC

The optimal solution to (OCP), as deduced in Sec. 2.2 appears to be comprised of three phases: constant voltage (CV), constant current (CC) and rest. As a recap, the fundamental reason for the optimal solution to exhibit the CV-CC is that the optimal current at each instance takes only extreme values (Theorem II.3). The extreme values of current correspond to the define the different operational phases. The CV phase occurs when the maximum admissible current I_{admit} defined

$$I_{admit} = \min\left\{\frac{v_{oc}(z) - v_1 - v_{min}}{R_c(T_c)}, I_{max}\right\} \tag{2.7}$$

is less than I_{max}. During the CC portion, $I_{admit} = I_{max}$. We term the period of prolonged rest that occur almost exclusively at the end of the warm-up phase and is in place to make use of the heat-generating built-up internal polarization, as the rest phase.

Determining if the solution should switch between CV and CC is easy since it involves the computation of I_{admit} using an algebraic equation; it can be done instantaneously. Thus

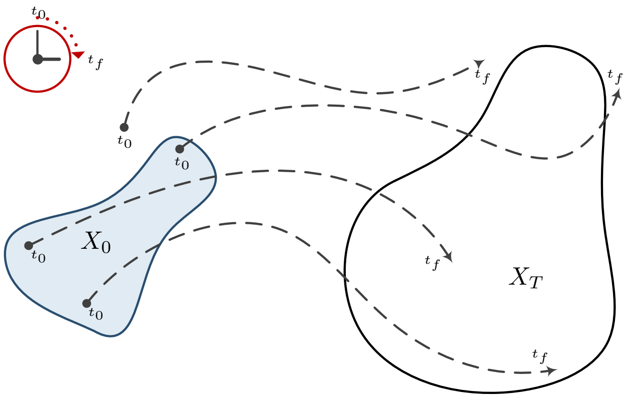

Figure 2.6: An illustration of the concept of backwards reachable set.

a rule for the CV and CC phases is established. Thus, a first approximation of the *exact* optimal solution is one that consists of the CV and CC phases.

2.3.2 Approximation two: CV-CC-rest

The second approximation differs from the first in that it includes the rest phase. Without a self-evident means to analytically compute the condition to switch into the rest phase (henceforth termed the *rest condition*), this section approximates the *rest condition* by solving an auxiliary optimization problem.

The *rest condition* is an expression that is satisfied at the instant after which the optimal current is identically zero. Stated differently, the *rest condition* can be interpreted as being related to the boundary of the set of state initial-conditions from which the system dynamics will be self-driven to reach the desired terminal battery temperature. Thus, the problem of identifying the rest condition is equivalent to a backwards reachable set (BRS) identification problem as shown in the following result.

Lemma II.5. *The description of the boundary of the time-limited free-time backwards reachable set defined as below can serve as the rest condition.*

Definition II.6 (The *tBRS*)**.** The time-limited, free-time backwards reachable set of X_T satisfies

$$\begin{aligned} X_0^r = \{x_0 \in X \mid \exists \zeta : [0, t_f] \xrightarrow{\text{dynamics}} X,\, \zeta(0) = x_0, \\ \exists \tau \in [0, t_f],\, \zeta(\tau) \in X_T\}, \end{aligned} \tag{2.8}$$

where $x = [z, v_1, T_c, T_a, T_h]'$, X is the state-space and ζ is a state trajectory that satisfies the dynamics almost everywhere.

The *best* rest condition is the one that defines the boundary of the *largest* such X_0^r.

Proof. Follows from definition. ☐

To better understand the definition of X_0^r, refer to Fig. 2.6 for an illustration. Suppose we are given a dynamical system and a set X_T. The *tBRS* is the set of initial conditions of the system from which *all* resulting trajectories pass through X_T at some time $\tau(x_0)$ before $t = t_f$. In Fig. 2.6, the set X_0^r is the *tBRS* and the dot-dashed lines are state trajectories. Recognize that not all trajectories that begin in X_0^r are within X_T at $t = t_f$; there is at least one trajectory that leaves X_T and that is admissible by definition. The *tBRS* is *time-limited* because $\tau \le t_f$, but is also *free-time* because τ is free to take any value less than t_f.

Let us define X_T as the set with $T_c \ge T_{des}$ and the other states taking all admissible values. Under the drift dynamics (with no current), X_0^r is the set of system configurations that are guaranteed to reach the desired temperature during the rest phase. Lemma II.5 asserts that the rest condition is the description of ∂X_0^r.

In the following section, the intuition behind the method employed to estimate the rest-condition is presented; for more details, refer to Appendix 1.2.

2.3.2.1 Identifying the rest condition

Estimating the backwards reachable set (BRS) is a well studied problem. The more common implementations use level-set methods [64], viability theory [65], and Zubov's approach [66] amongst others. These techniques usually require either discretizing the state space to use Hamilton-Jacobi equations (curse of dimensionality), solving Bilinear Matrix Inequalities (BMIs) (hard to solve) or making conservative approximations (quality of estimate not guaranteed). More recently, a new approach to solve such problems was proposed in [57]. This method leverages recent results in algebraic geometry and measure theory to generate a sequence of Semi-Definite Programs whose solutions converge, and approximate the BRS. Since such problems are convex, global optimality can be guaranteed. In this chapter, this latter approach is built-upon to estimate the *tBRS*.

The key idea in the adopted estimation methodology is the following. We seek to find functions v and w that satisfy:

1. $\frac{\partial v}{\partial t} + \frac{\partial v}{\partial x} f \le 0$, $\forall (t, x) \in [0, t_f] \times X$
2. $v(t, x) \ge 0$, $\forall (t, x) \in [0, t_f] \times X_T$
3. $v(0, x) - w(x) - 1 \ge 0$, $\forall (t, x) \in [0, t_f] \times X$
4. $w \ge 0$, $\forall x \in X$

where $v \in C^1([0, t_f] \times X)$, $w \in C([0, t_f])$ and f is the dynamics of the system. Note that a v that satisfies the above conditions is like a Lyapunov function. Say $x_0 \in X_0^r$, then by the fundamental theorem of calculus

$$0 \le v(\tau, x(\tau)) = v(0, x_0) + \int_0^\tau \frac{\partial v}{\partial t} + \frac{\partial v}{\partial x} f \, dt \tag{2.9}$$

$$\le v(0, x_0) \le w(x_0) - 1. \tag{2.10}$$

Since the above inequality is true for all $x_0 \in X_0^r$, one could use w to estimate X_0^r. More more information on how to arrive at these requirements and additional constraints, refer to Appendix A.

2.3.2.2 An example

In the previous section, an overview of the technique employed to estimate X_0^r and the rest condition was presented. We now present an example that will serve as the platform on which the approximations will be compared.

Example II.7. Suppose a battery that is in thermal equilibrium with the atmosphere which is at $T_\infty = -10$ °C, that $\gamma_3 = 30$, and the desired terminal temperature $T_{des} = 20$ °C. Let the initial SOC be $z = 0.6$, the total warm-up time $t_f = 150$ s, and the maximum duration of the rest-phase be 90 seconds (roughly the average time constant of the R-C pair). Additionally, it is required that the battery retain 20% SOC after warm-up.

Figure 2.7 depicts the state trajectories that result from applying the two approximations delineated in this section. Observe that as a result of adding the terminal rest-phase, the energy consumed during warm-up decreases by ~ 9% [3]; however, the time for warm-up increases by ~ 10 s. That is, including the rest phase can drive the cost of the problem lower, and hence is closer to the true optimal solution.

The rest condition that was used to characterize the second approximate solution was derived by using degree 20 approximations for the functions v and w introduced above. The problem was parsed using the SPOTLESS toolbox and was solved using MOSEK on a computer that with an Intel® Xeon® E5-2660 v3 processor and 128 GB of RAM. The computation time using MOSEK 8 (beta) was ~ 200 s.

In this example, since the value of γ_3 is large, the impact of the heater on the battery's thermal dynamics is negligible; thus, the projection of the set $\hat{X}_0^r$ onto the $T_c - v_1$ space is depicted as being filled in gray in Fig. 2.8. The rest condition is shown in blue.

To demonstrate that $\hat{X}_0^r$ is a subset of the *tBRS*, a few initial conditions are selected from $\hat{X}_0^r$ and forward simulated. The inset in Fig. 2.8 traces the trajectory of the state

---

[3] Savings are computed according to

$$\text{saving } \% = 100 \times \frac{|z^1(\tau) - z^2(\tau)|}{z^1(0) - z^1(\tau)}, \tag{2.11}$$

where z^1 and z^2 are the SOC trajectories resulting from applying the CV-CC and CV-CC-rest approximations.

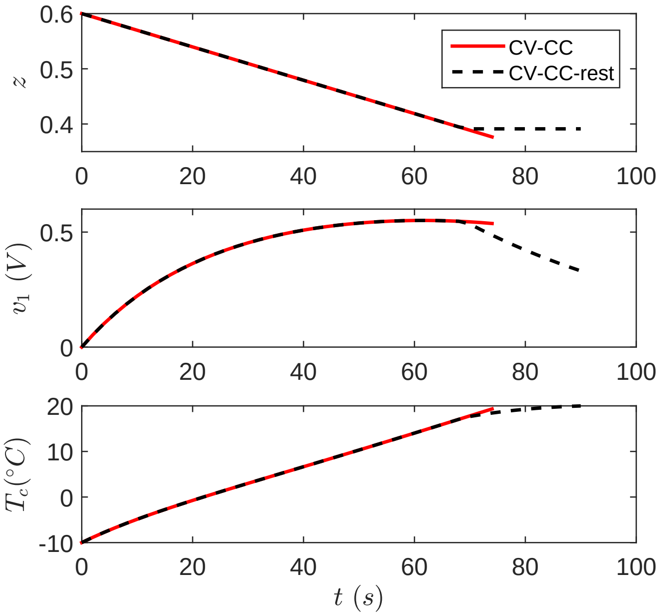

Figure 2.7: Simulated trajectories of the battery states using the two approximations of the optimal solution when $T_c(0) = -10\ °C$, $z(0) = 0.6$, $\gamma_3 = 30$: CV-CC (red dashed), CV-CC-rest (solid black). Notice that while the trajectory corresponding to CV-CC reaches the desired temperature earlier, it consumes ~ 9% more energy than that associated with CV-CC-rest.

trajectories on the phase-plane with the blue • s denoting the initial condition and the green × s, the terminal state. Notice that all trajectories that begin in $\hat{X}_0^r$, be they in the interior or on the boundary, reach the desired terminal temperature $T_{des} = 20$ °C; in fact, the boundary of $\hat{X}_0^r$ that is in the interior of X is the state trajectory of an initial condition.

In the next section, the proximity of each of the above approximations to the true optimal will be qualitatively assessed by comparing the sizes of the respective domains where the (OCP) is feasible.

Remark II.8. In the rest phase, as the current is identically equal to zero; i.e. SOC of the battery does not change. That is, it is not necessary to consider this state as a part of the problem of identifying X_0^r; this saves computation time.

Remark II.9. Recall that while the CV-CC method can be applied without any off-line computation, the CV-CC-rest approximation may require offline computation (to compute the rest condition). Additionally, an accurate description of the dynamics of the system is required for the computed the rest condition to be truly closer to the optimal solution. However, if some information about the uncertainty is known, then a probabilistically robust rest condition can be computed by extending the techniques employed in [49, 52, 67].

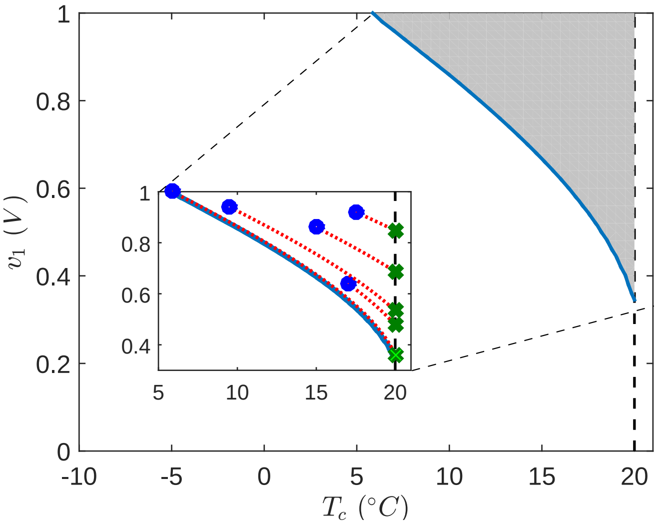

Figure 2.8: An example of the switching surface into the rest phase. The blue curve partitions the space such that on the right of the curve is the rest phase, for when $T_{set} = 20$ °C, $T_c(0) = -10$ °C and $\gamma_3 = 30$.

2.4 Certifying (in)feasibility

In the previous section, two approximations of the optimal solution to (OCP) were presented; one of which appeared to be *better* that the other in an example. In this section, the relative proximity of the approximate solutions to the true optimal is studied by comparing the size of the respective feasible domains. Such a comparison would help highlight the impact of the rest phase in the approximation of the optimal solution; this time, for a wider range of operating conditions.

Computing the domains where (OCP) is feasible when using either $CV-CC$ or $CV-CC-rest$ is accomplished with relative ease: by discretizing the state-space and forward simulating. On the other hand, identifying the set of initial conditions from which (OCP) is feasible (with the true optimal solution) is challenging; solving the optimization problem for each initial condition as in Sec. 2.2 takes ~ 8 mins, and there is no guarantee that the obtained solution is the global optimal. With 10 nodes per dimension in the grid, a conservative estimate of the time to approximate $X \backslash X_0$ would take in excess of 10 days when executed in parallel across 20 cores. We seek a better alternative.

The problem of identifying the set of initial battery states from which (OCP) (introduced in Sec. 2.2) is (in)feasible, is related the time-limited backwards reachable-set identification problem. Before formalizing this relation, we first define the *controlled, time-limited free-time* backwards reachable set as follows.

Definition II.10 (The ctBRS)**.** The controlled time-limited backwards-reachable-set of X_T

satisfies

$$
\begin{aligned}
X_0^f = \{x_0 \in X \mid \exists I : [0,t_f] \times X \to [0, I_{max}],& \\
\text{st. } \exists\, \zeta : [0,t_f] \xrightarrow{\text{dynamics}} X,\, \zeta(0) = x_0,& \\
v_t(\, \zeta(t),\, I(t, \zeta(t))\,) \in Y,\, \forall t \in [0, t_f],& \\
\text{and } \exists \tau \in [0, t_f],\, \zeta(\tau) \in X_T\},&
\end{aligned}
$$

where $x = [z, v_1, T_c, T_a, T_h]'$, X is the state-space, $Y := [v_{min}, v_{max}]$ is the admissible output space, and ζ is a state trajectory that satisfies the dynamics almost everywhere.

Recall that the *time-limited free-time* backwards reachable set was defined in Sec. 2.3 (Defn. II.6). The *ctBRS* differs from the *tBRS* in that the former considers all possibly current trajectories; the latter assumes that the current is identically zero (rest phase). That is, the *ctBRS* is the set of initial conditions from which there exists a control policy that can drive the system-states to the desired terminal configuration.

With *ctBRS* defined as above, the following Lemma relates this set to the set of feasible initial conditions for (OCP).

Lemma II.11. *The maximal feasible set of initial conditions of* (OCP) *is the largest controlled, time-limited backwards reachable set.*

In this section, we estimate the *ctBRS* employing the same principle as introduced in Sec. 2.3.2.1 and use approximations as described in Sec. 2.3.2.2.

Recall that the objective in Example II.7 was to increase the battery's temperature to $T_{des} = 20$ °C within 150 s when the the atmosphere's temperature $T_\infty = -10$ °C and $\gamma_3 = 30$. The particular problem solved in this section maintains the temperature of the temperature of T_∞ constant whilst varying the initial battery temperature and SOC. Solving for degree 10 representations of functions v and w on a workstation with an Intel Xeon E5-2660 processor and 128GB of RAM and took 19 minutes to solve, and the resulting solution can be stored in 360 bytes, and evaluated onboard almost instantaneously [4].

Figure 2.9 documents the key aspects of the solution. The boundary of the approximation of the *ctBRS* is traced in solid blue. The boundaries of the feasible region as derived by using the CV-CC and CV-CC-rest approximations are traced in black dot-dashed and solid red with x markers respectively. These boundaries are *under-approximations* since they were derived by gridding the state-space and forward simulating the dynamics.

The region of the space that is colored in gradients quantifies the impact that the rest phase has on the approximate solution as computed using Eqn. (2.11).

There are a few major takeaways from Fig. 2.9:

---

[4] An implementation of this problem can be found at `http://www.umich.edu/~elemsn`

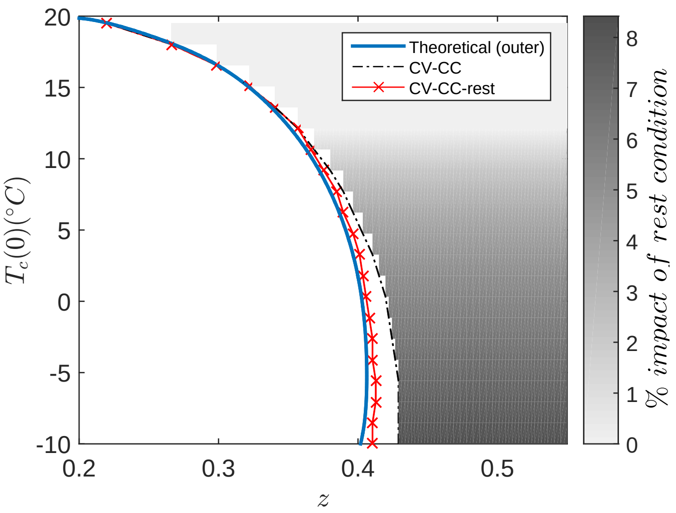

Figure 2.9: This figure demonstrates the influence of the shape of the control on the size of the region from which (OCP) is feasible; the shaded region is the feasible set. Amongst the two approximate trajectories, CV-CC-rest yields a bigger feasible set that is close to the theoretical outer approximation. The gradation in the shaded region is indicative of the impact of the rest condition.

1. The outer approximation of the theoretical region of the state-space from which (OCP) is feasible, contains the sets deemed feasible by both CV-CC and CV-CC-rest, and serves as a sanity check.

2. CV-CC-rest carves-out a larger portion of the space as being feasible.

3. The impact of rest diminishes as the temperature increases. This can be explained by realizing that as the temperature of the battery increases, the time constant decreases; i.e. the value of v_1 is typically smaller and hence the rest condition is not necessarily satisfied at any point along the trajectory (refer to Fig. 2.8).

4. The gap between the theoretical outer and the CV-CC-rest's curve is not significant. This reinforces the belief that for the situation described in Example II.7, the *true* optimal solution is likely to be similar to CV-CC-rest.

Remark II.12. The *ctBRS*, besides being useful to gauge the *closeness* to optimality of the approximations, can serve an additional purpose. If it were possible to store information about the *ctBRS*, an onboard supervisory controller can use this information to steer the system states towards a feasible portion. For example, on a cold winter day, prior to coming to a halt, the supervisory controller in a Hybrid Electric Vehicle can ensure that there is adequate remaining energy in the battery such that warm-up is possible.

2.5 Conclusions

2.5.1 Summary

A warm-up policy is deemed *productive* if it is capable of increasing the battery's temperature whilst ensuring that there is adequate energy stored to perform work after warm-up. In this chapter, the problem of time-limited energy-optimal productive warm-up of Li-ion batteries from sub-zero temperatures when using a battery powered heater and convective heating is presented and solved.

It is identified that the optimal solution, at every instant, attains only extreme values. Numerical solutions are observed to resemble a sequence of constant voltage (CV), constant current (CC) and rest phases. The influence of losses to the atmosphere is parametrically investigated and it is noted that the system has to be reasonably well-insulated for the heater to be of any assistance in warm-up. Lastly, by approximating the optimal policy by either a CV-CC sequence or a CV-CC-rest sequence, the problem of ascertaining the feasibility of productive warm-up is addressed.

2.5.2 Deductions

Observations from numerical simulations suggest that a CV-CC-rest approximation of the optimal policy is close to the true optimal solution. That is, it is good to draw the maximum current possible at every instant, until the rest condition is satisfied. The impact of the rest phase is more pronounced only when warming from deep in the cold. The rest phase aside, this approximation is expected to be optimal with respect to the minimum time optimal control problem prompting the question, 'Are the energy-optimal and time-optimal warm-up problems equivalent in the sense of inverse optimal control problems?'.

In this chapter, it was assumed that the heater could sink any power that was provided by the battery. The rule to draw the maximum admissible current when needed, is not expected to change when the heater has power constraints. That is, the optimally-sized heater (cost and energy-optimal) is the smallest heater that can sink the maximum power output from the battery.

CHAPTER III

Comparison of Optimality Metric and Robustness to Parameters

This chapter builds on the results in Chapter II with the primary objective of answering the following questions:

1. How does the power capability based terminated energy-optimal solution look?
2. Are there instances when the temperature and power capability based problems have identical solutions?
3. Is there is a relation between the minimum time warm-up problems and the other formulations states above?
4. In terms of robustness to parametric uncertainty, is a power capability based terminal constraint better than one that is temperature based?

This chapter is organized as follows: Section 3.1. Section 3.3 demonstrates that the energy-optimal warm-up problems with temperature and power capability based constraints, and the minimize time warm-up problem are equivalent when the influence of polarization is ignored. To compare between problems that have temperature and power capability as terminating conditions, the sensitivity of their corresponding costs is studied through numerical simulations. Finally, conclusions are drawn in Section 3.5.

3.1 Battery Model

In this section, the couple electro-thermal dynamics of the $LiFePO_4$ (A123 26650) battery considered in this chapter is described.

The representation of the electrical sub-system of the battery whose capacity is Q Ahrs, is constituted by two states — one that corresponds to the State of Charge (z) and the other corresponding to bulk polarization voltage (v_1) across a virtual capacitor with capacitance

Parameter	α_1	α_2
Value	0.0214	0.0035

Table 3.1: Parameters of the thermal model

C F.

$$\begin{aligned} \dot{z} &= -\frac{I}{3600 \cdot Q} \\ \dot{v}_1 &= -\frac{v}{\tau(T_c)} + \frac{I}{C(T_c)} \\ v_t &= v_{oc}(z) - v_1 - I \cdot R_s(T_c), \end{aligned} \tag{3.1}$$

where I is the current in Amperes (positive when discharging), temperature dependent real functions τ, C, R_s represent the time constant of the overpotential and ohmic drop respectively, and T_c is the battery's temperature. A polynomial approximation of these functions, derived from the data presented in [58], is presented in Eqns. (3.2).

The thermal dynamics of the cylindrical cell is modeled by a single state representing the bulk temperature (T_c) of the cell [68].

$$\dot{T}_c = \alpha_1 \cdot P_{Joule} + \alpha_2 \cdot (T_\infty - T_c), \tag{3.3}$$

where T_∞, T_c are the temperatures of the atmosphere, and cell respectively; the values of the different parameters are as listed in Tab. 3.1; and

$$P_{Joule} = I^2 \cdot R_s(T_c) + v_c^2 \frac{C(T_c)}{\tau(T_c)} \tag{3.4}$$

3.2 Energy-Optimal Warm-Up

In this section, we introduce two optimal control problems that minimize the energy consumed during warm-up, subject to operating constraints on terminal voltage and battery current. The two problems considered herein differ in their definition of what constitutes a

---

$$\begin{aligned} R_s(T_c) &= -6.833 \times 10^{-7} T_c^3 + 5.477 \times 10^{-5} T_c^2 - 1.468 \times 10^{-3} T_c + 0.02421 \\ \tau(T_c) &= 1.088 \times 10^{-5} T_c^4 - 6.002 \times 10^{-4} T_c^3 - 1.961 \times 10^{-3} T_c^2 - 0.116 T_c + 47.57 \\ C(T_c) &= -1.186 \times 10^{-3} T_c^3 - 0.144 T_c^2 + 45.63 T_c + 1360 \\ v_{oc}(z) &= 1.528 z^3 - 2.264 z^2 + 1.193 + 3.091 \\ v_{min} &= 2 \text{ V}, Q = 2.3 \text{ Ah}, I_{max} = 25 \text{ A}, v_{max} = 3.6 \text{ V} \end{aligned} \tag{3.2}$$

warm-up battery – the first uses heats the battery until the battery's temperature reaches a pre-specified level; the second formulation uses the power capability of the battery as an indicator of when the battery is ready for use in discharge mode, instead of temperature. Both optimal control problems are numerically solved and solutions are presented and discussed.

For notational convenience, we define the following placeholders for constraints that will appears in the optimal control problems described in this chapter.

$$\mathcal{V} := \{v_{oc}(z(t)) - v_1 - I(t)R_s(T_c(t)) \in [v_{min}, v_{max}]\} \tag{3.5}$$

$$\mathcal{I} := \{I(t) \in [0, I_{max}]\} \tag{3.6}$$

$$\mathcal{F}_{t_f P} := \{P_{cap}(t_f) = P_{des}\} \tag{3.7}$$

$$\mathcal{F}_{t_f T} := \{T_c(t_f) = T_{des}\} \tag{3.8}$$

The above constraints, in order, enforce that the terminal voltage and current are bounded; that the terminal power capability (at time $t = t_f$) and terminal temperature meet specifications. Further, the states of the systems are represented in vector form as $x = [z, v_1, T_c]$ and the dynamics of the coupled electro-thermal system is written as $\dot{x} = f(x, I, T_\infty)$.

3.2.1 Temperature as terminal constraint

The temperature limited warm-up problem was reported in [3] and is presented below.

$$(P^T) \qquad \min_{I \in L^2([0,t_f];[0,I_{max}])} \left\{ \int_0^{t_f} I(t)\, dt \;\middle|\; \begin{array}{l} \dot{x} = f(x, I, T_\infty) \\ \mathcal{V} \wedge \mathcal{I} \wedge \mathcal{F}_{t_f T} \end{array} \right\} \tag{3.9}$$

The problem (P^T) seeks to find the trajectory of current that results in the least drop in battery SOC whilst increasing its temperature to the set-point T_{des}. Additionally, the optimal current is to be chosen that the resulting terminal voltage and current trajectories are within the manufacturer's stipulated safe operating range.

It was shown in Chapter II that the optimal policy to (P^T) attains only the maximum or minimum value at every instance. Figure 3.1 depicts the control, state, and output trajectories that result from solving (P^T) with $z(0) = 0.6$, $T_{des} = 10$ °C, $T_c(0) = T_\infty = -20$ °C. To obtain the above solution, the problem was solved using pseudo-spectral collocation with GPOPS2 as the problem parser and IPOPT as the back-end solver [63].

Note that in Fig. 3.1, the optimal current consists of three distinct phases namely constant voltage (CV), constant current (CC) and rest. The 'ON' phase depicted in Fig. 3.1 subsumes the CV and CC phases. Despite the appearance of switching-like behavior closer to the start and end of the 'ON' phase, in Chapter II, it was shown that the optimal solution can be approximated without this switching pattern, without a significant change in cost.

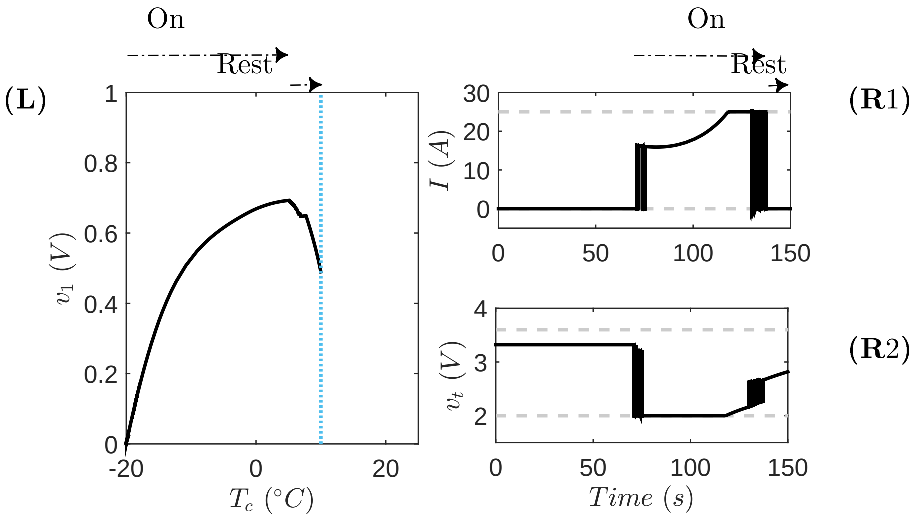

Figure 3.1: Trajectories of control, state and terminal voltage resulting from applying the optimal solution to (P^T) with $t_f = 150$ s, $T_{des} = 10$ °C, $z(0) = 0.6$, $T_c(0) = T_\infty = -20$ °C. Subplot (L) presents the evolution of cell temperature (T_c) and bulk polarization (v_1); subplots (R1) & (R2) depict the energy-optimal current trajectory and the resulting terminal voltage. In the subplots on the right, the dashed gray lines identify the boundary of the corresponding constraints. Notice that the optimal current consists of distinct operating phases. In [3], it is shown that the optimal policy can be approximated by such a staged current.

3.2.2 Power capability as terminal constraint

The energy-optimal warm-up problem with power constraints is presented, using (P^T) as a template, below.

$$(P^P) \qquad \min_{I\in L^2([0,t_f];[0,I_{max}])}\left\{\int_0^{t_f} I(t)\,dt \;\middle|\; \begin{array}{l}\dot{x} = f(x,I,T_\infty)\\ \mathcal{V}\wedge\mathcal{I}\wedge\mathcal{F}_{t_fP}\end{array}\right\} \tag{3.10}$$

Problem (P^P), similar to (P^T), aims to increase the battery temperature; however, the decision to terminate warm-up is dictated by the instantaneous power that can be delivered that is defined as

$$P_{cap} = v_{min}\frac{v_{oc}(z) - v_1 - v_{min}}{R_s(T_c)}. \tag{3.11}$$

Since problems (P^T) and (P^T) differ only in the terminating condition, one would expect that the optimal solution will share characteristics. Indeed, the optimal policy to (P^P), much like that of (P^T), attains only extreme values at each instant as shown in the following result.

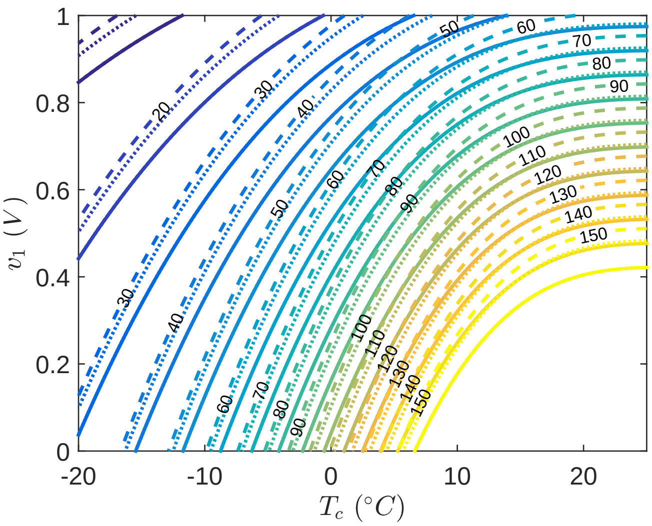

Figure 3.2: Power capability contour as a function of battery temperature, polarization and SOC (the dashed, dotted and solid lines correspond to $z = 0.2, 0.5, 0.7$ respectively). Notice that at any given temperature, as v_1 increases, the power capability decreases. For a fixed polarization level, increasing battery temperatures increase the power capability. Importantly, note that the power capability is more sensitive to changes in v_1.

Theorem III.1. *The optimal policy to* (P^T), $I^* \in L^2([0, t_f]; [0, I_{max}])$, *satisfies*

$$I^*(t) \in \left\{0, \min\left\{\frac{v_{oc}(z) - v_1 - v_{min}}{R_s(T_c)}, I_{max}\right\}\right\}. \qquad \forall t \in [0, t_f] \quad (3.12)$$

Proof. The proof follows directly from that of [3, Theorem 1] with one minor change: in the proof of [3, Lemma 12], employ the fact that as the battery temperature increases, the P_{cap} increases (refer to Fig. 3.2) to establish the sign of the co-state. □

The optimal policy to (P^T) generally is not found to have prolonged periods of rest during the 'ON' portion of the trajectory; a similar statement cannot be made of the minimizer of (P^P). The value of instantaneous power capability is influenced by the build-up of bulk polarization (recall that P_{cap} depends linearly on v_1). Figure 3.2 presents contours of the instantaneous power capability for varying levels of polarization, SOC levels and cell temperature. Observe that P_{cap} is more sensitive to changes in v_1 than to those in T_c; the sensitivity has a negative correlation with the former and a positive correlation with the latter.

The minimizer of (P^P) will likely have periods of rest in the 'ON' phase, for they can be beneficial to raise P_{cap}. During a period of rest, since the dynamics of v_1 and T_c are asymptotically stable, the values of v_1 and T_c tend to decrease. The time constant of the dynamics of T_c is larger than that of v_1. Consequently, as P_{cap} is more sensitive to v_1, a

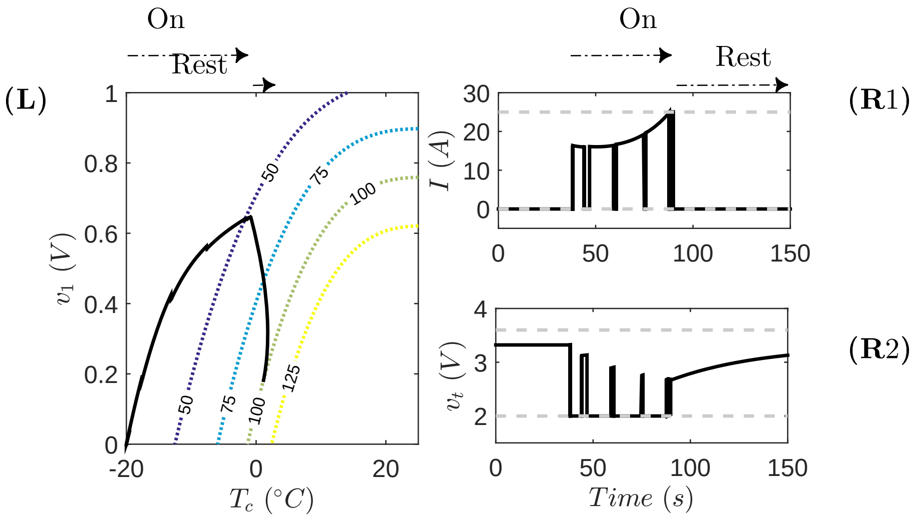

Figure 3.3: Solutions to (P^P) when $t_{max} = 150$ s, $P_{dmd} = 100$ W, $z(0) = 0.6$, $T_\infty = -20$ °C and the battery is in thermal equilibrium with the atmosphere at time $t = 0$. Subplot (L) presents the evolution of cell temperature (T_c), bulk polarization (v_1) and the contour corresponding to $P_{cap} = 100$ W; subplots (R1) & (R2) trace the optimal policy and the resulting terminal voltage trajectory.

carefully chosen rest can help increase P_{cap} by reducing v_1. Thus, it is to be expected that the optimal solution to (P^P) will include notable rest periods.

Figure 3.3 presents the optimal state, control and output trajectories when (P^P) is solved with $P_{des} = 100$ W, $T_c(0) = T_\infty = -20$ °C and $z(0) = 0.6$. The numerical solution was derived in a manner similar to that in the example in Sec. 3.2.1. Again, note that the optimal current trajectory can be partitioned into an 'ON' phase and a rest phase.

During the 'ON' phase, the solution trajectory is such that either the voltage or current constraint is active; this is in line with Theorem III.1. Moreover, as expected, periods of rest are noted during the 'ON' phase. Subplot (L) traces the trajectory of v_1 plotted against T_c along with some contours of power capability. During the 'ON' phase, P_{cap} increases almost monotonically; including during the periods when of intermittent rest. During intermittent rests, the kink that appears in the curve in subplot (L) occurs to the right of the curve; P_{cap} has increased during these rests.

The other way in which this solution differs from that of (P^T) is that the duration of the 'Rest' phase is longer. During the 'Rest' phase, the P_{cap} almost doubles as depicted in subplot (L); and is this because of the drop in v_1. Notice how the curve bows during the 'Rest' phase in subplot (L); the battery's temperature starts to decrease after a while, and yet P_{cap} continues to increase. This is because P_{cap} is relatively more sensitive to v_1.

In this section, two problem formulations for energy-optimal warm-up were presented; both of which exhibit somewhat similar characteristics. In the next section, it is shows that these two problems are equivalent under certain conditions; in Sec. 3.4, the sensitivity of these problems to parameter uncertainty is studied.

3.3 Equivalence of optimal control problems

The simulation results presented in Sec. 3.2 suggest that the energy-optimal solution has three discernable phases – constant current, constant voltage, and rest. If we ignore any terminal rest period (i.e. ignoring the contribution of bulk polarization from all aspects of the problem), then the solution resembles the action that any engineer would employ without having solved the optimal control problem.

In addition, it was noted that the optimal solution to (P^T) and (P^P) are similar, but not the same. This prompts the question of when they are the same; in this section we address this question in addition to whether the solution to (P^T) is similar to that of the minimum-time problem warm-up problem.

The examples in the previous section suggest that the optimal control problems are not equivalent when the model includes a polarization term (the state v_1 corresponds to the diffusion dynamics in the battery). Thus, in this section, we drop the polarization term from the electrical dynamics of the battery; this reduced battery dynamics is denoted as f_R in the ensuing presentation.

First, in the spirit of the problems defined in Sec. 3.2, we define the following constraints.

$$\bar{\mathcal{V}} := \{v_{oc}(z(t)) - I(t)R_s(T_c(t)) \in [v_{min}, v_{max}]\} \tag{3.13}$$

$$\mathcal{T} := \{\tau \in [0, t_f]\} \tag{3.14}$$

$$\mathcal{F}_T := \{T_c(1) = T_{des}\} \tag{3.15}$$

$$\mathcal{F}_P := \{P_{cap}(1) = P_{des}\} \tag{3.16}$$

$$\mathcal{F}_{\tau T} := \{T_c(\tau) = T_{des}\} \tag{3.17}$$

$$\mathcal{F}_{\tau P} := \{P_{cap}(\tau) = P_{des}\} \tag{3.18}$$

With the above notation, the free terminal-time minimum energy problem can be defined as below.

$$(P_T^R) \qquad \min_{I \in L^2([0,1]), \tau} \left\{ \int_0^1 I(t)\, dt \;\middle|\; \begin{array}{l} \dot{x} = \tau f_R(x, I, T_\infty) \\ \bar{\mathcal{V}} \wedge \mathcal{I} \wedge \mathcal{T} \wedge \mathcal{F}_T \end{array} \right\} \tag{3.19}$$

In the above, τ is the total warm-up time and the minimization is over all square integrable functions. The objective is to minimize the total loss in SOC subject to constraints on terminal voltage current, and with terminal temperature constraint.

Next, analogous problem with power as terminal constraint is introduced.

$$(P_P^R) \qquad \min_{I\in L^2([0,1]),\tau} \left\{ \int_0^1 I(t)\,dt \;\middle|\; \begin{matrix} \dot{x} = \tau f_R(x, I, T_\infty) \\ \bar{\mathcal{V}} \wedge \mathcal{I} \wedge \mathcal{T} \wedge \mathcal{F}_P \end{matrix} \right\} \tag{3.20}$$

The minimum time optimal warm-up problems with terminal temperature and power constraints are defined in the following.

$$(P_{tT}^R) \qquad \min_{I\in L^2([0,1]),\tau} \left\{ \int_0^\tau 1\,dt \;\middle|\; \begin{matrix} \dot{x} = f_R(x, I, T_\infty) \\ \bar{\mathcal{V}} \wedge \mathcal{I} \wedge \mathcal{T} \wedge \mathcal{F}_{\tau T} \end{matrix} \right\} \tag{3.21}$$

$$(P_{tP}^R) \qquad \min_{I\in L^2([0,1]),\tau} \left\{ \int_0^\tau 1\,dt \;\middle|\; \begin{matrix} \dot{x} = f_R(x, I, T_\infty) \\ \bar{\mathcal{V}} \wedge \mathcal{I} \wedge \mathcal{T} \wedge \mathcal{F}_{\tau P} \end{matrix} \right\} \tag{3.22}$$

With the above problems defined, we present the main result of this section that states that the above problems are equivalent in the sense that they result in the same optimal control policy and state trajectories.

Theorem III.2. *The problems* (P_T^R), (P_P^R), (P_{tT}^R), (P_{tP}^R) *are equivalent.*

Proof. To prove this theorem, we consider establishing pairwise equivalence between problems. For ease of presentation, this is broken into the following Lemmas.

Lemma III.3. *The optimal policy to* (P_{tT}^R) *is to draw the maximum admissible current at every instant.*

Proof. We prove this proposition via contradiction. The optimal current takes only extreme values at every time instant [68]. Suppose there is an interval $[t_1, t_2]$ during which the optimal current, I^*, is identically zero and the maximum admissible current is not zero. Let the optimal value associated with this solution be J^* and the associated temperature trajectory be T_c^*; clearly $t_1, t_2 \neq J^*$. Now consider a new policy, I_* such that

$$I_*(t) = \begin{cases} I^*(t) & t \in [0, t_1), \\ I_{cap}(t) & t \in [t_1, t_2], \end{cases} \tag{3.23}$$

where $I_{cap}(t)$ is the maximum admissible current at time t. It is easy to see that the resulting cell temperature trajectory because of I_*, T_{c*}, satisfies $T_c^*(t_2) < T_{c*}(t_2)$. Suppose $T_{c*}(t_2) \leq T_{set}$, and let

$$\tau := \min\{x \mid T_c^*(x) = T_{c*}(t_2), x > t_2\}; \tag{3.24}$$

the existence of τ is trivial. Let us complete the characterization of I_* as follows: $I_*(t) = I^*\big(t + (\tau - t_2)\big), \forall t \in (t_2, J^* - (\tau - t_2)]$ (this completion is admissible because bulk polarization is not considered). It is easy to see that $T_{c*}\big(J^* - (\tau - t_2)\big) = T_{des}$ and hence $J_* = J^* - (\tau - t_2)$; the statement in the proposition follows. If $T_{c*}(t_2) \geq T_{des}$, then $\exists \tau \in [t_1, t_2]$ st. $T_{c*}(t) = T_{des}$; terminate the warm-up at τ to obtain $J_* = \tau < J^*$; and the hypothesis follows. ☐

Lemma III.4. *Problems* (P_T^R) *and* (P_{tT}^R) *are equivalent.*

Proof. Follows trivially from noting that the optimal solutions only takes extreme values and using arguments similar to that in the proof to Lemma III.3. ☐

Lemma III.5. *The optimal policy to* (P_P^R) *and* (P_{tP}^R) *is to draw the maximum admissible current at every instant.*

Proof. The power capability of the battery is defined by

$$P_{cap} = \min\left\{ v_{min}\frac{v_{oc}(z) - v_{min}}{R_s(T_c)}, v_{min}I_{max} \right\}. \tag{3.25}$$

At the terminal time, the following relations hold

$$P_{des} \leq P_{cap} \leq v_{min}\frac{v_{oc}(z) - v_{min}}{R_s(T_c)} \tag{3.26}$$

$$\Rightarrow R_s(T_c) \leq \frac{v_{min}}{P_{des}} \cdot (v_{oc}(z) - v_{min}) \tag{3.27}$$

$$P_{des} \leq P_{cap} \leq v_{min}I_{max} \tag{3.28}$$

$$\Rightarrow \frac{P_{des}}{v_{min}} \leq I_{max} \tag{3.29}$$

If Eqn. (3.29) is not satisfied the problem is not feasible and hence this option is not entertained. Now, note that by definition, $R_s(T_c)$ is monotone decreasing in T_c. Thus, the constraint in Eqn. (3.27) can be re-written in the following form

$$T_c \geq \alpha, \tag{3.30}$$

for some α, a function of P_{des} and $v_{oc}(z)$. Since increasing the battery's discharging power capability consumes energy, and problem (P_P^R) is minimizing energy consumed, the optimal solution satisfies Eqn. (3.30) with an equality. Thus, (P_P^R) can be translated into an equivalent problem with terminal temperature constraints. Thus, this problem is equivalent to (P_T^R).

Using similar arguments, it is can be shown that (P_{tP}^R) is equivalent to (P_{tT}^R). ☐

The above Lemmas prove that $(P_{tT}^R) \equiv (P_T^R) \equiv (P_T^R) \equiv (P_{tP}^R)$ ☐

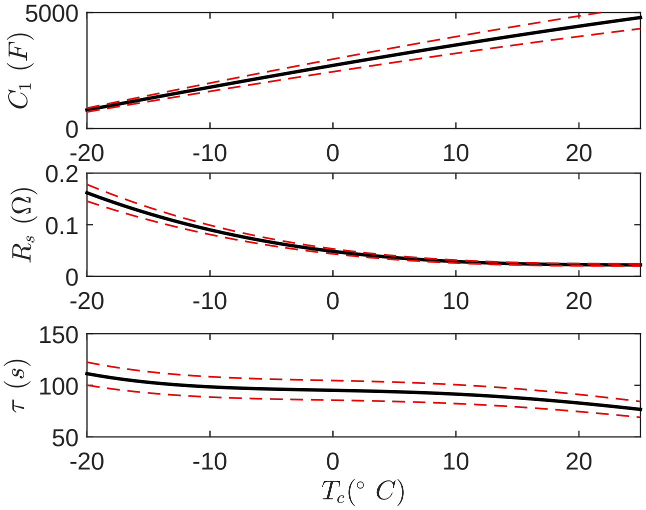

Figure 3.4: The values of electrical sub-model parameters at different temperatures with a 3σ envelope around them.

3.4 Sensitivity to parameter uncertainty

Problems (P^T) and (P^P) introduced in Sec. **??** differ only in that the terminal constraints are specified differently – (former) the more conventional temperature constraint; (latter) power capability constraint. Batteries typically serve as energy storage elements that can be used to power loads. Thus a more natural specification for battery warm-up is power capability; i.e. warming the battery until it can provide the desired power (problem (P^P)). However, such a formulation does not often feature in literature; temperature as terminal constraint is more prevalent (problem (P^T)).

In Sec. **??** it was shown that under certain assumptions, the terminal temperature and terminal power constraint specifications are equivalent. In practice, these assumptions are not necessarily met—since the influence of diffusion dynamics is not ignorable—and hence the designer/practioner is likely faced with having to choose between formulations. To aid making this decision, in this section we compare the two problem formulations.

Comparing the two problems is equivalent to studying the impact of the terminal constraint. In this section, we study the sensitivity of the terminating constraints to parametric uncertainty; specifically, the sensitivity to multiplicative uncertainty of the following form

$$\tilde{C}(T_c, \Delta C_1) = (1 + \Delta C_1)C(T_c), \tag{3.31}$$

$$\tilde{\tau}(T_c, , \Delta\tau) = (1 + \Delta\tau)\tau(T_c), \tag{3.32}$$

$$\tilde{R}_s(T_c, \Delta R_s) = (1 + \Delta R_s)R_s(T_c). \tag{3.33}$$

To accommodate these uncertain parameters, the dynamics is re-written in the discrete domain as follows:

$$z_{k+1} = z_k + \frac{\delta t}{3600Q} I_k \tag{3.34}$$

$$v_{1,k+1} = \left(1 - \frac{\delta t}{\tilde{\tau}(T_{c,k}, \Delta R_{s,k})}\right) v_k + \frac{\delta t}{\tilde{C}_1(T_{c,k}, \Delta C_{1,k})} I_k \tag{3.35}$$

$$v_{t,k} = v_{oc}(z_k) - v_{1,k} - \tilde{R}_{s,k}(T_c, \Delta R_{s,k}) I_k \tag{3.36}$$

$$T_{c,k+1} = \alpha_2 \delta t \cdot T_\infty + (1 - \alpha_1 \delta t) T_{c,k} + \delta t \cdot P_{Joule,k} \tag{3.37}$$

with $\Delta C_{1,k} \sim N(0, 0.01/9), \Delta R_{s,k} \sim N(0, 0.01/9), \Delta \tau_k \sim N(0, 0.01/9)$ are independent and identically distributed.

With the above description, it is easy to see that at each temperature, parameters are distributed normally with the mean given by the expression in Eqn. (2.2); the variance changes to ensure that with 0.99 probability, the values are within 10% of the mean. Figure 3.4 presents the key features of the parameter distribution against battery temperature.

An analytic comparison of the sensitivity of problems (P^T) and (P^P) with these uncertain parameters is beyond the scope of the present discussion; it will be studied in a future study. Instead, in this chapter, the robustness of the problems is assessed by way of studying the impact of parameter uncertainties on the terminal constraints.

With this description of the dynamics, the terminating conditions are compared as described hereafter. First, it is assumed that the current trajectory is constituted only by the 'ON' phase that was identified in Sec. 3.2. The discrete dynamic is simulated at rates faster than 10 Hz, drawing a new value for the random variables at each sample. When the terminal conditions are satisfied, the simulation is terminated and the energy consumed during warm-up is computed. Five thousand such trials were performed and the resulting distribution of energy consumed is studied. Figure 3.5 presents the resulting distribution obtained by performing one-factor-at-a-time randomization.

Remark III.6. In Chapter II, a method to approximate the optimal solution to (P^T) was described; an approximation that included both the 'ON' phase and the rest phase. Employing the techniques therein, it is possible to generate an approximate solution for (P^P). Such approximations cannot however be used to study the impact of parameter uncertainty on the terminating condition, for feasibility of the problem cannot be guaranteed.

The presented data was collected by solving the problems with the following specifications: $z(0) = 0.6$, $T_c(0) = T_\infty = -20$ °C, $P_{des} = 100$ W and $t_f = 150$ s. The value of T_{des} for (P^T) was set based on the solution to (P^P) as follows:

$$T_{des} \geq \max\{T_c^*(t), \ \forall t \in [0, t_f]\}$$

where T_c^* is the temperature trajectory resulting from applying the optimal solution to (P^P)

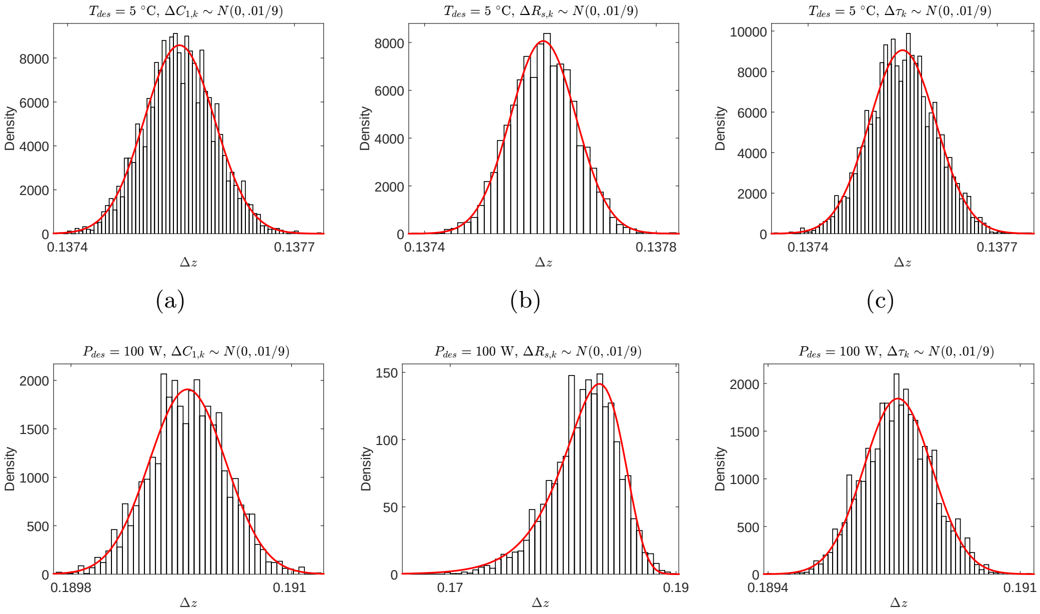

(a) (b) (c)

(d) (e) (f)

Figure 3.5: Comparison of one-factor-at-a-time sensitivity of optimal cost with power and temperature constraints

in the case where there is no randomness in parameters. The termination temperature is set as $T_{des} = 5$ °C.

In Fig. 3.4 each subplot presents the histogram of energy consumed and a fit of the distribution; in all but subplot (e), the fitted distribution is Beta; it is a Weibull distribution in subplot (e). Subplots (a)–(c) present data corresponding to (P^T) and the remaining subplots depict information pertinent to (P^P).

Let the distribution of Δz be denoted by ν. We define[1] a metric for the impact that uncertainties have on the cost, as follows:

$$\eta(\nu) := \frac{\inf_{A\subset[0,1]}\{\lambda(A) \mid \nu(A) \geq 0.99\}}{\int 1 \, d\nu}, \tag{3.38}$$

where λ is the Lebesgue measure on the real line. For convenience, let us refer to this metric as *impact*. The *impact* of ν is the normalized spread of the distribution (as measured by the size of the smallest set from which events occur 99% of the time) and can be interpreted as the cautiously worst-case impact of uncertainty on the cost. Recognize that for distributions with long tails, this metric might ignore much of the tail; also, the shape of the distribution is immaterial.

From Fig. 3.4, the impacts of the different distributions are computed and tabulated in

---

[1] In this case, the more intuitive metric of ratio of variance to mean is not quite applicable since one of the distributions in consideration is not like the others; and because they are not all normally distributed.

	Uncertain parameter		
i Constraint	Resistance	Capacitance	Time constant
Temperature	0.0028	0.0025	0.0024
Power	0.1294	0.0075	0.0087

Table 3.2: The computed *impact* of distributions of SOC lost in warm-up because of uncertainty in different parameters. The impacts are computed for each of the two terminal constraints under study–temperature and power.

Table 3.2. Notice that, under this metric, uncertainties in the different parameters coupled with the temperature constraint have almost identical influence on the energy consumed during warm-up. This coincides with the inference one would derive by visual inspection. This can be reasoned by recalling that temperature is a state of the system whose evolution is affected by the uncertain parameters only via the heat generation term. Any noise/variation in the input to the thermal dynamics gets filtered-out by the slow dynamics. A detailed investigation of the mechanics of this process is deferred until a subsequent work.

Power as a terminal constraint is generally more sensitive to uncertainties. This is surmised by comparing the entries in Tab. 3.2. In particular, uncertainties in the series resistance have the most influence on the total energy consumed. The impact that uncertainties in the series resistance have on the terminal constraint is immediately apparent upon inspecting the expression of P_{cap}.

$$P_{cap} = v_{min} \frac{v_{oc}(z) - v_1 - v_{min}}{R_s(T_c, \Delta R_s)} \tag{3.39}$$

This uncertain parameter manifests directly in the denominator of the expression in the constraint description, unlike in the temperature based constraint where the influence is filtered.

Based on the above discussion, it appears that using temperature as a terminal constraint can serve one better when the model of the system is not accurately known. It is absolutely essential to note that this discrepancy is not of relevance when working on a physical test-bench/hardware, for in that case a feedback policy would be driven by a particular instantiation of the parameters (no randomness). This result however can help in the planning stage; when the battery's parameters are still not known exactly.

Remark III.7. The discussion and comparison in this section is based on some feasible solution (the 'ON' phase current). That the observed *impact* is small when using this feasible solution is not indicative of the variation in the *true* optimal cost. The authors conjecture that there is a relation between the variance when the parameter variation is bounded, and the value functions satisfy certain regularity conditions.

3.5 Conclusions

In this chapter, the power counterpart to energy-optimal warm-up with terminal temperature constraint is presented and solved. In addition, it is shown that when the influence of polarization voltage is not significant, then some warm-up problems are equivalent. Lastly, it is shown, via simulations, that there is reason to believe that problems with temperature as terminal constraints are less sensitive to parameter uncertainties.

CHAPTER IV

State, Parameter and Power Capability Estimation and its Applications

The performance and longevity of these batteries hinges on constraining their operation such that their terminal voltage, and internal and surface temperatures are regulated within prescribed ranges [69, 70]. With these batteries acting as power sources, an effective way to respect operating constraints is through active regulation of power-flow – a task performed by a supervisory controller in electrified vehicles (refer Fig. 4.1).

The power capability of a battery is the constant power that can be provided by or drawn over a finite window of time without violating operating constraints [71]. Methods to estimate power capability have been widely explored in literature. In [71–74] the authors, using a representative equivalent circuit model, compute the maximum admissible battery charge and discharge power ensuring that the battery's terminal voltage and SOC remain constrained. The authors of [75] and [76] use a *more* physics-based electrochemical model to impose direct constraints on SOC and Li-ion concentration.

There is another constraint that significantly influences the rate of battery degradation of Li-ion batteries: temperature. It is well understood that operating batteries in elevated temperatures increases the potential for adverse side reactions and results in accelerated degradation [69]; however, it has not been factored-in when computing the power capability. This work aims to address this lacuna by using reduced-order models to represent the electrical and thermal dynamics of the battery.

The electrical and thermal behavior of Li-ion batteries depends on their current state and operating conditions. Since most power capability estimation techniques rely on model inversion, accurate information of the local dynamic behavior and estimates of internal states are desired. Thus, state-parameter estimation has been considered as an important aspect in the problem of power capability estimation [72–74, 77]. Broadly, the most common methods employed can be classified as being based on dual [77] or joint estimation [73, 74]. Dual estimation is often preferred for it promises to minimize the influence of poor *a priori* knowledge of the values of parameters and poor quality of measurements on state estimates. In this chapter we propose another augmented-state-parameter-space (aSPs) partitioning

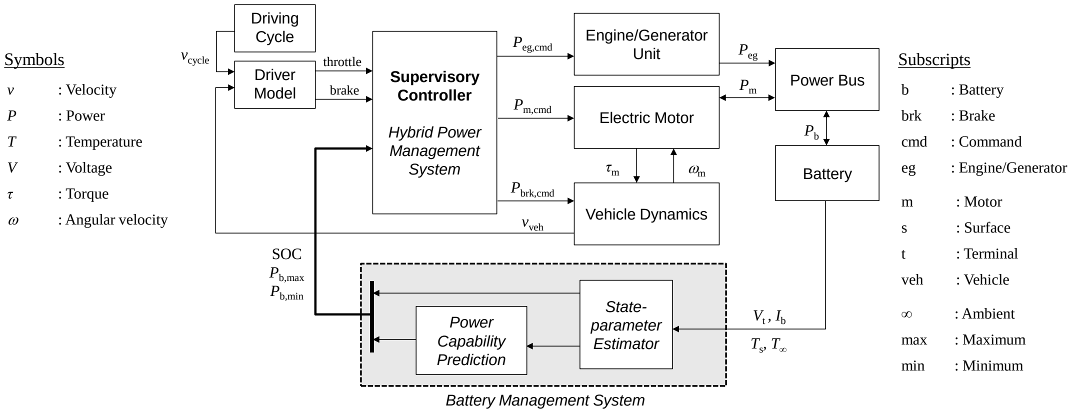

Figure 4.1: A schematic of power and battery management systems in an SHEV simulation framework. The focus of the chapter is on the battery management system, the gray shaded box.

technique based on a notion of relative estimability. A significance metric computed from Principal Component Analysis (PCA) on the Fisher Information Matrix (FIM), similar to the ones defined in [78–81] for off-line parameter identification, is used to measure relative estimability. The aSPs is partitioned based on these significance metrics to aggregate elements which have a similar influence on the system output. Finally, each partition is endowed with an estimator, in this instance an Extended Kalman Filter (EKF).

The contribution of this chapter is three-fold: 1) a simple and effective method to determine thermally and electrically constrained power capability of Li-ion batteries; 2) a quantitative metric—termed significance metric—is introduced to assess the estimability of states and parameters of the electro-thermal battery model based on the FIM; and 3) partitioned estimators for on-line state-parameter identification are designed based on the significance metrics.

This chapter is organized as follows: Section 4.1 describes the electrical and thermal dynamic models of the battery used in this study. Section 4.2 details a method to estimate the power capability of a battery accounting for electrical and thermal constraints. Section 4.3 proposes a quantitative metric based on PCA to partition the augmented-state-space in designing estimators, and Section 4.4 presents the control of a Series Hybrid Electric Vehicle (SHEV) as an example application of the presented techniques. Finally, Section 4.6 concludes the chapter with a summary of contributions and with a discussion on possible extensions.

4.1 Control-Oriented Battery Model

One of the objectives of this work is to develop on-line estimation and control algorithms. To that end, simple control-oriented models are employed to capture the electrical and thermal behavior of Li-ion batteries. Specifically, an *equivalent-circuit* model for the electrical

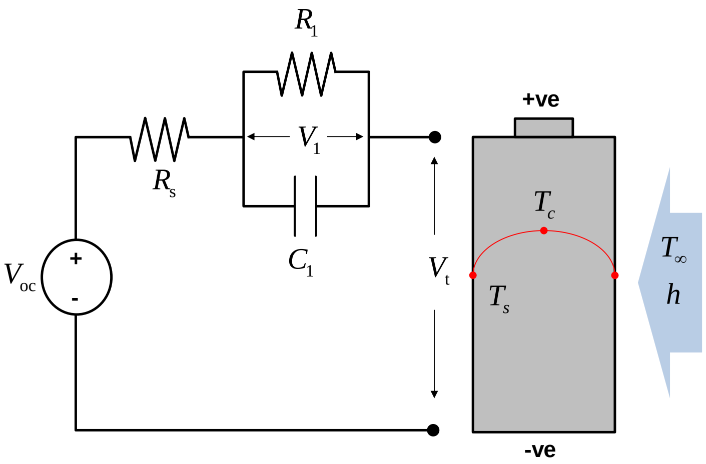

Figure 4.2: Schematic of an electro-thermal model for cylindrical batteries consisting of an equivalent-circuit model and 1-D thermal model

dynamics [82], and the reduced order model developed in [83] for the thermal dynamics are adopted.

4.1.1 Electrical dynamics

A two-state equivalent-circuit model is considered to predict terminal voltage as shown in Fig. 4.2. The electrical dynamic behavior of the battery with the total capacity Q_b in discrete-time domain is described by

$$\begin{bmatrix} z_{k+1} \\ v_{1,k+1} \end{bmatrix} = A_e \begin{bmatrix} z_k \\ v_{1,k} \end{bmatrix} + B_e I_k, \tag{4.1a}$$

$$v_{t,k} = v_{oc}(z_k) - v_{1,k} - R_{s,k} I_k, \tag{4.1b}$$

where system matrices A_e and B_e are expressed by

$$A_e = \begin{bmatrix} 1 & 0 \\ 0 & e^{\frac{-\Delta t}{R_{1,k} C_{1,k}}} \end{bmatrix},$$

$$B_e = \begin{bmatrix} -\frac{\Delta t}{Q_\mathrm{b}} \\ R_{1,k}\left(1 - e^{\frac{-\Delta t}{R_{1,k} C_{1,k}}}\right) \end{bmatrix}.$$

The battery SOC, z, and polarization voltage, v_1, are states, i.e. $x_e = [z, v_1]'$; I is the current; v_t and v_{oc} are the terminal voltage and open circuit voltage of the battery, respectively. The series resistance, R_s, and polarization resistance/capacitance, (R_1, C_1), are parameters to be estimated, i.e., $\theta_e = [R_s, R_1, C_1]'$. The subscript e denotes the electrical system to differentiate from the thermal system later. The sampling period in battery management system is denoted by Δt. Refer to Chapter V for a list of nominal values of the parameters of the model when the cell under consideration is an A123 26650 LFP cell.

4.1.2 Thermal dynamics

To predict core and surface temperatures of the battery, T_c and T_s, respectively, a reduced-order model developed in [83] is adopted and reproduced below for convenience:

$$\begin{bmatrix} \bar{T}_{k+1} \\ \bar{\gamma}_{k+1} \end{bmatrix} = A_t \begin{bmatrix} \bar{T}_k \\ \bar{\gamma}_k \end{bmatrix} + B_t \begin{bmatrix} \dot{q}_k \\ T_{\infty,k} \end{bmatrix}, \tag{4.2a}$$

$$\begin{bmatrix} T_{\mathrm{c},k} \\ T_{\mathrm{s},k} \end{bmatrix} = C_t \begin{bmatrix} \bar{T}_k \\ \bar{\gamma}_k \end{bmatrix} + D_t T_{\infty,k}, \tag{4.2b}$$

where $\bar{T}$ is the averaged temperature and $\bar{\gamma}$ is the averaged temperature-gradient. The above model was derived from the simple 1D heat equation assuming uniform heat generation across the radius of the cylindrical cell and a quadratic form for the temperature distribution along the radial direction. Ambient temperature and the rate of heat generation are denoted by T_∞ and $\dot{q}$, respectively. The subscript T denotes the thermal system. Matrices of the thermal system are given by

$$A_t = \begin{bmatrix} \frac{hr^2+24k_t r-48\alpha h\Delta t}{r(24k_t+rh)} & \frac{-15\alpha h\Delta t}{24k_t+rh} \\ \frac{-320\alpha h\Delta t}{r^2(24k_t+rh)} & \frac{hr^3+24k_t r^2-120\alpha\Delta t(rh+4k_t)}{r^2(24k_t+rh)} \end{bmatrix},$$

$$B_t = \begin{bmatrix} B_{t_1} & B_{t_2} \end{bmatrix} = \begin{bmatrix} \frac{\alpha\Delta t}{k_t V_b} & \frac{48\alpha h\Delta t}{r(24k_t+rh)} \\ 0 & \frac{320\alpha h\Delta t}{r^2(24k_t+rh)} \end{bmatrix},$$

$$C_t = \begin{bmatrix} C_{t_1} \\ C_{t_2} \end{bmatrix} = \begin{bmatrix} \frac{24k_t-3rh}{24k_t+rh} & -\frac{120rk_t+15r^2h}{8(24k_t+rh)} \\ \frac{24k_t}{24k_t+rh} & \frac{15rk_t}{48k_t+2rh} \end{bmatrix},$$

$$D_t = \begin{bmatrix} D_{t_1} \\ D_{t_2} \end{bmatrix} = \begin{bmatrix} \frac{4rh}{24k_t+rh} \\ \frac{rh}{24k_t+rh} \end{bmatrix},$$

$$I_{max,k}^{z_{min}} = \left(\sum_{i=0}^{N-1} C_{e_1} A_e^i B_e + D_{e_1} \right)^{-1} \left(z_{min} - C_{e_1} A_e^N \begin{bmatrix} z_k \\ v_{1,k} \end{bmatrix} - E_{e_1} \right), \tag{4.3a}$$

$$I_{min,k}^{z_{max}} = \left(\sum_{i=0}^{N-1} C_{e_1} A_e^i B_e + D_{e_1} \right)^{-1} \left(z_{max} - C_{e_1} A_e^N \begin{bmatrix} z_k \\ v_{1,k} \end{bmatrix} - E_{e_1} \right), \tag{4.3b}$$

$$I_{max,k}^{v_{min}} = \left(\sum_{i=0}^{N-1} C_{e_2} A_e^i B_e + D_{e_2} \right)^{-1} \left(v_{min} - C_{e_2} A_e^N \begin{bmatrix} z_k \\ v_{1,k} \end{bmatrix} - E_{e_2} \right), \tag{4.3c}$$

$$I_{min,k}^{v_{max}} = \left(\sum_{i=0}^{N-1} C_{e_2} A_e^i B_e + D_{e_2} \right)^{-1} \left(v_{max} - C_{e_2} A_e^N \begin{bmatrix} z_k \\ v_{1,k} \end{bmatrix} - E_{e_2} \right). \tag{4.3d}$$

where r, k_t and α are the radius, thermal conductivity, and thermal diffusivity of the battery, respectively; typically, these parameters are not significantly affected by operating temperature. However, the convection coefficient, h, is highly influenced by cooling or heating condition and hence it is chosen to be a parameter to be estimated. States and parameter of the thermal dynamics for the on-line estimation are $x_T = [\bar{T}, \bar{\gamma}]'$ and $\theta_T = h$, respectively. Refer to Chapter V for a list of nominal values of the parameters of the model when the cell under consideration is an A123 26650 LFP cell.

The heat generation rate, $\dot{q}$, is determined by the electrical dynamics as

$$\dot{q}_k = I_k^2 R_{s,k} + \frac{v_{1,k}^2}{R_{1,k}} - I_k \bar{T}_k \frac{\Delta S_k}{F}, \tag{4.4}$$

where F is Faraday's constant, 96485.3365 C/mol; ΔS denotes the entropy change of the battery and is related to a certain amount of energy that needs to be reversibly absorbed or released to balance the whole reaction inside the battery.

4.2 Power Capability Estimation

In determining power capability, the following factors are considered

1. The thermal and electrical dynamics of a Li-ion battery are intrinsically coupled.
2. The internal resistance and the rate of change of internal resistance with respect to temperature decrease with increasing temperature.
3. For a galvanostatic operation, any arbitrary increase in battery temperature causes reduced internal losses, and subsequently generates less heat.
4. Over a short time horizon, changes in temperature and SOC are assumed to be bounded.

The above statements are valid insofar as the battery temperature does not exceed the threshold temperature at which thermal runaway is initiated. Since thermal dynamics are much slower than electrical dynamics, in determining the power capability, the thermal and electrical constraint problems are addressed separately.

To calculate the power capability of the battery, an Algebraic Propagation (AP) method is applied with information about states and parameters from the state-parameter estimators developed in the following section. The AP method computes a constant input which leads to that none of constraints are violated in N future steps. To apply the AP method to the electrical system, the output of the system (4.1) needs to be linearized and is expressed as:

$$\begin{bmatrix} z_{k+1} \\ v_{1,k+1} \end{bmatrix} = A_e(R_{1,k}, C_{1,k}) \begin{bmatrix} z_k \\ v_{1,k} \end{bmatrix} + B_e(R_{1,k}, C_{1,k}) I_k, \tag{4.5a}$$

$$\begin{bmatrix} z_k \\ v_{t,k} \end{bmatrix} = C_e \begin{bmatrix} z_k \\ v_{1,k} \end{bmatrix} + D_e I_k + E_e, \tag{4.5b}$$

where matrices C_e, D_e and E_e are defined as

$$C_e = \begin{bmatrix} C_{e_1} \\ C_{e_2} \end{bmatrix} = \begin{bmatrix} 1 & 0 \\ \frac{\partial v_{oc}(z)}{\partial z}\Big|_{z=z_k} & -1 \end{bmatrix}, \tag{4.6}$$

$$D_e = \begin{bmatrix} D_{e_1} \\ D_{e_2} \end{bmatrix} = \begin{bmatrix} 0 \\ -R_{s,k} \end{bmatrix}, \tag{4.7}$$

$$E_e = \begin{bmatrix} E_{e_1} \\ E_{e_2} \end{bmatrix} = \begin{bmatrix} 0 \\ v_{\text{oc}}(z_k) - \frac{\partial v_{oc}(z)}{\partial z}\Big|_{z=z_k} z_k \end{bmatrix}. \tag{4.8}$$

The maximum permissible currents accounting for electrical constraints such as SOC and voltage limits, z_{min}, z_{max}, v_{min}, and v_{max}, are determined respectively as in Eqn. (4.3). Each of those equations, in sequence, help compute the value of constant current that will drive (a) SOC to lower limit (b) SOC to upper limit (c) terminal voltage to lower limit (d) terminal voltage to upper limit; at the end of a N step prediction window. The derivation of each sub-equation in Eqn. (4.3) follows the same steps; thus for simplicity, the derivation of Eqn. (4.3a) is provided below. At any instant k, the N-step ahead prediction of the various states assuming a constant current, I, is given by

$$\begin{bmatrix} z_{k+N} \\ v_{1,k+N} \end{bmatrix} = A_e^N \begin{bmatrix} z_k \\ v_{1,k} \end{bmatrix} + \left(\sum_{i=1}^{N-1} A_e^i B_e \right) I. \tag{4.9}$$

If the value of SOC at the end of N samples is equal to z_{min}, then the value of continuous discharge charge current ($I_{max,k}^{z_{\text{min}}}$) that drives the SOC to lower boundary is computed by enforcing the terminal constraint on Eqn. (4.9); i.e.

$$z_{min} = C_{e_1} \begin{bmatrix} z_{k+N} \\ v_{1,k+N} \end{bmatrix} + I_{\text{max},k}^{z_{min}} D_{e_1} + E_{e_1}. \tag{4.10}$$

Now substituting Eqn. (4.9) into the above and collecting terms, Eqn. (4.3a) is derived.

For the battery thermal system, the representation in Eqn. (4.2) is re-written as the following equations:

$$\begin{bmatrix} \bar{T}_{k+1} \\ \gamma_{k+1} \end{bmatrix} = A_t(h_k) \begin{bmatrix} \bar{T}_k \\ \gamma_k \end{bmatrix} + B_{t_1}(h_k)\mu_k + \xi_{1,k}, \tag{4.11a}$$

$$T_{c,k} = C_{t_1}(h_k) \begin{bmatrix} \bar{T}_k \\ \gamma_k \end{bmatrix} + \xi_{2,k}, \tag{4.11b}$$

where

$$\mu_k = I_k^2 R_{s,k} - I_k \bar{T}_k \frac{\Delta S_k}{F}, \tag{4.12a}$$

$$\xi_{1,k} = B_{T_1}(h_k) \begin{bmatrix} \frac{v_{1,k}^2}{R_{1,k}} \\ T_{\infty,k} \end{bmatrix}, \tag{4.12b}$$

$$\xi_{2,k} = D_{T_1}(h_k) T_{\infty,k}. \tag{4.12c}$$

When the prediction period is short, the battery SOC and temperature do not change significantly over the prediction horizon. Thus, it is reasonable to assume that the entropy change and internal resistance are constant over the prediction horizon; i.e. $R_{s,j|k} \approx R_{s,k}$ and $\Delta S_{j|k} \approx \Delta S_k$ for $j = k, k+1, \ldots, k+N$. In addition, the ambient temperature and convection coefficient do not change rapidly and hence are assumed to be constant, i.e. $T_{\infty,j|k} \approx T_{\infty,k}$ and $h_{j|k} \approx h_k$ for $j = k, k+1, \ldots, k+N$. Lastly, an estimate of heat generation by the polarization voltage over the prediction horizon is obtained through model iteration using the maximum permissible current at previous sampling time,

$$\bar{\xi}_{1,k} = \max\{\xi_{1,k}, \xi_{1,k+N}\}. \tag{4.13}$$

These approximations make it easy to handle the nonlinearity in the expression of heat generation rate using a quadratic term I_k^2 and a bilinear term $I_k \bar{T}_k$.

Then, the maximum of the input $\mu_{\mathrm{max},k}^q$, $q \in \{\mathrm{dch}, \mathrm{chg}\}$, which is described by considering the maximum core temperature $T_{c,\mathrm{max}}$, is determined as follows:

$$\mu_{max,k}^{dch} = \left(\sum_{i=0}^{N-1} C_T A_T^i B_T \right)^{-1} \left(T_{c,max} - C_T A_T^N \begin{bmatrix} \bar{T}_k \\ \gamma_k \end{bmatrix} - \sum_{i=0}^{N-1} C_T A_T^i \bar{\xi}_{1,k}^{dch} - \xi_{2,k} \right), \tag{4.14a}$$

$$\mu_{max,k}^{chg} = \left(\sum_{i=0}^{N-1} C_T A_T^i B_T \right)^{-1} \left(T_{c,max} - C_T A_T^N \begin{bmatrix} \bar{T}_k \\ \gamma_k \end{bmatrix} - \sum_{i=0}^{N-1} C_T A_T^i \bar{\xi}_{1,k}^{chg} - \xi_{2,k} \right), \tag{4.14b}$$

where superscripts *dch* and *chg* represent battery discharge and charge, respectively. By substituting Eqns. (4.14) into Eqn. (4.12a), the maximum permissible currents during battery discharge and charge are determined respectively by the following equations

$$I^{T_{max}}_{max,k} = \frac{\frac{\bar{T}_k \Delta S_k}{F} + \sqrt{\left(\frac{\bar{T}_k \Delta S_k}{F}\right)^2 + 4R_{s,k}\mu^{dch}_{max,k}}}{2R_{s,k}}, \tag{4.15a}$$

$$I^{T_{max}}_{min,k} = \frac{\frac{\bar{T}_k \Delta S_k}{F} - \sqrt{\left(\frac{\bar{T}_k \Delta S_k}{F}\right)^2 + 4R_{s,k}\mu^{chg}_{max,k}}}{2R_{s,k}}. \tag{4.15b}$$

Maximum discharge and charge currents accounting for all constraints are calculated with

$$I_{max,k} = \min\{I^{z_{min}}_{max,k}, I^{v_{min}}_{max,k}, I^{T_{max}}_{max,k}\}, \tag{4.16a}$$

$$I_{min,k} = \max\{I^{z_{max}}_{min,k}, I^{v_{max}}_{min,k}, I^{T_{max}}_{min,k}\}. \tag{4.16b}$$

Finally, the power capability $\{P_{max,k}, P_{min,k}\}$ is computed by the product of the maximum allowable current and terminal voltage after N future sample steps expressed as

$$P_{max,k} = I_{max,k} \cdot v^{dch}_{t,k+N|k}, \tag{4.17a}$$

$$P_{min,k} = I_{min,k} \cdot v^{chg}_{t,k+N|k}, \tag{4.17b}$$

where the predicted terminal voltage $v^{q}_{t,k+N|k}$, $q \in \{dch, chg\}$ is calculated with

$$\begin{aligned} v^{dch}_{t,k+N|k} &= v_{oc}\left(z_k - \frac{I_{max,k} N \Delta t}{Q_b}\right) - I_{max,k} R_{s,k} \\ &\quad - e^{\frac{-N\Delta t}{R_{1,k}C_{1,k}}} v_{1,k} - I_{max,k} R_{1,k}\left(1 - e^{\frac{-N\Delta t}{R_{1,k}C_{1,k}}}\right), \\ v^{chg}_{t,k+N|k} &= v_{oc}\left(z_k - \frac{I_{min,k} N \Delta t}{Q_b}\right) - I_{min,k} R_{s,k} \\ &\quad - e^{\frac{-N\Delta t}{R_{1,k}C_{1,k}}} v_{1,k} - I_{min,k} R_{1,k}\left(1 - e^{\frac{-N\Delta t}{R_{1,k}C_{1,k}}}\right). \end{aligned}$$

4.3 State and Parameter Estimation

The power capability of a battery as described in Section 4.2 relies on the accurate description of the battery's electro-thermal dynamics. The challenge of estimating model states and parameters in the context of power capability estimation has been extensively studied; broadly, the most common methods employed can be classified as being based on dual [77] or joint estimation [73, 74].

In this section, the problem of state-parameter estimation is addressed by describing a method to partition the augmented-state-parameter-space (aSPs) for dual estimation; the partitioning is inspired by spectral techniques that have thus far been used for off-line parametrization of models; and the resulting partitions are worked upon by a cascading estimator. To that end, this section is structured as follows – Section 4.3.1 describes the partitioning technique in general. Section 4.3.2 specializes the method to the problem of state-parameter estimation for the electro-thermal model and describes the overall structure of the estimator.

4.3.1 Partitioning of the augmented-state-space

Joint estimation in the aSPs is generally computationally intensive and is less preferred to dual estimation because the latter is believed to reduce the influence of poor *a priori* knowledge of initial parameters, and poor measurements on state estimates [77, 84, 85]. In a typical implementation of a dual estimator, the aSPs is partitioned into two groups consisting of states and parameters respectively. In this chapter, based on the notion of observability/estimability, an alternate criterion to partition the augmented-state-parameter-space (aSPs) is suggested. The proposed partitioning technique is a direct extension of standard off-line parameter estimation techniques [78, 86].

Consider a general dynamic system whose evolution is described by the following equations

$$x_{k+1} = f(x_k, \theta_k, u_k), \tag{4.18a}$$

$$y_k = g(x_k, \theta_k, u_k), \tag{4.18b}$$

where $f,\, g \in \mathcal{C}^1(\mathbb{R}^{n_x} \times \mathbb{R}^{n_p} \times \mathbb{R}^{n_u})$. Suppose it is of interest to estimate the states, x, and the parameters, θ, in the presence of exogenous inputs, u; the aSPs description for the estimator is defined as following:

$$\tilde{x}_{k+1} = f(\tilde{x}_k, u_k), \tag{4.19a}$$

$$y_k = g(\tilde{x}_k, u_k), \tag{4.19b}$$

where $\tilde{x} = [x,\, \theta]' \in \mathbb{R}^{n_x + n_p}$. The parameters, θ, are assumed time-invariant or slow-varying, over a short window of data of length N samples. State-parameter estimation problems can in general be re-cast as one of finding the initial condition of states and parameters in the form of a least squares estimation (LSE) problem [87],

$$\tilde{\theta} = \arg\min_{\tilde{\theta}} \|Y - \hat{Y}(\tilde{\theta}, U)\|^2, \tag{4.20}$$

where $\tilde{\theta} = [x_0,\, \theta]'$; x_0 are the initial conditions of states, and θ are parameters of the dynamical system, U is the vector of inputs $U = [u_1, \ldots, u_N]'$, Y is the vector of measurements $Y = [y_1, \ldots, y_N]'$ and $\hat{Y}$ is the output of the model $\hat{Y}(\tilde{\theta}) = [\hat{y}_1(\tilde{\theta}), \ldots, \hat{y}_N(\tilde{\theta})]'$. In the following discussion, the Fisher Information Matrix (FIM) is used as a tool to asses the estimability of parameters $\tilde{\theta}$[1].

The FIM, F, is typically constructed by stacking a sequence of sensitivity coefficients. In the context of the LSE problem in Eqn. (4.20), $F = H'H$ where

$$H(\hat{\tilde{\theta}}, Y, U) = [\mathrm{diag}(Y)]^{-1} \begin{bmatrix} \frac{\partial y_1(\tilde{\theta},U)}{\partial \tilde{\theta}_1} & \cdots & \frac{\partial y_1(\tilde{\theta},U)}{\partial \tilde{\theta}_{n_x+n_p}} \\ \vdots & \ddots & \vdots \\ \frac{\partial y_N(\tilde{\theta},U)}{\partial \tilde{\theta}_1} & \cdots & \frac{\partial y_N(\tilde{\theta},U)}{\partial \tilde{\theta}_{n_x+n_p}} \end{bmatrix} \Bigg|_{\tilde{\theta}=\hat{\tilde{\theta}}} [\ \mathrm{diag}(\hat{\tilde{\theta}})],$$

$\hat{\tilde{\theta}}$ is the best *a priori* estimate of $\tilde{\theta}$, and it has been assumed that measurement uncertainty, if any, is additive white gaussian with unit variance. Observe that the Jacobian is left multiplied by a diagonal matrix of measurements from the model, and is multiplied from the right by a diagonal matrix of the values of the various parameters. The Jacobian matrix is thus '*scaled*' to normalize entries and remove any units associated with entries[2].

The FIM provides useful information about the estimation problem – the rank of F presents the number of estimable parameters; an ill-conditioned F indicates that some parameters are not robustly estimable; the inverse of F is termed the covariance matrix and is related to the variance of estimates as derived by the best unbiased estimator (the Cramér-rao bound). The information matrix has been used for yet another purpose – to infer the relative significance of estimating parameters from the provided data. This form of analysis, typically reserved for off-line parametrization, has been discussed in literature (refer to [78–81] and references therein); studies on off-line estimability typically culminate in a method to partition the set of parameters to be estimated, $\tilde{\theta}$, into groups. Herein, a similar partitioning technique is utilized to design the on-line estimator.

A quantitative metric to assist in ranking parameters based on their relative significance on the measurement and hence their estimability from the measurement can be defined by using Principal Component Analysis (PCA) [86, 89] on FIM. In the following discussion, for simplicity of expressions, it is assumed that the F has distinct eigenvalues. Let $r = n_x + n_p$ and $\Lambda = \{\lambda_1, \ldots, \lambda_r\}$ be the ordered set (increasing) of eigenvalues of the F, and $\{E_1, \ldots, E_r\}$ be the set of eigenvectors arranged to match the corresponding eigenvalue. The principal components of H, the eigenvectors of F, are ordered as follows – $\forall\, i, j \in \mathbb{N}_r$, if $i < j$, E_j explains the variation in the data better than E_i. The relative significance of principal components is a reflection of the corresponding directions along which there is a larger variation. A measure of the significance of the i^{th} parameter, $\tilde{\theta}_i$, is given by

$$\eta_i = \frac{\sum_{k=1}^{r} |\lambda_k \cdot (E_k)_i|}{\sum_{k=1}^{r} |\lambda_k|}, \tag{4.21}$$

---

[1] For the relation between FIM and local nonlinear observability, refer [88].

[2] Viewed differently, one could say that the various parameters—each a random variable—are scaled to create new random variables and the Jacobian is with respect to the new random variables.

Algorithm 1: Cascading estimation algorithm (SISO)

```
**Data**: $Y, U$ and $\tilde{\theta}_{k-1}$
Initialize $\tilde{\theta}_k$;
Build $G_1$ and $G_2$;
Set $i = 1$;
while $i \leq 2$ do
    val$(G_i) = \psi_i(G_1, G_2, Y, U)$;
    $i = i + 1$;
end
Update $\theta_k$ from $G_1$ and $G_2$.
where $\psi_i$ is an estimator designed for group $G_i$.
```

where $(E_k)_i$ denotes the i^{th} row of E_k. Note that $0 \leq \eta_i \leq 1$ and reflects the difficulty of estimating the i^{th} parameter by itself; if $\eta_i > \eta_j$, the i^{th} parameter is more estimable than the j^{th} parameter.

Based on the significance metrics, the overall estimator can be described as follows. Let Θ be the set of parameters $\tilde{\theta}$, elements of the aSPs and suppose ζ is the critical threshold about which the parameters are partitioned. For notational convenience it is assumed that $\zeta \in [0, 1]$. Then two vectorized groups G_1 and G_2 can be defined as follows

$$G_1 = \text{vec}(\{\theta_i \in \Theta \mid \zeta \leq \eta_i \leq 1\}), \tag{4.22a}$$

$$G_2 = \text{vec}(\Theta \backslash G_1). \tag{4.22b}$$

The on-line estimation problem at every update instant k is depicted in Alg. 1. At each update instance, estimates of the value taken by elements in the aSP are updated in sequence with groups consisting of more significant elements being updated earlier than groups with less significant elements. In Alg. 1, $\tilde{\theta}_{k-1}$ is the estimate of every element of aSP using the information available until instance $k-1$; a priori estimates of $\tilde{\theta}_k$ are derived from $\tilde{\theta}_{k-1}$ using the dynamics in Eqn. (4.19). This is followed by initializing the values of elements in G_j using the a priori estimates of $\tilde{\theta}_k$. The value of members of each group are subsequently updated using measurement information of inputs and outputs (U and Y) and a priori estimates; this is achieved by using estimator ψ_i associated with group G_i. The ψ_is in the algorithm are estimators designed specific to group G_is and are chosen such that the extent to which measurements influence the updates decreases as the group number increases. At each instant k, as such, the following equality holds

$$e_k^2 \leq e_k^1,$$

where e_k^1 is the output prediction error having updated G_1 and G_2 is the total output prediction error after all states and parameters have been updated. The availability of individually tunable parameters for each group is an additional degree of freedom that the

```
Algorithm 2: Ranking states/parameters
    Data: Current, output and state trajectories associated with a drive-cycle
    Result: $\bar{\eta}$, the average significance vector
    Let $X$ be the states of interest;
    Set $L :=$ length of drive-cycle;
    Set $n_{\tilde{\theta}} = \dim(\theta)$;
    Set $n_h := 2n_{\tilde{\theta}} + 1$;
    Set $i = 1$;
    while $i \leq L - n_h + 1$ do
        $H = H(X(i), Y_i^{i+n_h-1}, U_i^{n_h-1})$;
        $F = H'H$;
        $\forall j \in \mathbb{N} \cap [1, n_\theta]$, $\Upsilon_{i,j} = \eta_j$;
    end
    $\bar{\eta} := \bar{\Upsilon}'$;
    where $\bar{\Upsilon}$ is the row average of the columns of $\Upsilon$ and $Y_i^{i+a}$ represents a vector
    consisting of elements $i$ through $i + a$ of $Y$.
```

designer can utilize to address the problem that typically attributed to joint estimation; by de-tuning the estimators associated with G_2, the impact of measurement noise on the less observable states/parameters can be reduced.

Remark IV.1. As elements in each group have comparable influence on the measured output, in our experience, tuning individual estimators is simpler than when the cascading structure was not adopted.

4.3.2 State-parameter estimation of the electro-thermal model

The previous subsection presented the architecture of the estimator considered in this study — the aSPs was partitioned based on metrics derived from the FIM of the initial condition estimation problem. This subsection addresses the problem of state-parameter estimation of the electro-thermal model.

Table 4.1: Significance of States and Parameter to Outputs over Different Input Profiles based on Principal Component Analysis

Cycle	Electrical					Thermal		
	$\bar{\eta}_z$	$\bar{\eta}_{v_1}$	$\bar{\eta}_{R_s}$	$\bar{\eta}_{C_1}$	$\bar{\eta}_{R_1}$	$\bar{\eta}_{\bar{T}}$	$\bar{\eta}_{\bar{\gamma}}$	$\bar{\eta}_h$
UAC	0.485	0.170	0.682	0.008	0.002	0.996	0.027	0.078
ECC	0.455	0.189	0.560	0.007	0.002	0.996	0.016	0.081
HD-UDDS	0.364	0.199	0.456	0.005	0.003	0.996	0.016	0.081

$\bar{\eta}_*$ is the average significance metric corresponding to state/parameter $*$, over the entire drive-cycle. Refer to Section 4.1 for a list of all parameters.

Fundamental to the application of the cascading algorithm in Alg. 1, is the availability of the significance metric η. In off-line parametrization problems, the entire trajectory of the inputs and outputs are completely known and the ranking algorithm can be set-up as described in the previous section; however, for on-line estimation problems, particularly for nonlinear estimation, when the employed estimator works with a limited data-set, the parameter significance ranking has to be performed dynamically using a window of data. However, since a BMS platform, in general, does not have sufficient computational power, the expected influence of parameters is computed off-line by generating a meaningful set of data as described below.

The average significance of each element in the aSPs over which the estimator operates is computed by utilizing standard drive-cycles. For each drive-cycle, the model of the integrated SHEV presented in [90] is used to generate the trajectory of battery currents. The generated current profile is in-turn fed to the battery pack model and the resulting output voltage and the trajectories of the internal states and parameters are recorded similarly to [41]. Taking into account the minimum number of samples required to estimate n parameters from data, $2n + 1$, as suggested in [91], the information matrix is computed along the trajectory of the states and the associated significance of each element of aSPs is computed as described in Alg. 2. The significance metrics, computed at each instance based on a receding history, are then averaged to compute the significance metric over the entire drive-cycle.

Figures 4.3(a) and 4.3(b) present the evolution of the significance metric associated with each element of the aSPs, for both the thermal and electrical sub-systems. The metrics are evaluated over a rolling data-set obtained from driving the heavy-duty vehicle model to follow the *Urban Assault Cycle* (UAC) [90]. The first sub-plot of both figures traces the values of the significance metrics, while the second subplot provides an indication of the relative ranking of the significance metrics at every time instant; it should be noted that in the second plot, higher the relative rank, the more significant the parameter.

From Fig. 4.3(a), it is observed that the average temperature gradient, $\bar{\gamma}$, has the least influence on the surface temperature T_s. The surface temperature is structurally more influenced by the averaged temperature than by the thermal gradient as can be observed from system matrix C_{T_2} (Eqn. (4.2)). In addition, the influence of perturbation of h on the surface temperature is dominated by the ratio of thermal conductivity to radius; that is, when the battery with low thermal conductivity has small radius, it is expected that a change in convection coefficient does not lead to any discernable change in the surface temperature.

Unlike Fig. 4.3(a), Fig. 4.3(b) exhibits a slightly erratic pattern; however, the key traits are fairly predictable. As the influence of the parameters of the single R-C pair manifest themselves through the trajectory of the polarization voltage, it is expected that these parameters are not any more estimable than V_1. The contribution of V_1 to the terminal voltage is usually smaller than that of the series resistance and the open circuit voltage in

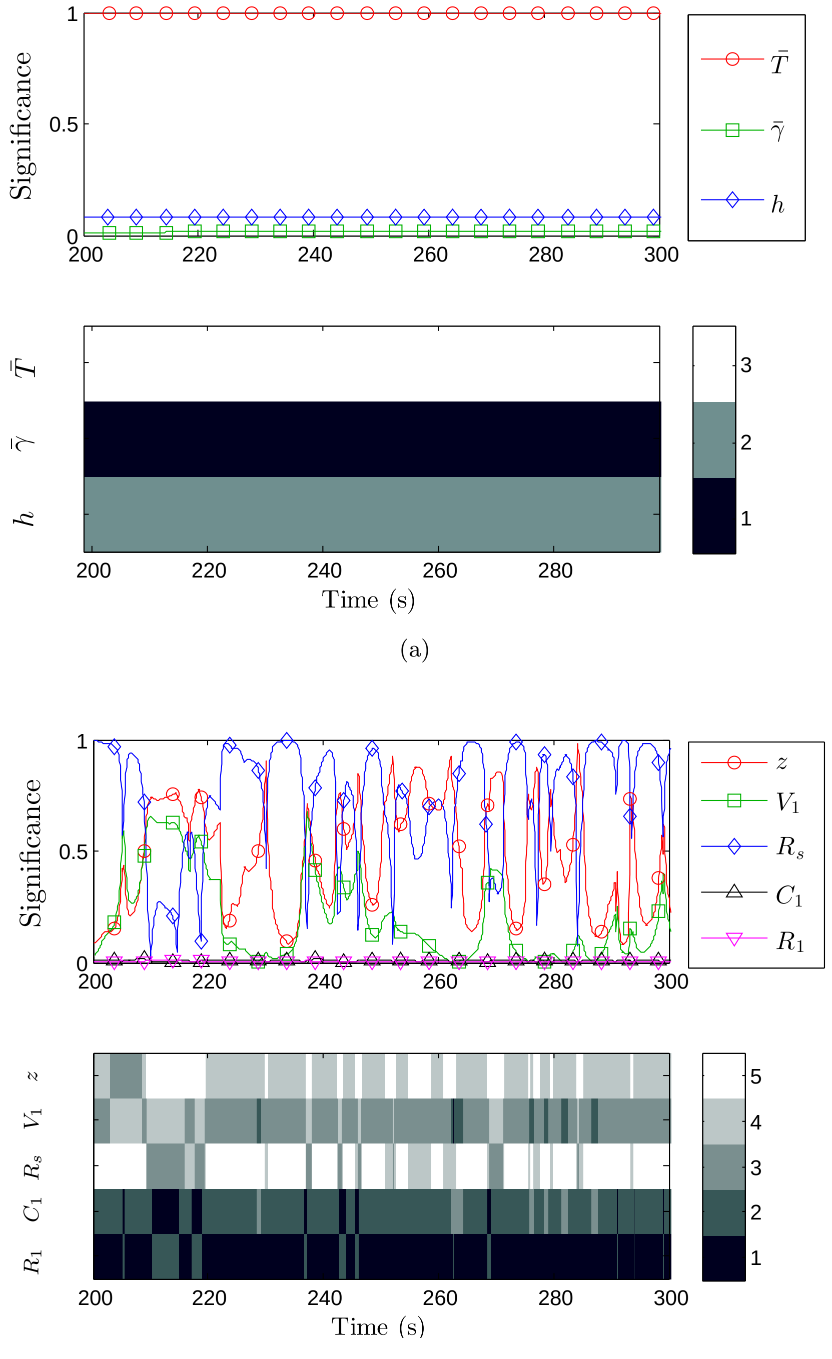

Figure 4.3: Measuring the significance of each state in the (a) thermal aSPs while measure the surface temperature alone (b) electrical aSPs, along the UAC.

terms of magnitude. This behavior arises from the current in hybrid vehicles being typically charge sustaining. Thus, on an average, R_s—the most significant parameter to compute the power capability [92]—is the most estimable parameter and the average significance

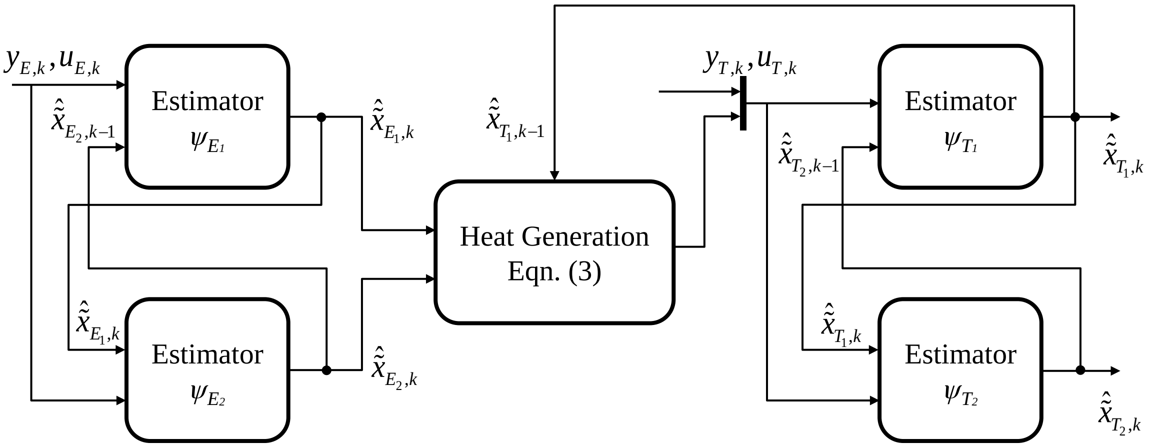

Figure 4.4: Schematic of state-parameter estimators with cascading structure

metric mirrors our expectations of estimability of states and parameters. Note that when the current is identically zero, the series resistance is not estimable; in producing the Fig. 4.3, it was assumed that the pack is always excited with some current.

Remark IV.2. It is worth re-iterating that the aSP of the electrical and thermal models of the battery are, in this study, partitioned based on average significance metrics. This choice was made by observing that the relative ranking of the various states/parameters—computed using Alg. 2—remains fairly constant. This is to be expected when the battery operates at or above room temperature, and in an HEV application wherein the SOC deviates about a nominal (not by much). However, for a generic non-linear system, if the solution trajectory was such that the local behavior at any two instances were sufficiently different, then the number of partitions and their members will have to be dynamically adjusted.

Remark IV.3. The parameters of the equivalent circuit model that are considered for online estimation has one glaring omission–battery capacity; an accurate estimate of the cell's capacity is assumed. The cell's measurable capacity is a function of temperature and the magnitude of power fed/drawn; an inaccurate estimate constitutes a structural uncertainty in the dynamics of the electrical sub-system. A discussion on the impact of this uncertainty on the quality of estimates and the structure of the estimator is deferred until a subsequent work.

4.4 Power Management in a Hybrid Electric Vehicle

This section investigates the performance of the proposed power capability estimator and its influence on the power management in a heavy-duty SHEV. The SHEV is simulated in the co-simulation framework in which the battery electro-thermal model and the on-line adaptive estimators are fully integrated to the vehicle model.

The HEV simulator is developed using a forward-looking approach as shown in Fig. 4.1. The driver, which takes the desired and actual vehicle velocities as inputs and provides propulsion or braking power demands, is modeled as a PI controller. Powertrain components such as the engine/generator, motor and battery are modeled with quasi-static maps.

In the simulator, power distribution is managed using a receding horizon controller whose instantaneous objective is to optimally minimize a weighted cost function: fuel consumption, SOC deviation, and power rate of the engine/generator. Details of the controller and its implementation are not of immediate relevance to the contents of this chapter and hence have not been included; they can be found in [90].

Extending the presentation in Section 4.3, Alg. 2 is iterated over three different standard heavy-duty vehicles' drive-cycles. Table 4.1 tabulates the computed expected relative influence for the thermal and electrical sub-systems over these drive-cycles. The mean significance of each state/parameter $*$ is denoted as $\bar{\eta}_*$. From a cursory glance at the numerical estimates of expected significance, one notes a self-evident partitioning of the aSPs and Table 4.2 collates the relevant groups for both sub-systems (using $\zeta = 0.1$ in Eqn. (4.22) for both the electrical and thermal sub-systems). With these partitions, independent estimators are designed for each group as shown in Fig. 4.4. Note that states/parameters of the electrical systems are estimated solely based on terminal voltage but those of the thermal systems are influenced by estimates of the electrical systems through Eqn. (4.4). To reflect this dependency, estimates of the electrical sub-system are updated prior to those of the thermal sub-system. The estimator of choice is the Extended Kalman Filter (EKF) summarized briefly in Appendix 2.2.

4.4.1 Estimator tuning

The average significance metric as presented in Section 4.3 enables one to determine quantitatively the relative extent to which variation in the measured data can be explained by each element of the augmented-state-space. Viewed differently, the inverse of the significance metric is roughly indicative of the relative variance of the estimates of the states and parameters obtained from the provided data; the EKFs used in this study are tuned with

Table 4.2: State, parameter, input and output of electrical and thermal systems for state-parameter estimation

	Electrical	Thermal
G_1	$\tilde{x}_{E_1,k} = [z_k,\, v_{1,k},\, R_{s,k}]'$	$\tilde{x}_{T_1,k} = \bar{T}_k$
G_2	$\tilde{x}_{E_2,k} = [R_{1,k},\, C_{1,k}]'$	$\tilde{x}_{T_2,k} = [\bar{\gamma}_k,\, h_k]'$
Input	$u_{E,k} = I_k$	$u_{T,k} = [\dot{q}_k,\, T_{\infty,k}]'$
Output	$y_{E,k} = v_{t,k}$	$y_{T,k} = T_{s,k}$

this information. Matrices Q and R which correspond to the process and measurement noise covariance matrices respectively are set as follows.

Recall that the average significance metric of parameter $*$, $\bar{\eta}_*$, was computed from the eigenvalues of the FIM and that the FIM matrix was computed from the '*scaled*' Jacobian. Scaling the Jacobian can be interpreted as scaling the parameters. To compute the expected variance of each parameter, the inverse of the significance metric has to be multiplied by the square of the scaling factor – the nominal value of the parameter.

Thus, the Q matrix for every estimator employed is defined as follows

$$\begin{aligned}
Q_{e_1} &= \text{diag}([1/\bar{\eta}_z, 1/\bar{\eta}_{v_1}, 1/\bar{\eta}_{R_s}])\cdot N_{e_1},\\
Q_{e_2} &= \text{diag}([1/\bar{\eta}_{C_1}, 1/\bar{\eta}_{R_1}])\cdot N_{e_2},\\
Q_{t_1} &= \text{diag}([1/\bar{\eta}_{\bar{T}}])\cdot N_{t_1},\\
Q_{t_2} &= \text{diag}([1/\bar{\eta}_{\bar{\gamma}}, 1/\bar{\eta}_h])\cdot N_{t_2},
\end{aligned}$$

where $\bar{\eta}_*$ is the mean significance metric of state $*$ presented in Table 4.1 and the matrix on the right of each expression, N, is a diagonal matrix comprised of the square of the nominal value of the corresponding parameter $*_{\text{nom}}$. Table 4.3 collates the nominal values of various parameters and the derived nominal matrices.

The values of $\bar{\eta}_*$'s are computed from the scaled version of the Jacobian, H (refer to Eqn. (4.21))[3]. The listed Q matrices correspond to the electrical (subscript E) and thermal (subscript T) subsystems respectively, and the numeral subscript corresponds to the group number. With the Q matrices defined as above, the values of the corresponding R matrices are tuned to minimize the mean error in individual estimates of state and parameters. The matrix R is tuned by scaling appropriately sized identity matrices and the mean error threshold is chosen to be 5%. In this particular application, the values of the corresponding R matrices are the following

$$R_{e_1} = 10^4, \qquad R_{e_2} = 10^4,$$
$$R_{t_1} = 10^{-4}, \qquad R_{t_2} = 10^3.$$

Table 4.3: Nominal values and derivative matrices

Parameter	z	V_1	R_s	C_1	R_1	$\bar{T}$	$\bar{\gamma}$	h
Value	0.5	0.1	10^{-3}	1.5×10^3	10^{-3}	30	30	15

$$\begin{aligned}
N_{e_1} &= \text{diag}([z_{\text{nom}}^2, {v_1}_{nom}^2, {R_s}_{nom}^2])\\
N_{e_2} &= \text{diag}([{C_1}_{nom}^2, {R_1}_{nom}^2])\\
N_{t_1} &= \text{diag}([\bar{T}_{nom}^2])\\
N_{t_2} &= \text{diag}([\bar{\gamma}_{nom}^2, h_{nom}^2])
\end{aligned}$$

---

[3] When a random variable is scaled, its variance is also quadratically scaled; the right diagonal matrices for Q are in place to normalize the entries of the corresponding states

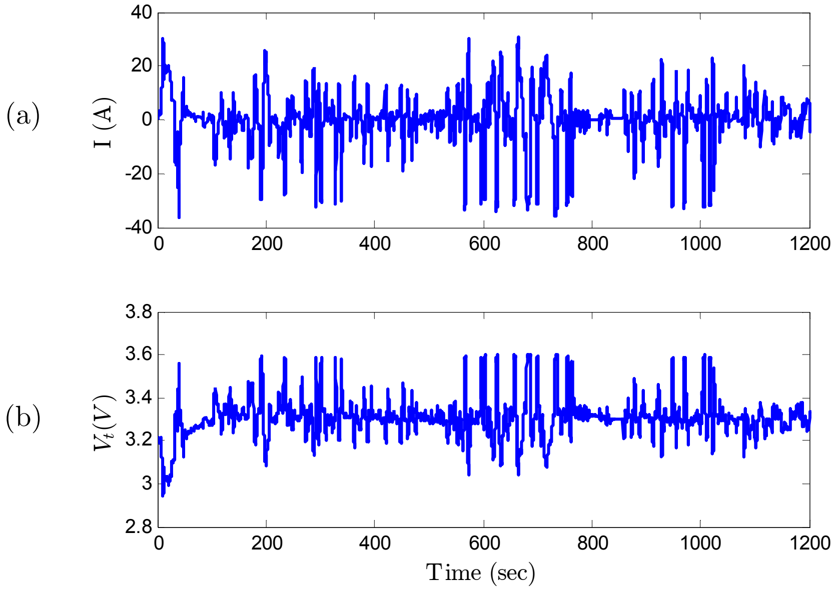

Figure 4.5: Input data to the estimators $\psi_{E\cdot}$ over the UAC: (a) current, (b) terminal Voltage

4.4.2 Results & discussion

The battery current and terminal voltage, which are inputs to the EKF-based estimator for the electrical system $\psi_{E\cdot}$, are shown in Fig. 4.5. To simulate realistic noise conditions, the current and voltage are contaminated with artificial Gaussian noises, i.e. $\sigma_I = 3 \times 10^{-3}$ and $\sigma_V = 1 \times 10^{-3}$. The results of state-parameter estimation for the electrical system are shown in Fig. 4.6(a)–(e), indicating that the estimator $\psi_{E\cdot}$ can simultaneously estimate SOC[4], polarization voltage, series resistance, polarization resistance and capacitance. It is observed that states and parameter in G_1 are estimated accurately and their convergence rates are relatively fast compared to those in G_2. Specifically, polarization resistance R_1 has the lowest estimation quality, which corresponds to the result that R_1 has the smallest significance metric among states and parameters.

Figure 4.7 shows the battery surface temperature and ambient temperature which are used as inputs to the EKF-based estimator for the thermal system $\psi_{T\cdot}$; similar to electrical system, Gaussian noises are artificially added to the surface and ambient temperatures, i.e. $\sigma_{T_s} = \sigma_{T_\infty} = 1.57 \times 10^{-3}$. To simulate malfunction of the cooling system, the convection coefficient is deliberately changed from 20 to 3 W/m^2-K at $t = 600$ second. This malfunction condition is simulated to assess not only the performance of the estimator ψ_T, but also the effectiveness of the power capability estimation. As seen from Fig. 4.8, the estimator is capable of providing accurate estimates of the states and parameter of the thermal system.

Remark IV.4. The controller employed by the simulator aims to minimize fuel consumption

---

[4] The battery SOC from the plant model is measured by using Coulomb Counting.

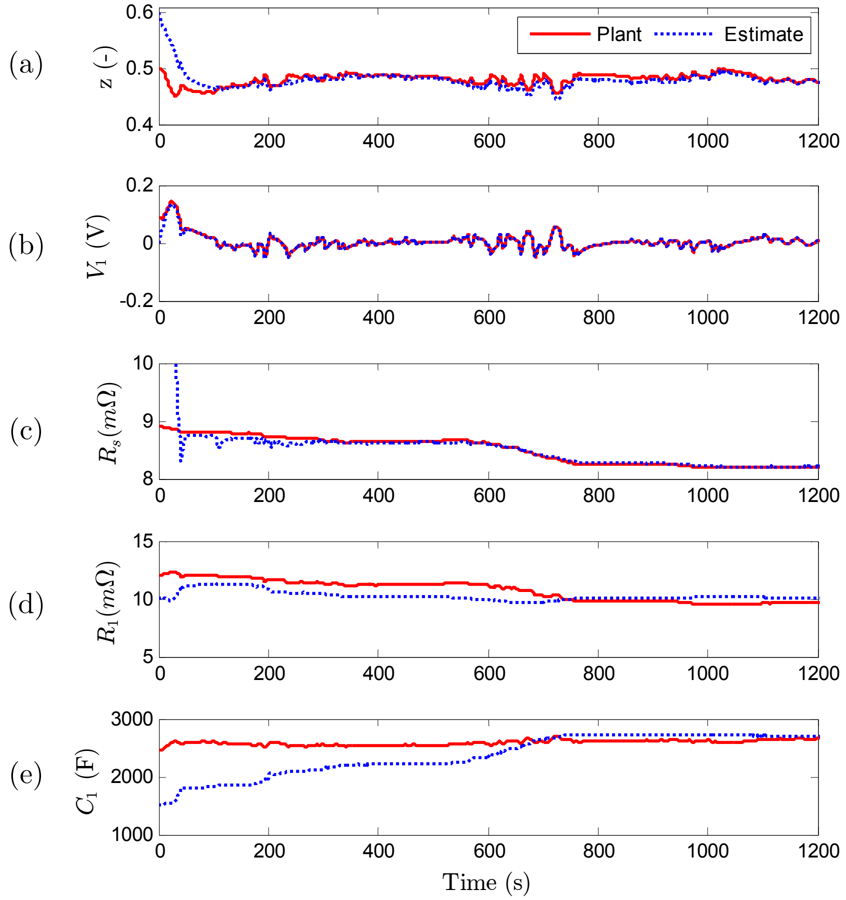

Figure 4.6: Performance of the estimator for the electrical system ψ_E: (a) SOC, (b) polarization voltage, (c) series resistance, (d) polarization resistance, (e) polarization capacitance

while also regulating battery SOC; the objective function of the controller is formulated as the weighted sum of fuel consumption and SOC deviation about the 0.5. Since the optimization problem is solved in receding horizon fashion without any terminal or invariant set constraints, the SOC at the end of the simulation should not be expected to be identical to 0.5 despite the general formulation being labeled *charge sustaining*. Additionally, if the thermal constraints are active, then the power that can be drawn and or deposited into the pack decreases, making SOC regulation more challenging.

The results of power capability estimation are shown in Figs. 4.9 and 4.10, which depict the battery power, SOC, terminal voltage and core temperature. Each subplot has the trajectory of the variable in blue and the bounds on its value in red. As shown in Fig. 4.9(a), the maximum battery power is limited by electrical-constrained power capability when the battery core temperature is lower than the target value of $T_{c,\max} = 45°C$. It is observed that the battery SOC and terminal voltage do not violate constraints (Fig. 4.9(b) and (c)).

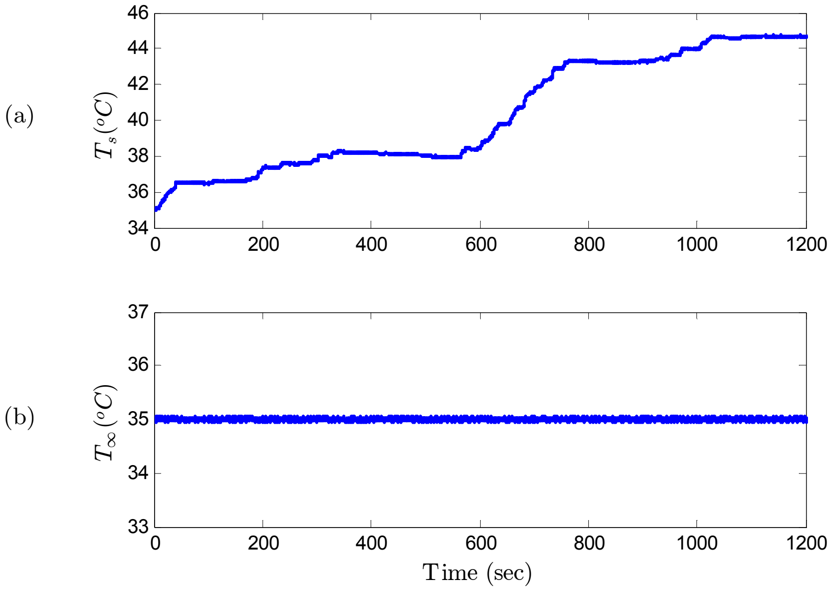

Figure 4.7: Input data to the estimator ψ_T over the UAC: (a) surface temperature; (b) ambient temperature

However, as the core temperature increases, thermal-constrained power capability becomes active and hence the battery power are effectively regulated between the maximum and minimum power limits. To highlight this performance, specific time periods from 1000 to 1100 seconds are shown in Fig. 4.10. Consequently, the core temperature is well regulated around the maximum temperature as illustrated in Fig. 4.10(d); $\max\{\hat{T}_{\mathrm{c}} - T_{\mathrm{c}}, 0\} = 0.02$. Considering that the accuracy of a thermocouple is usually less than 0.5°C and that the convection coefficient h is estimated from noisy measurements, it can be said that the performance of the proposed method is reasonably satisfactory.

Evidenced by the results from the model-in-the-loop simulation, it can be concluded that the developed estimation algorithms including states, parameters, and power capability are capable of providing accurate information about the battery. Thus, the safe and reliable operation of the power management system as well as the battery can be achieved.

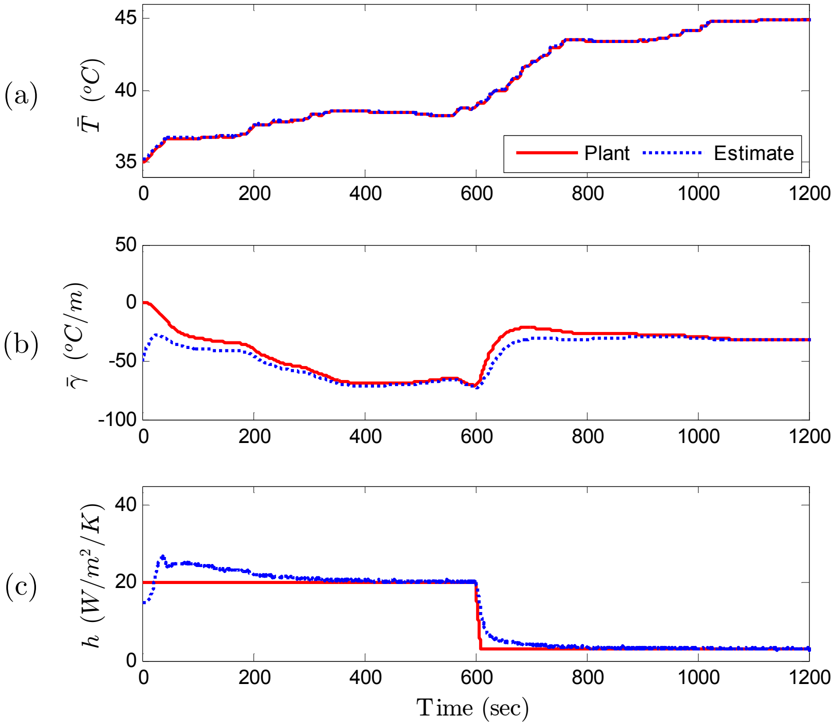

Figure 4.8: Performance of the estimator for the thermal system ψ_T.: (a) averaged temperature, (b) averaged thermal gradient, (c) convection coefficient

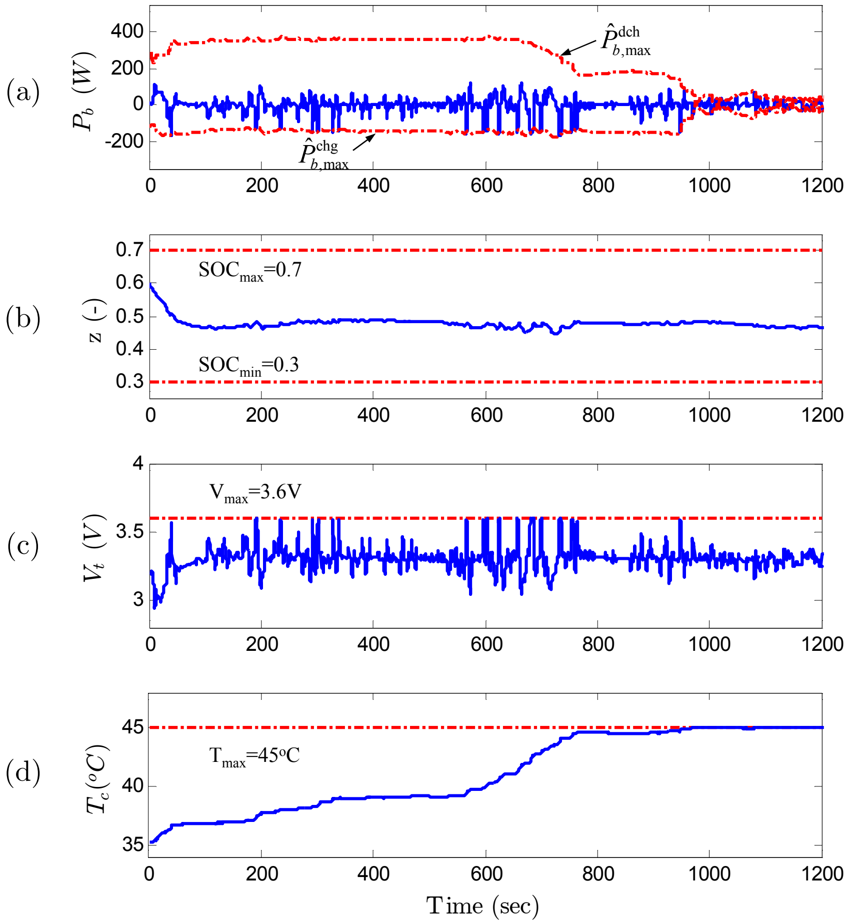

Figure 4.9: Performance of the power capability estimation: (a) power, (b) SOC, (c) terminal voltage, and (d) core temperature

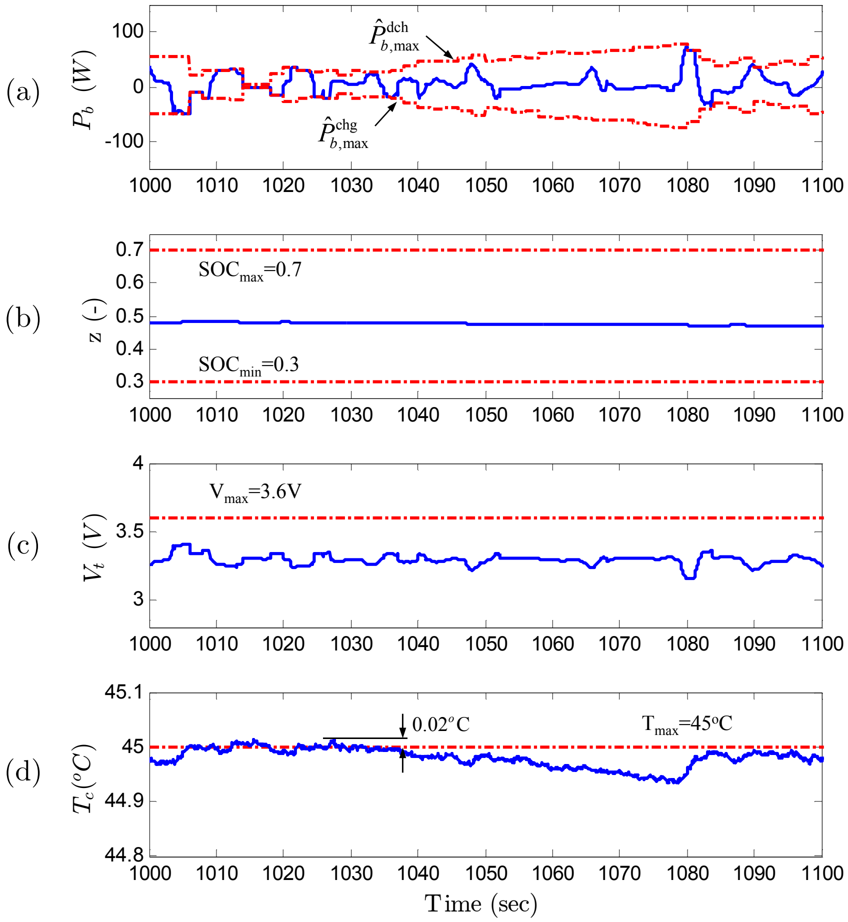

Figure 4.10: Performance of the power capability estimation from 1000 to 1100 seconds: (a) power, (b) SOC, (c) terminal voltage, and (d) core temperature

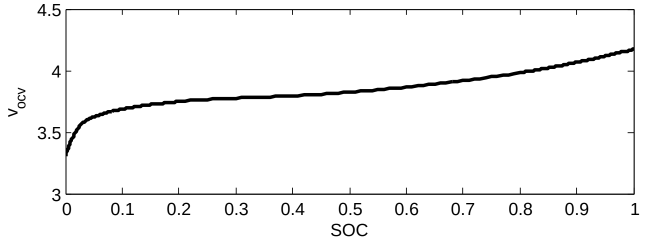

Figure 4.11: Graph of open-circuit-voltage, v_{ocv} of a Sanyo NMC cell

4.5 Experimental Estimator Performance Validation (Cold start)

In this section, we study the performance of the estimator design method on experimental data. To that end, a Sanyo NMC cell whose open circuit voltage is depicted in Fig. 4.11 is excited with eight back-to-back cold FTP cycles. The cell was initially in thermal equilibrium with the atmosphere at −5 °C; and the resulting terminal voltage and surface temperature were recorded at 10 Hz. It should be noted that the current profile was not generated using the SHEV simulator as the profile in Section 4.4; it was derived using the proprietary supervisory controller employed in a Ford C-max, and applied to the battery using a Bitrode FTV cycler. Consequently, the complete trajectories of current and voltage are not presented; instead, down-sampled versions are shown in Fig. 4.12.

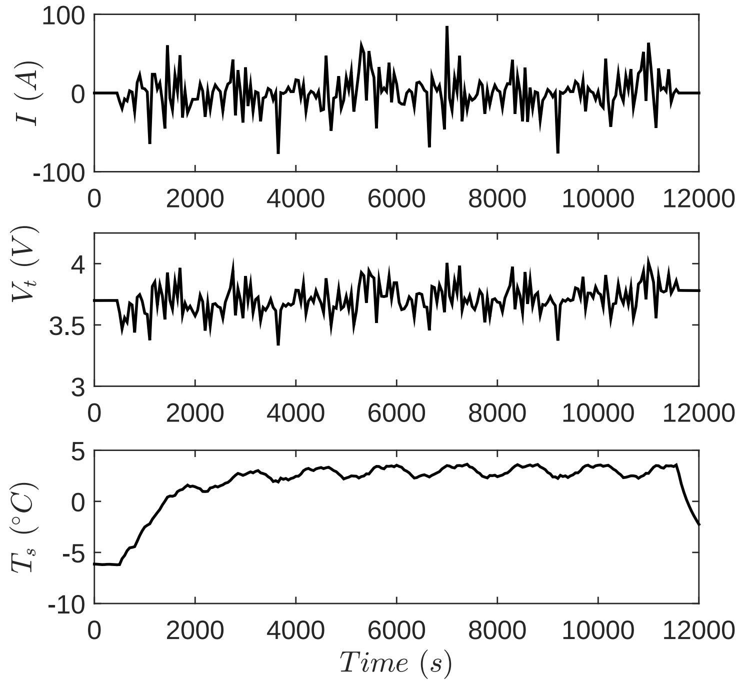

Figure 4.12: Down-sampled current excitation as derived from a cold FTP cycle, and resulting terminal voltage and surface temperature that resulted by the application of the current to a Sanyo 5 Ahrs NMC cell.

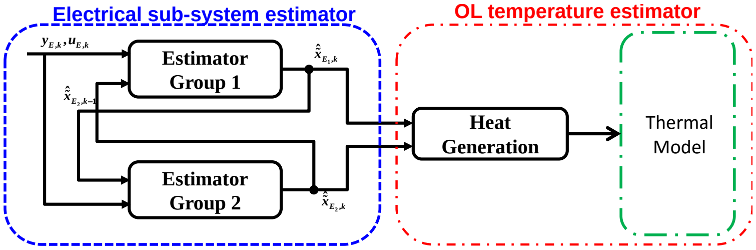

Figure 4.13: Structure of the cascading estimator

The Sanyo NMC cell is a prismatic cell (with a wound interior), unlike the cylindrical Iron Phosphate battery utilized in the sections afore. Since the Sanyo NMC does not admit the instrumentation of with a thermocouple in its interior with ease, developing a reliable model of its 3D spatial temperature distribution is hard; in [93], the authors develop one such model. It was observed that the temperature difference between any two position on the surface and on the interior was not significant, unless the excitation was persistent. Given the excitation presented in Fig. 4.12, it is surmised that the temperature in the cell will be almost uniform; thus it is adequate to model the thermal dynamics by a one-state model. Further, since the surface temperature is measured, there is no need to build an estimator for the battery's temperature. The derived thermal model is utilized to predict the surface temperature in open-loop. Figure 4.13 shows a modified version of the estimator schematic introduced in Sec. 4.3, tailored to this problem with a temperature predictor.

Using the methods described in Sec. 4.3, the values of the significance metrics for each of the state and parameters is derived. To derive the values of the significance metrics, it the spirit of keeping the estimator blind to the experiment and the data collected, a different

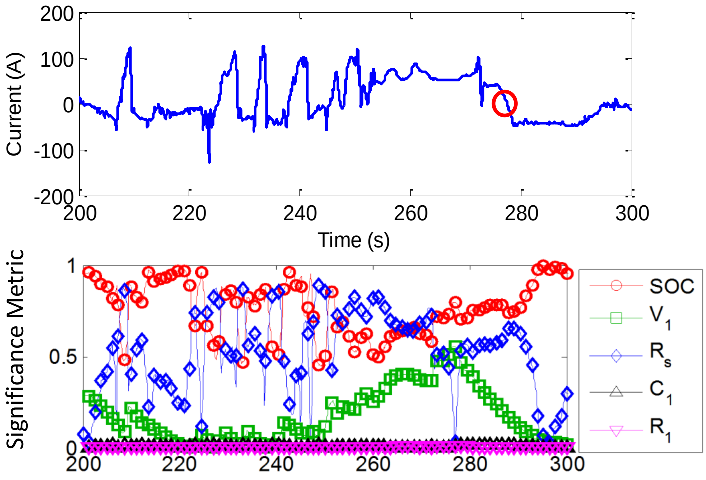

Figure 4.14: Computed relative sensitivities along the a current trajectory (using the expression in Eqn. (2.9))

η_{SOC}	η_{v_1}	η_{R_s}	η_{R_1}	η_{C_1}
0.746	0.201	0.500	0.0048	0.011

Table 4.4: Average significance metric for all states and parameters of the electrical subsystem

drive cycle (ECC) was employed. Figure 4.14 presents a snap-shot of the trajectories of the computed values and Tab. 4.4 lists the average significance metric.

The values in Tab. 4.4 suggest the following partitioning of the aSP:

$$G_1 \coloneqq \{R_s, SOC, V_1\},\; G_2 \coloneqq \{C_1, R_1\},$$

similar to the structure noted in Sec. 4.4. Using these values, Extended Kalman Filters for each group are designed as described in Appendix 2.1.2, and the state and parameters are estimated. The results are presented in Figs. 4.15 & 4.16.

The first subplot in Fig. 4.15 compares the estimated SOC against the *true* (Coulomb counting) SOC trajectory; the second subplot traces the error in SOC estimation, and the third subplot presents the relative estimation error. Estimates of the states and parameters of the electrical sub-system are used to compute the heat generated and are subsequently used to compute the evolution of the surface temperature of the cell; as depicted in Fig. 4.13.

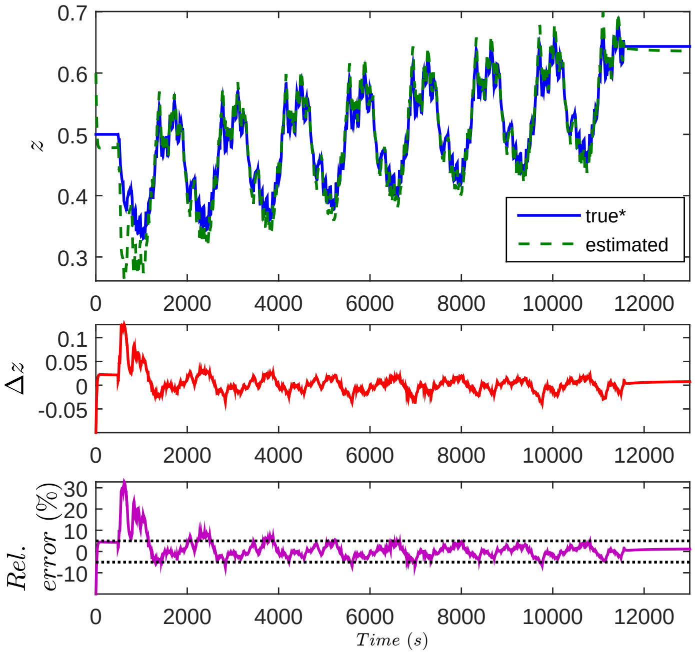

Figure 4.15: Trajectories of estimated SOC using the cascading observer. Subplot (1) traces the SOC trajectory, both estimate and *true*; (2) the error in SOC estimation; (3) relative SOC estimation error.

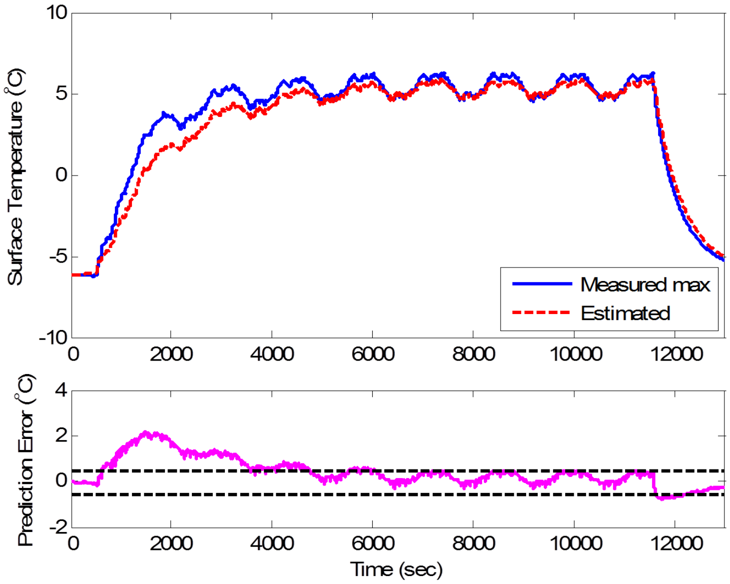

Figure 4.16: Measured and predicted surface temperature of the battery as resulting from applying the coldFTP cycle

The evolution of surface temperature and the open-loop estimated surface temperature are compared in Fig. 4.16, and the corresponding prediction error is also traced.

As evidenced by the error trajectories, the estimator performs satisfactorily by keeping the SOC error bounded to within 5% relative error after the initial transient. Estimates of surface temperature, a representative of the quality of estimates of the electrical parameters (because these parameters dictate how much heat is generated), converges to within 1 °C of the true temperature. That the temperature estimate converges could mean one or both of two things: (1) the DC-gain of the thermal dynamics model matches that of the battery, (2) the estimated parameters are indeed accurate. To assess if both of the above choices are true, then it would be worth comparing the estimated parameters with the parameters in the model of the battery derived in [93].

Remark IV.5. As tuned, the convergence rate of the thermal dynamics about 30 mins; it is possible that the dynamics of the parameter estimation is fairly slow. This time is much longer than the time it takes to warm the battery pack. Consequently, the parameter estimates might not be immediately employable for any warm-up strategy; however, the information so derived is still valuable. In [94] the authors assert that the parameters of the equivalent circuit model retain the same functional dependence on temperature at different battery ages. Thus, parameter estimates derived as the estimator *settles* is usable to predict the impact of aging and on the value of the model parameters at sub-zero temperatures.

4.6 Conclusion

This chapter presents a method to estimate the thermally and electrically constrained power capability of battery systems and demonstrates its application to the power management problem in an SHEV. The dynamics of the electrical and thermal sub-systems are not invariant and hence are adapted. To design estimators/adaptors, the relative estimability of the states and parameters of the electrical and thermal models was studied using Principal Component Analysis (PCA). Based on a ranking table derived from their relative estimability, the elements of the augmented-state-space model were grouped based on an average significance metric and individual estimators were designed for each group. The results of the model-in-the-loop simulation show that the proposed estimation algorithms can provide accurate information about the battery to the power management system and hence safe and reliable operation of the series hybrid electric vehicle can be achieved. A future work will explore the possibility of allowing for dynamically altering the number of groups and their membership based on the local significance of the various states and parameters.

CHAPTER V

Battery Warm-Up Using Bi-directional Pulses

In this chapter, the warm-up of Li-ion batteries from sub-zero temperatures, in the absence of an external energy source/heating system, is considered. Such a scenario is termed *standalone* operation.

Most techniques discussed in literature strive to warm the cell until a certain pre-specified cell temperature is reached. Since in most applications, the cell serves as a source of power, we use the cell's pulse power capability, instead of the temperature, as a condition to terminate the warm-up operation. In addition, we seek to investigate the feasibility of reaching the necessary power capability in an energy efficient manner.

Pulse power capability or state-of-power (SOP) is an estimated quantity whose accuracy is determined by the fidelity of the model that captures the electrical dynamics of the cell [95]. Modeling the electrical behavior of Li-ion cells at sub-zero temperatures, particularly at high current rates, is more challenging than emulating its thermal dynamics [28]. Thus, owing to the inherent relation between operating temperature and power capability, in this chapter, temperature rise is taken as a measurable surrogate. Then, the stated objective of increasing power capability can be re-written as one of effecting temperature rise in an energy conscious manner *until* the desired power can be delivered.

Maximizing temperature rise while regulating energy loss provides for certain desirable characteristics of the battery current. With heat generated being proportional to the input current, it follows that the candidate current profile be bi-directional to minimize cumulative discharge and achieve fast warm-up. Drawing bi-directional currents necessitates that a temporary energy reservoir for energy shuttling, such as an ultra-capacitor or another battery, be available (refer to 5.1). Since the bi-directional current includes a charging phase, it is important to note that charging the cell at low temperatures is challenging and imposes stringent charging current constraints (see [96, 97] for challenges at room temperature).

Charging Li-ion cells at sub-zero temperatures is difficult because of the reduced diffusivity in the anode that results in increased polarization and a drop in electrode overpotential [98,99]. From a control perspective, the propensity of charging currents to cause plating can be minimized by actively regulating the electrode overpotential. Pulsed charging is one of

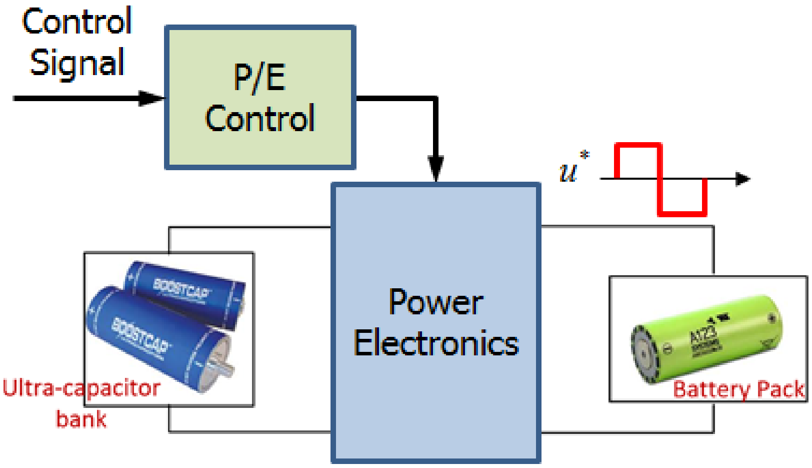

Figure 5.1: Schematic of the overall power circuit

the most widely adopted technique to slow down polarization and allow for more even ion distribution [100]. In this chapter, in addition to using bi-directional pulses, anode polarization is indirectly controlled by enforcing the magnitude of charging currents to be less than the discharging portion of the pulse.

This chapter attempts to study the feasibility of using computationally efficient models to improve the power capability of Li-ion cells in an energy efficient manner. This chapter is organized as follows. The models that are used to mimic the cell's electrical and thermal behavior are detailed in Section 5.1 and their parametrization is discussed in Section 5.2. The control problem is formulated in Section 5.3 and an example simulation is studied in Section 5.4. Conclusions and final remarks are made in Section 5.5.

5.1 Modeling

This section introduces the models of electrical and thermal dynamics adopted in this study. The dynamic behavior of a cylindrical (26650) LFP cell is captured using simple reduced order models. The validity of the chosen models for the application at hand is ascertained through experimental validation.

5.1.1 Electrical model

Over the decades, much effort has been expended in developing phenomenological models of the electrical dynamics. The more complex models are based on concentration theory, first proposed by Doyle, Fuller and Newman in [101]. Models so derived are hard to parameterize [80], have notable memory requirements and, are computationally intensive. On the other hand, equivalent circuit models have been widely adopted in literature and in practice, eg. [41] and references therein.

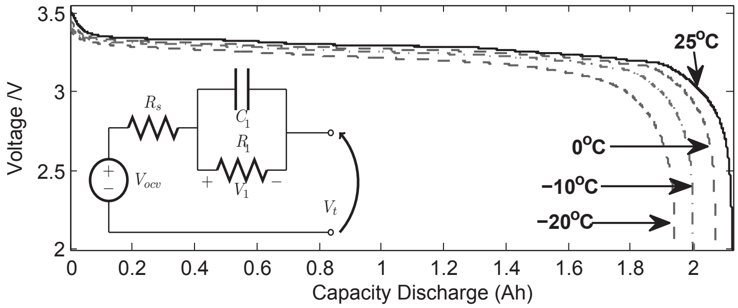

Figure 5.2: Relation between temperature, OCV and capacity, (inset) single R-C equivalent circuit representation of electrical dynamics

Small signal and local approximations of the dynamic behavior of electrochemical studies can be obtained by using impedance measurements [102]. Results of the impedance spectroscopy study conducted in [39] suggest that at low operating temperatures, for high frequencies of current, the Li-ion cell's electrical dynamics exhibits a first order characteristic. Thus, in this chapter, an equivalent circuit model whose dynamics is governed by Eqn. (5.1) is utilized to capture the electrical dynamics of the Li-ion cell. Note that the system Eqn. (5.1) describes is one of a Linear Parameter Varying system wherein the parameters are scheduled based on the state of charge (SOC), z, and the cell temperature T

$$\underbrace{\begin{bmatrix}\dot{z}\\ \dot{V}_1\end{bmatrix}}_{x_{el}} = \underbrace{\begin{bmatrix}0 & 0\\ 0 & -\dfrac{1}{R_1(T)C_1(T)}\end{bmatrix}}_{A_{el}} \begin{bmatrix} z\\ V_1\end{bmatrix} + \underbrace{\begin{bmatrix} -\dfrac{1}{3600\cdot Q_b(T)}\\ -\dfrac{1}{C_1(\cdot)}\end{bmatrix}}_{B_{el}} v_{el},$$

$$v_t = v_{oc}(z,T) + V_1 - R_s(\cdot)v_{el}. \tag{5.1}$$

where $v_{el} = I$ (sign convention – charge : negative; discharge : positive), Q_b is the temperature dependent capacity of the cell; v_t is the terminal voltage of the cell; v_{ov} is the Open Circuit Voltage (OCV), a function of SOC and cell temperature; and $R_s(\cdot)$ is the series resistance. Figure 5.2 presents an electric equivalent of the dynamical system in Eqn (5.1) and the dependence of C_b on temperature. State V_1 can be interpreted as being indicative of the bulk polarization in the cell; its time constant is determined by the pair $\{R_1, C_1\}$ which is assumed to be a function of SOC, cell temperature and current direction. In the interest of notational simplicity, in the remainder of the chapter, the dependence of model parameters on dynamic states and input is not explicitly stated when there is little room for confusion.

The power capability of a cell is defined as the product of the maximum continuous current that can be drawn over a fixed time interval without violating current and or voltage constraints. In this chapter, estimates of power capability for a pulse duration of N samples are computed in discrete-time using expressions provided in [92]. In discrete-time domain, denoting the linearized system matrices of the electrical model as A_{el}^d, B_{el}^d, C_{el}^d, D_{el}^d,

$$P_{cap,k} = V_{min} \left\{ \frac{V_{min} - V_{OCV}(z_k) + C_{el}^d L z_k - C_{el}^d (A_{el}^d)^N x_{el,k}}{C_{el}^d M_{el}^d + D_{el}^d} \right\}, \tag{5.2}$$

where V_{min} is the minimum permissable terminal voltage, $L = [1,\, 0,\, 0]'$, $M = \sum_{i=0}^{N-1} (A_{el}^d)^j B_{el}^d$ and N is the number of samples in the constant discharge pulse.

5.1.2 Thermal model

The thermal model of a cylindrical battery developed in [43] is taken to represent the thermal dynamics in this study. The model of the thermal dynamics when expressed in terms of the core (T_c), surface (T_s), ambient (T_{amb}) temperatures and rate of heat generation (q) is represented as

$$\begin{aligned} \dot{x}_{th} &= A_{th} x_{th} + B_{th} v_{th}, \\ y_{th} &= C_{th} x_{th} + D_{th} v_{th}, \end{aligned} \tag{5.3}$$

where the states represent temperature gradient across the radius ($\bar{\gamma}$) and average temperature ($\bar{T}$); $x_{th} = [\bar{T} \;\; \bar{\gamma}]^T$, $v_{th} = [q \;\; T_{amb}]^T$ and $y_{th} = [T_c \;\; T_s]^T$. System matrices A_{th}, B_{th}, C_{th}, and D_{th} are defined as follows:

$$\begin{aligned} A_{th} &= \begin{bmatrix} \frac{-48\alpha h}{r(24k_{th}+rh)} & \frac{-15\alpha h}{24k_{th}+rh} \\ \frac{-320\alpha h}{r^2(24k_{th}+rh)} & \frac{-120\alpha(4k_{th}+rh)}{r^2(24k_{th}+rh)} \end{bmatrix}, \\ B_{th} &= \begin{bmatrix} \frac{\alpha}{k_{th}V_b} & \frac{48\alpha h}{r(24k_{th}+rh)} \\ 0 & \frac{320\alpha h}{r^2(24k_{th}+rh)} \end{bmatrix}, \\ C_{th} &= \begin{bmatrix} \frac{24k_{th}-3rh}{24k_{th}+rh} & -\frac{120rk_{th}+15r^2h}{8(24k_{th}+rh)} \\ \frac{24k_{th}}{24k_{th}+rh} & \frac{15rk_{th}}{48k_{th}+2rh} \end{bmatrix}, \\ D_{th} &= \begin{bmatrix} 0 & \frac{4rh}{24k_{th}+rh} \\ 0 & \frac{rh}{24k_{th}+rh} \end{bmatrix}, \end{aligned} \tag{5.4}$$

Table 5.1: Thermal model parameters

Parameter	Symbol	Value	Unit
Density	ρ	2047	kg/m^3
Specific heat coeff.	c_p	1109	J/kgK
Thermal conductivity	k_t	0.610	W/mK
Radius	r	12.9×10^{-3}	m
Height	L	65.15×10^{-3}	m
Volume	v_b	3.421×10^{-5}	m^3

where k_{th}, h and ρ are the thermal conductivity, convection coefficient and bulk density, α, the thermal diffusivity is defined as the ratio of k_{th} to the heat capacity, c_p. These parameters are assumed to independent of the cell and ambient temperatures.

The bulk of heat generation in electrochemical cells can be attributed to three components – Joule, entropic and heating due to polarization. Since the current in this application is bidirectional and is large in magnitude, Joule heating dominates entropic heating. Further, the heat generated by polarization is affected by the time constant of the R-C pair and the voltage across them.

$$q = \frac{v_1^2}{R_1} + I^2 R_s \tag{5.5}$$

5.2 Model Parametrization & Validation

The parameters of the thermal model, thermal properties of the cell and the environment, are not significantly influenced by temperature variations. This affords us the option of adopting values presented in [43] (reproduced in Table 5.1) without change. However, a similar argument cannot be made for the electrical model.

Modeling the electrical dynamics of Li-ion cells as a linear parameter varying system has been extensively pursued in literature eg. [41] and references therein. In this chapter, the standard method utilized to parameterize equivalent circuit models and which is described in [41] is extended to sub-zero temperatures.

Figure 5.3 presents some of the key characteristics of the representative sub-model; each line in every subplot corresponds to the trajectory of the variable as a temperature changes for a particular SOC.

Based on the estimated values for model parameters, for large currents, it can be shown that the heat generated can be approximated by Joule heating. Hence in the remainder of the chapter, the generated heat is computed as

$$q = I^2 R_s. \tag{5.6}$$

To validate the models described in the sections afore, a 26650 LFP cell was instrumented with a thermocouple in its center cavity and placed in a Cincinnati Sub-Zero ZPHS16-3.5-SCT/AC temperature controlled chamber. The chamber temperature was set to -20 °C and the air-flow was regulated to mimic natural convection ($h = 5\ W/m^2K$). This cell was excited with square current pulse-train provided by a Bitrode FTV1-200/50/2-60 cycler. Each pulse in current was set to have a duty-cycle of 50% and the magnitude of charging and discharging currents were set at five and 10 amperes. The frequency of pulse-train was set to 1 Hz and measurements of terminal voltage, current, surface and core temperature were collected at the rate of 100 Hz. The measured current was fed to both the electrical (single R-C model) and thermal models and the estimated terminal voltage,

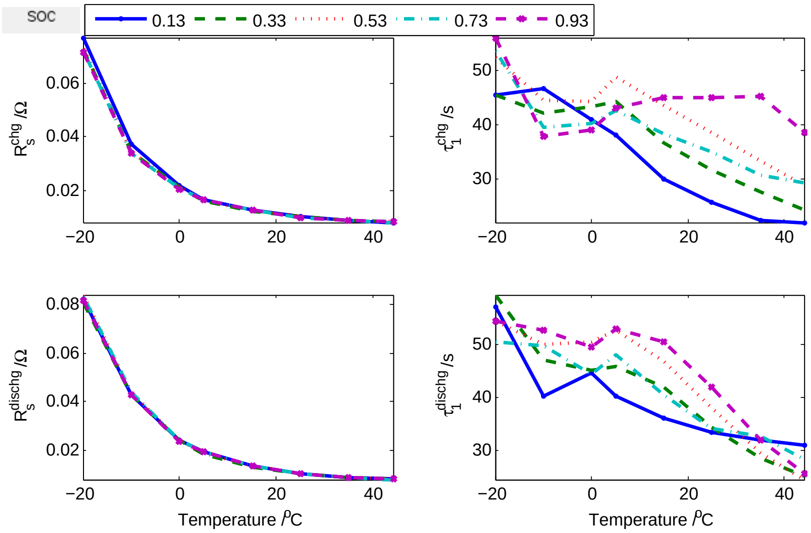

Figure 5.3: Estimated SOC and temperature dependent parameters at different SOCs during charge (*chg*) discharge (*dischg*)

surface and core temperatures are plotted in Figs. 5.4 – 5.5.

From Fig. 5.4 it is noted that the root mean squared (rms) error in estimating the terminal voltage is less than 50 mV. Much of the large errors in estimation of terminal voltage is incident with changes in current direction. The most likely reason is that while the model is able to capture the steady state values, it has deficiencies in capturing the very fast transients. The relatively slower transients are captured by the R-C pair in the model and the first subplot in Figure 5.4 traces the trajectory of the estimated bulk polarization. Observe that the polarization voltage is at-times almost 10% of the total voltage swing across the entire SOC range and can can significantly the measured terminal voltage.

In this work, we are interested in warming the cell. Since most of the heat is generated through Joule heating and given that the parameterized model is able to capture the steady-state voltage fairly accurately, the developed model is assumed adequate and is used in the remainder of the chapter.

Figure 5.5 presents the outcome of simulating the thermal model. The input to the thermal model, namely Joule heating, was computed using the electrical model parameters and states. Upon inspection, it is possible to conclude that the thermal model is able to predict the surface and core temperatures to within the accuracy of the T-junction thermocouples, 0.5°C, for the critical range of cold conditions

5.3 Automated Optimal Warm-Up Formulation

The primary focus of this work is on warming the cell in an energy efficient manner until the desired power can be drawn from the cell. To this end, based on electrochemical

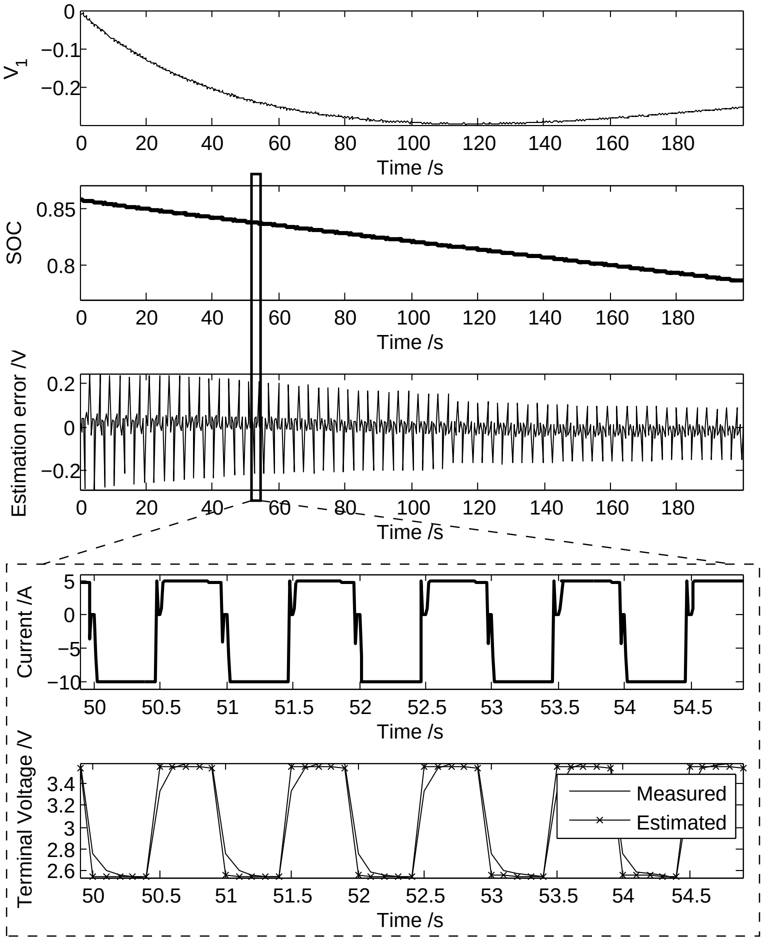

Figure 5.4: Model validation – Predicting Terminal Voltage

considerations, the profile of input current is chosen as a sequence of bi-directional pulses recurring at a certain frequency. To keep the problem formulation simple, each period is stipulated to have just one sign change in current as shown in Figure 5.6. To completely characterize the current profile, one would require four control variables – frequency, duty-cycle, peaks of charge and discharge pulses. The frequency of the pulse train influences the rate of heat generation – from EIS tests, increasing frequencies decreases the effective series resistance while decreasing the reactive component of the total impedance [103]. In this study, the optimal frequency at which the resistance is *large* yet the reactive component is *small* is assumed to be known. Since the frequency is pre-determined, the values of the remaining variables – duty-cycle and magnitudes, need to be determined.

The dynamic behavior of the electrical and thermal sub-systems of the cell are functions of its operating conditions and internal states. Specifically, the optimal decision at the kth instance is influenced by the trajectory of states until then. As the model dynamics is affected by the value of its states, the problem of deciding the values of the control variables

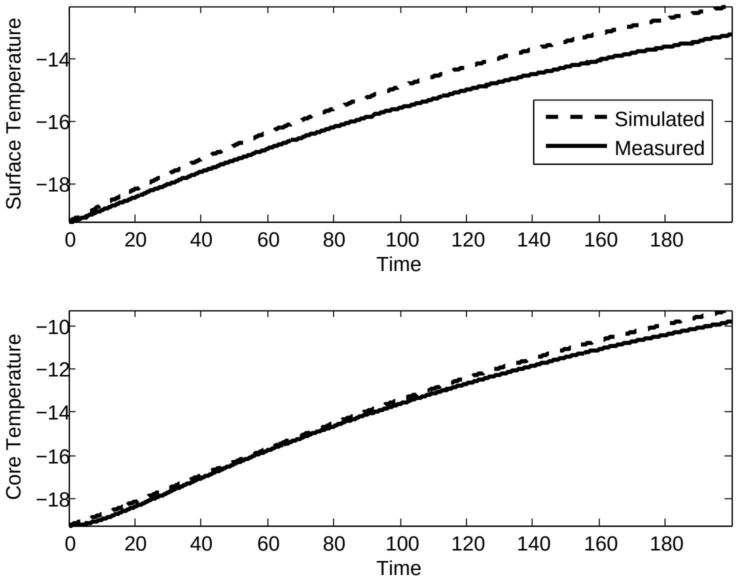

Figure 5.5: Model Validation – Predicting Surface and Core temperatures

is formulated as a linearized receding finite horizon optimization problem and described in this section.

The objective of the problem under consideration is to increase the temperature of the cell while penalizing the effective energy discharged (measured in terms of loss in SOC) from the cell. This objective can, in the general case, be mathematically formulated as

$$\min_{\mathcal{U},\mathcal{D}} -[\bar{T}_{k+1+n_s\cdot N} - \bar{T}_{k+1}] + \tilde{\beta}\sum_{j=1}^{N}(u_{c,j}\cdot d_{c,j} + u_{d,j}\cdot d_{d,j}), \tag{5.7}$$

where N is the number of periods in prediction horizon, $\tilde{\beta}$ is the relative penalty on energy loss, n_s is the number of samples per period of the pulse; in the j^{th} period of the horizon,

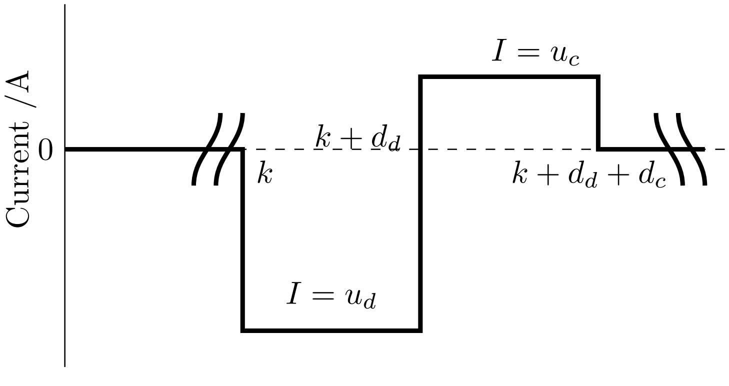

Figure 5.6: Pulse current profile

$d_{c,j}$ and $d_{d,j}$ are the durations of charge and discharge portion of the period as multiples of sampling period ΔT, and $u_{c,j}$ and $u_{d,j}$ are the the charge and discharge currents. Then,

$$\begin{aligned}
\mathcal{D} &= \Big\{\{d_{c,j},\, d_{d,j}\} \mid \forall j \in [1, N] \cap \mathbb{Z},\, d_{c,j} + d_{d,j} \leq n_s\Big\},\\
\mathcal{U} &= \Big\{\{u_{c,j},\, u_{d,j}\} \mid \forall j \in [1, N] \cap \mathbb{Z},\, |u_{c,j}| \leq |u_{d,j}|\Big\}.
\end{aligned}$$

Note that Eqn. (5.7) is, by virtue of the fact that the second term is non-convex and that the first and second terms do not have terms in common, non-convex. The variables over which the problem is optimized takes a mixture of integer and continuous values; the problem under consideration is a non-convex Mixed Nonlinear Integer Programming problem (MNIP). Non-convex MNIPs are NP-hard [104] and are not suitable for online control. In the interest of making the problem more tractable, in this chapter, the duty-cycle of both charge and discharge pulses are set to be equal; i.e. 50% duty-cycle; in so doing, the problem devolves into a regular nonlinear programming problem (NLP) that could be solved online.

Having fixed the duty-cycle to be 50%, for simplicity of expressions, without loss of generality it is assumed that each period of the current is spread over only two samples. A more general case is easily derived by scaling the appropriate variables.

5.3.1 Characterizing the current profile

At each instant l, for a prediction horizon of length $2N$ samples, the problem of deciding the magnitude of pulses to increase cell temperature in an energy conscious manner is computed by solving the following problem **P1**:

$$\min_{u} \; -[\bar{T}_{l+2N+1} - \bar{T}_{l+1}] + \tilde{\beta}|z_{l+2N+1} - z_{l+1}|$$

$$\text{s.t. : } \forall k \in \{l+0, \ldots, l+2N\}$$

$$\left.\begin{aligned}
x_{th,k+1} &= A^d_{th} x_{th,k} + B^d_{th} v_{th,k}\\
y_{th,k} &= C^d_{th} x_k + D^d_{th} v_{th,k}\\
v_{th,k} &= [u_k^2 R_{s,k}; T_{amb,k}]
\end{aligned}\right\} \tag{5.8a}$$

$$\left.\begin{aligned}
x_{el,k+1} &= A^d_{el} x_{el,k} + B^d_{el} u_k\\
y_{el,k} &= C^d_{el} x_{el,k} + D^d_{el} u_k + G^d_{el}
\end{aligned}\right\} \tag{5.8b}$$

$$\left.\begin{aligned}
&|u_i| \leq |I_d(\bar{T}_i)|,\ \forall i \in \{l+1, l+3, \ldots, l+2N-1\}\\
&|u_i| \leq |I_c(\bar{T}_i)|,\ \forall i \in \{l+2, l+4, \ldots, l+2N\}\\
&|u_i| \geq |u_{i+1}|,\ \forall i \in \{l+1, l+3, \ldots, l+2N-1\}
\end{aligned}\right\} \tag{5.8c}$$

$$\left.\begin{aligned}
v_{t,i} &\leq v_{max},\ \forall i \in \{l+1, \ldots, l+2N\}\\
-v_{t,i} &\leq -v_{min},\ \forall i \in \{l+1, \ldots, l+2N\}
\end{aligned}\right\} \tag{5.8d}$$

$$x_{el,k} = x_{el,l},\ x_{th,k} = x_{th,l}$$

where $z_k = x_{el,k}(1)$, $\bar{T}_k = x_{th,k}(1)$, $G_{el}^d = v_{oc}(z_{k-1})C_{el}^d(1)z_{k-1}$, $u = [u_1, \ldots, u_{2N}]'$, and $\tilde{\beta}$ is a relative weight that penalizes changes in SOC. In the above, the vector of control variables, u, is arranged such that odd and even elements correspond to discharging and charging current magnitudes respectively.

The cost function of **P1** strikes a compromise between total increase in the cell's average temperature and penalized loss in state of charge over the entire prediction horizon. Eqns. (5.8a) and (5.8b) describe the equality constraints on the temperature and electrical model dynamics in which a superscript 'd' indicates the discrete version of the variable. Cell manufacturers typically specify the voltage operating limit $[v_{min}, v_{max}]$, and the maximum charge and discharge current limits as a function of temperature; Eqns. (5.8c) and (5.8d) enforce these constraints.

For ease of implementation, the optimal control problem in Eqn. (5.8) is re-written as an optimization problem by recursive substitution of the dynamics as follows. Expressing the thermal dynamics, in discrete-time as

$$x_{th,k+1} = A_{th}^d x_{th,k} + B_{th}^d \begin{bmatrix} q_k \\ T_{amb,k} \end{bmatrix},$$

with $q_k = u_k^2 R_s$, it can be seen that,

$$\begin{aligned} & x_{th,k+2N+1} - x_{th,k+1} = \\ & [(A_{th}^d)^{2N} - \mathbb{I}_n]x_{th,k+1} + \sum_{j=1}^{2N} (A_{th}^d)^{j-1} B_{th}^d \begin{bmatrix} R_s u_p^2 \\ T_{amb,p} \end{bmatrix} \end{aligned}$$

where $p = 2N - j + k + 1$.

Then,

$$\begin{aligned} \bar{T}_{k+2N+1} - \bar{T}_{k+1} &= \underbrace{\begin{bmatrix} 1 & 0 \end{bmatrix}}_{\tilde{C}} [x_{th,k+2N+1} - x_{th,k+1}], \\ &= \tilde{C}[(A_{th}^d)^{2N} - I]x_{th,k} + \tilde{C} \sum_{j=1}^{2N} (A_{th}^d)^{j-1} B_{th}^d \begin{bmatrix} R_s u_p^2 \\ T_{amb,p} \end{bmatrix}, \\ &= u'Wu + \text{const.}, \end{aligned} \tag{5.9}$$

where, defining $\vartheta_j := \tilde{C}(A_{th}^d)^{2N+k-j} B_{th}^d \tilde{C}' R_s$, $W = diag([\vartheta_1, \ldots, \vartheta_{2N}])$. The constant term in Eqn. (5.9) can be expressed as $\tilde{C}[(A_{th}^d)^{2N} - I]x_{th,k} + \bar{C} \sum_{j=1}^{2N} (A_{th}^d)^{j-1} B_{th}^d \bar{C} T_{amb,2N-j+k+1}$ where $\bar{C} = [0\ 1]$. As constant terms in the cost are immaterial to minimization problems, the above constant is dropped in the following expressions.

Since the evolution of SOC is related to the summation of the control variables, the original problem in Eqn. (5.8) can be re-written in the following form

$$\begin{aligned} \min_{u} \; & -\|u\|_W^2 + \beta \sum_j u_j \\ \text{subject to : } \; & \Psi u \leq \Upsilon \\ & |u_i| \leq |I_d(\bar{T})|, \; \forall i \in \{1, 3, \ldots, 2N-1\} \\ & |u_i| \leq |I_c(\bar{T})|, \; \forall i \in \{2, 4, \ldots, 2N\} \\ & |u_i| \geq |u_{i+1}|, \; \forall i \in \{1, 3, \ldots, 2N-1\} \end{aligned} \tag{5.10}$$

where Ψ and Υ are as defined in Eqn. (5.11).

$$\Psi = \begin{bmatrix} -D^d_{el} & 0 & 0 & \cdots & 0 \\ C^d_{el}B^d_{el} & D^d_{el} & 0 & \cdots & 0 \\ -C^d_{el}A^d_{el}B^d_{el} & -C^d_{el}B^d_{el} & -D^d_{el} & \cdots & 0 \\ \vdots & \vdots & \vdots & \ddots & \vdots \\ C^d_{el}(A^d_{el})^{(2N-2)}B^d_{el} & C^d_{el}(A^d_{el})^{(2N-3)}B^d_{el} & C^d_{el}(A^d_{el})^{(2N-4)}B^d_{el} & \cdots & D^d_{el} \end{bmatrix} \tag{5.11a}$$

$$\Upsilon = \begin{bmatrix} -v_{min} \\ v_{max} \\ -v_{min} \\ \vdots \\ V_{max} \end{bmatrix} - \begin{bmatrix} -C^d_{el}A^d_{el} \\ C^d_{el}(A^d_{el})^2 \\ -C^d_{el}(A^d_{el})^3 \\ \vdots \\ C^d_{el}(A^d_{el})^{2N} \end{bmatrix} x_k - \begin{bmatrix} -C^d_{el}B^d_{el} \\ C^d A^d B^d_{el} \\ -C^d_{el}(A^d_{el})^2 B^d_{el} \\ \vdots \\ C^d_{el}(A^d_{el})^{2N-1}B^d_{el} \end{bmatrix} u_k - \begin{bmatrix} -(v_{oc}(z_k) - C^d_{el}(1)z_k) \\ v_{oc}(z_k) - C^d_{el}(1)z_k \\ -(v_{oc}(z_k) - C^d_{el}(1)z_k) \\ \vdots \\ v_{oc}(z_k) - C^d_{el}(1)z_k \end{bmatrix} \tag{5.11b}$$

$$W = diag([\vartheta_1, \ldots, \vartheta_{2N}]), \; \vartheta_i > 0, \; \vartheta_i \text{ are functions of thermal system matrices.} \tag{5.11c}$$

The above optimization problem belongs to the class of problems where a concave function is minimized over a convex set; such problems have been studied extensively in literature. Solvers of concave optimization problems can be broadly classified as being either approximate or global; global methods generally employ cutting-plane and or branch and bound techniques [105, 106]. In general global solvers are computationally expensive and thus their use may be limited to small-scale problems.

To gain better insight into the nature of the optimization problem under investigation, consider the simple case when the prediction horizon is of length one. Figure 5.7 presents the characteristic shape of the constraint polytope in $\mathbb{R}^2$ wherein coordinates of the vertices represent, in sequence, the magnitude of discharge and charge pulses. While edge e_1 enforces the trivial condition that charging and discharging pulses cannot have the same polarity, edge e_2 ensures that the magnitude of the charge current is never greater than that of the discharge current. Edges e_3 and e_4 complete the polytope and enforce adherence to voltage and current constraints.

The bounded polytope defined by constraints in the problem under consideration is convex. The solution to concave minimization problems, when restricted to a convex polytope

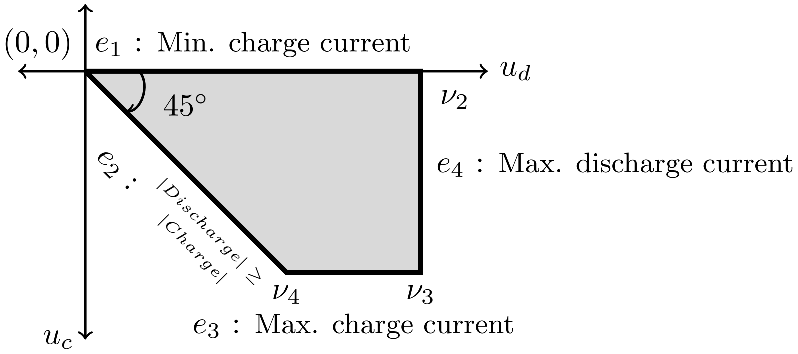

Figure 5.7: Region of the constrained optimization problem when the prediction length is one.

Algorithm 3: Control Algorithm (open-loop)

```
set flag=0;
set $[u_d, u_c]' = [-1, 1]'$;
set number_of_samples_in_block;
while !flag do
    Compute $P_{cap}$;
    if $P_{cap} <= P_{dmd}$ then
        Solve optimization problem;
        set $[u_d, u_c]' = [-u_d^*, u_c^*]'$;
        wait($t_s \cdot$ number_of_samples_in_block) seconds
    else
        set flag=1;
    end
end
† Variables with an '*' superscript are optimal solutions.
```

lies, at one of the vertices of the polytope [107]. For the simple case depicted in Fig. 5.7, it can be shown that the solution lies at either ν_3 or ν_4. As this work is a feasibility study in a simulation framework, the concave minimization problem is solved using a vertex enumeration strategy to find the global minimizer.

5.3.2 Control scheme

In the preceding sub-section, the problem of determining the magnitude of input current of the cell was formulated as an optimization problem in a receding horizon framework. Incorporating the termination condition based on power capability, the overall process can be cast into the control scheme depicted in Alg. 3.

The time constant of the thermal dynamics of the cell under consideration is in the order of tens of minutes. Thus, the increase in temperature as a result of applying one period of current (at 10Hz) may not be significant. For this reason the problem of current magnitude

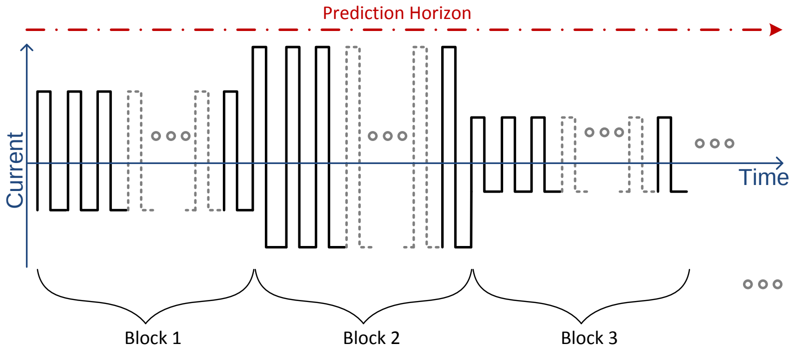

Figure 5.8: Blockwise implementation of the MPC problem

determination is solved in blocks. Periods in the prediction horizon are binned into blocks, with each block consisting of a pre-set number of pulse periods; the prediction horizon is then described by the number of blocks (refer Fig. 5.8). The optimization problem as formulated earlier is modified to enforce the constraint that every period in each block is identical.

In the overall scheme, at each control instant, the power capability, P_{cap}, is first estimated and compared to the desired set-point, P_{dmd}. If the required power cannot be provided, the optimization problem to compute the magnitudes of the pulses is solved and the optimal solution to the first block is applied. After waiting a duration that is equal to the duration of the block, the process is repeated and the power capability is re-computed. Once the desired power can be delivered, the warm-up operation is terminated.

Remark : Operation of this kind can be interpreted as intentionally allowing the states of the thermal model to grow. The thermal dynamics of a Li-ion cell is inherently stable, unless the temperature is increased to levels that may trigger thermal run-away. It can be argued that given the coupling between the thermal and electrical sub-models, as long as the maximum temperature is bounded away from (from above) a critical temperature ($\approx 80°C$), the thermal model remains stable and controllable. As for the electrical dynamics, SOC is a constrained state and the value of V_1 is implicitly bounded as a function of constraints on the terminal voltage and input current.

5.4 Simulation and Discussion

In this section, the proposed Pulsed Current Method (PCM) is simulated with both the plant and model dynamics dictated by the equations in Section 5.1.

5.4.1 Simulation setup

The augmented electro-thermal model (Eqn. (5.13)) is nonlinear in input and output; the proposed algorithm is implemented using discrete local linear models and is simulated

Table 5.2: Manufacturers specifications for A123 26650 cells for constant operation.

Direction	Temperature	Continuous Current
Charge	0–20^{o}C	3A
Charge	20–50^{o}C	10A
Discharge	-30–60^{o}C	60A

in the MATLAB/Simulink environment using a custom vertex enumerator.

$$\begin{bmatrix} \dot{x}_{el} \\ \dot{x}_{th} \end{bmatrix} = \begin{bmatrix} A_{el}x_{el} \\ A_{th}x_{th} \end{bmatrix} + \begin{bmatrix} B_{el} & 0 \\ 0 & B_{th} \end{bmatrix} \begin{bmatrix} u \\ u^2 \\ T_{amb} \end{bmatrix}$$

$$V_t = V_{OCV}(x_{el}) + C_{el}x_{el} + D_{el}u, \tag{5.13}$$

where u is the current drawn from the cell.

In implementing PCM variable values were chosen as follows – the cell operating voltage bounds were set at $[2, 3.6]$; the frequency of the pulse train was set to 10Hz based on electrochemical considerations [39] and the model was simulated at Nyquist frequency. The energy that is removed from the cell is assumed to be stored in an external storage system such as an ultracapacitor bank.

The simulated LFP cell is assumed to be a part of a pack that consists of 60 cells in series and four cells in parallel with a rated nominal continuous power at 25°C of 45 kW. Limits on the maximum deliverable current were set by factoring in manufacturers specifications (Table 5.2) and the standards proposed by USABC [108]. Note that the specifications provided in Table 5.2 are for continuous discharge. For pulsed currents, a multiplicative factor of 1.5 is used to amplify the current ratings for constant operation. The value of charge current limit below freezing was not provided explicitly in specification sheets. In practice, this limit may have to be empirically estimated if it is not provided. The value of the limit can be taken at the maximum magnitude of current that does not increase the effective resistance of the cell after a pre-determined number of energy cycles (using pulsed currents). In this study this limit is set at 1C. In addition, we assume a Arrhenius relation for the increase in charge current limit above 0°C.

The control scheme proposed in Section 5.3 relies on a receding horizon controller. In receding horizon controllers, the length of the prediction horizon is a tuning parameter that takes integer values. However, for large problems and problem with fast dynamics, shorter control and prediction horizons are preferred; in [109], the authors provide necessary conditions for when the prediction horizon of length one is near optimal. In this section, unless stated otherwise, it assumed that the prediction and control lengths are of length one; the impact of this assumption is studied numerically in Section 5.4.4.

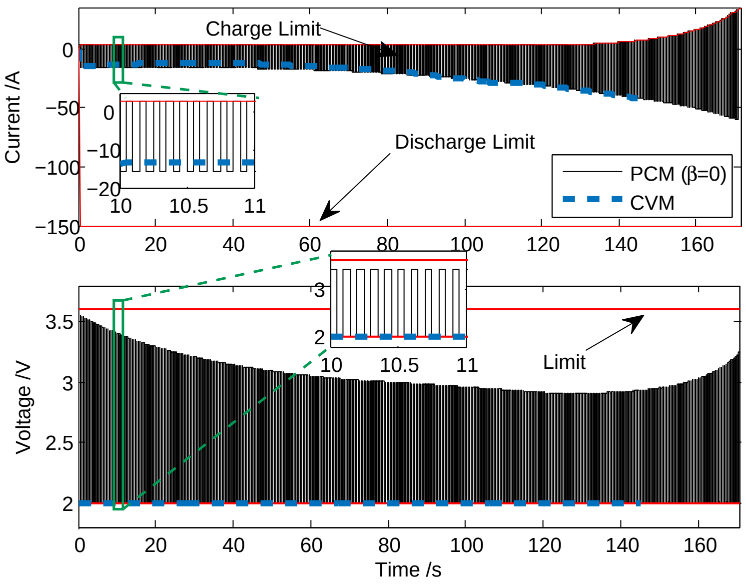

Figure 5.9: Down-sampled simulated trajectory of (down-sampled by 19) voltage and current using Pulse Current Method ($\beta = 0$)

5.4.2 Simulation, results & discussion

This section documents result of simulating the electro-thermal model of the battery developed in Sections 5.1 and 5.2 using the algorithm described in Section 5.3. Simulations are run with the following parameters – $SOC_0 = 0.6$, ambient temperature set to -20^oC and under natural cooling condition ($h = 5\,W/m^2K$).

5.4.3 Baseline

To study the performance of the proposed method and to establish a baseline, we compare the trajectories of battery temperature, power capability and SOC from the following two cases:

1. the limiting case when $\beta = 0$
2. the case of maximum permissable continuous discharge.

The second case, when the maximum permissable continuous discharging current is drawn, generates the maximum possible heat at every sample and hence is an approximate solution to the minimum warm-up time problem. In this mode of operation, to satisfy constraints, the terminal voltage is held at V_{min} (that is as long as the discharge current constraint is satisfied); thus, this mode is labeled Constant Voltage Method (CVM).

Figures 5.9 and 5.10 present trajectories resulting from simulating the electro-thermal model using the proposed reference current generation algorithm, PCM, and CVM using

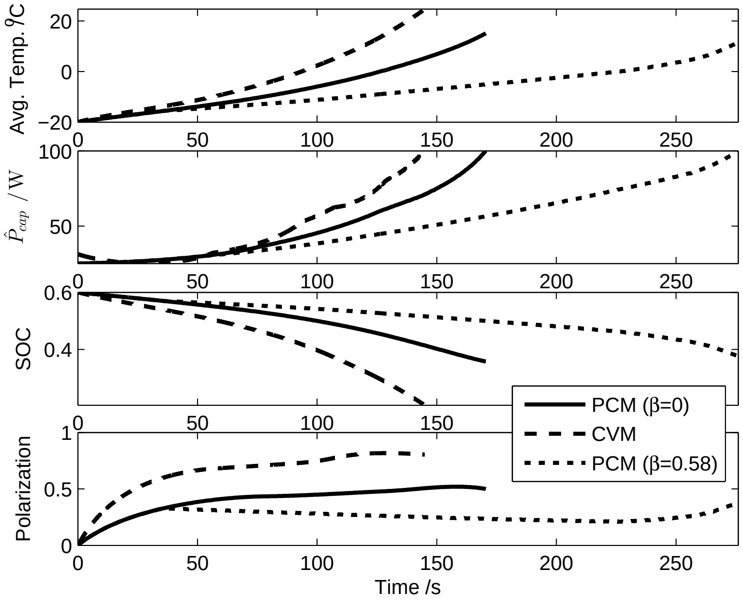

Figure 5.10: Simulated trajectories of average temperature, power capability and polarization using Pulse Current Method (PCM) and Constant Voltage (CVM) Method. The simulation was performed with the pack initialized with $SOC_0 = 0.6$ operating from −20°C with a terminal power demand, $P_{dmd} = 100$W under natural cooling conditions ($h = 5\ W/m^2K$).

power demand, ($P_{dmd} = 100$ W) as terminal constraint. Table 5.3 tabulates some of the key indices from having applied CVM and PCM.

The value of penalty on SOC lost in each period, β, influences the duration of the warm-up operation. Larger penalties will tend to increase the duration of the warm-up phase; this follows by observing that when operating from sub-zero temperatures, the current limits are not symmetric. That is, the minimum warm-up time that can be achieved using PCM is when $\beta = 0$. From Fig. 5.9 and Table 5.3, it is noted that the warm-up time when using CVM is shorter than when using PCM with $\beta = 0$. Thus, the warm-up time using PCM, for any value of β, will be longer than when using CVM.

Energy storage elements such as ultra-capacitors do not have very high energy densities, i.e., it is desirable to transfer as little energy as possible to the external energy storage element. From Table 5.3, note that the equivalent SOC stored in external storage using

Table 5.3: Comparison between PCM* and CVM, key indices

Method	Oper. Time	SOC_{store}	$\bar{T}_{final}$	SOC_{loss}
PCM ($\beta = 0$)	172s	0.13	17.5^{o}C	0.11
PCM ($\beta = 0.58$)	278s	0.12	12.25^{o}C	0.10
CVM	143s	0.23	24.3^{o}C	0.15

*1 block with 5 periods

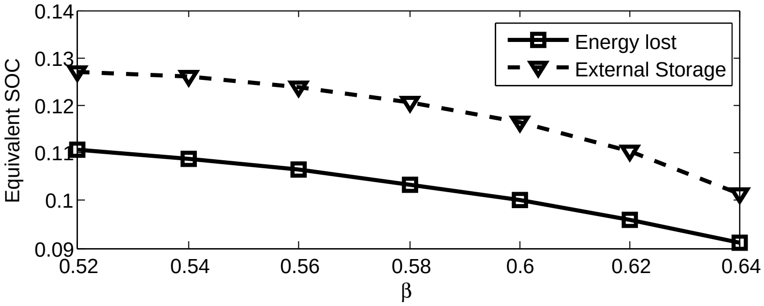

Figure 5.11: Results on increasing penalty on energy loss as percent of when no penalty is applied. The simulation was performed with the pack initialized with $SOC_0 = 0.6$ operating from −20°C with a terminal power demand, $P_{dmd} = 100$ W under natural cooling conditions ($h = 5\ W/m^2K$).

CVM is almost twice that of PCM.

Lastly, in comparing the effective energy lost using both methods — PCM and CVM — it is noted that CVM is more lossy. More specifically, comparing the CVM with PCM ($\beta = 0$), we observe that the total energy lost increases by nearly 35%; this increased loss manifests itself as increased terminal temperature of the cell.

The above results bear evidence to the fact that terminating warm-up based on terminal temperature is not the same as when using power as terminal constraint. While CVM enjoys shorter operating times, it is more lossy and requires larger storage elements as compared to PCM.

5.4.3.1 Penalizing energy loss

As formulated, the value of penalty β in the cost can be used to regulate the amount of energy dissipated as heat. Figure 5.11 documents the total energy lost and the reduction in size of external storage elements in equivalent battery SOC, for different values of β. Inspecting Fig. 5.11, it it evident that increasing the value of β can reduce energy expenditure and external sizing. By computing the percent change with respect to when $\beta = 0$, the energy lost and external storage size can be reduced by as much as 20%. This increased efficiency of operation does however come at the expense of operation time. Figure 5.12 presents a comparison between the increase in warm-up efficiency and time taken to be able to deliver the desired power; increased energy efficiencies result in increasing warm-up times.

The observations from Figs. 5.11 and 5.12 can be explained by studying the trajectories of terminal and polarization voltages, when $\beta = 0$ and $\beta = 0.58$; Figs. 5.10 and 5.13 depict these trajectories. The first observation from comparing these figures is that unlike the case when $\beta = 0$, the trajectory of terminal voltage when $\beta = 0.58$, does not always hit the lower limit of 2V; however, it does on occasion. Further, the trajectory of polarization is different after 40 s; these observations can be interpreted as follows.

From the problem formulation in Eqn. (5.10), it is possible to show that the value of polarization and the cell's operating temperature result in the solution migrating between vertices of the constraint polytope (as an example cf. Fig. 5.7 and vertices ν_3 and ν_4). The vertices between which the solution switches are dictated by the temperature of the cell, penalty β and the polarization. As the penalty, β, increases, SOC lost over the control horizon becomes important; therefore, the optimal solution tends to be $u_d = u_c$, i.e. the amplitudes of current during charge and discharge are the same, which can be clearly observed in Fig. 11 when $\beta = 0.58$ compared to the case of $\beta = 0$ in Fig. 9. The preference of charging and discharging at the same current rate has to consequences:

1. the average current during the control horizon decreases to zero and hence polarization voltage drops as well.
2. the heat generated during each period reduces and correspondingly the increasing rate of temperature diminishes.

As seen from Fig. 8, the increasing rate of temperature becomes lower when $\beta = 0.58$ than when no penalty on SOC loss is imposed. It is also observed that polarization voltage decreases from 50 second to 230 second. The polarization state is inherently stable; as the average current during each block in the control horizon tends to zero, the value of polarization decreases. The reduced polarization and rate of heat generation may result in the solution switching back to the vertex that extracts maximum current from the cell (vertex ν_3 in Fig. 5.7). This results in the switching behavior observed in Fig. 5.13.

Figure 5.12 also highlights another important characteristic of the solution – as the value of β is increased, the operation time reaches an asymptote, i.e. it becomes impossible to reach the desired terminal power capability. This is an extension of the behavior described above wherein the solution migrates; as β increases, the solution migrates and remains at the vertex that favors charging and discharging currents being of the same magnitude (vertex ν_4 in Fig. 5.7). In addition, for βs sufficiently large, the solution will remain at the vertex that favours negligible SOC loss and hence the power demand can never be achieved. Thus, for the above algorithm to be implemented, the value of β needs to be chosen appropriately to ensure feasibility of the overall problem.

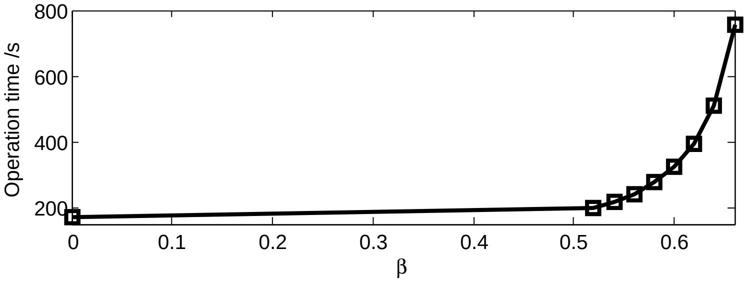

Figure 5.12: Comparison between increased efficiency and warm-up operation time

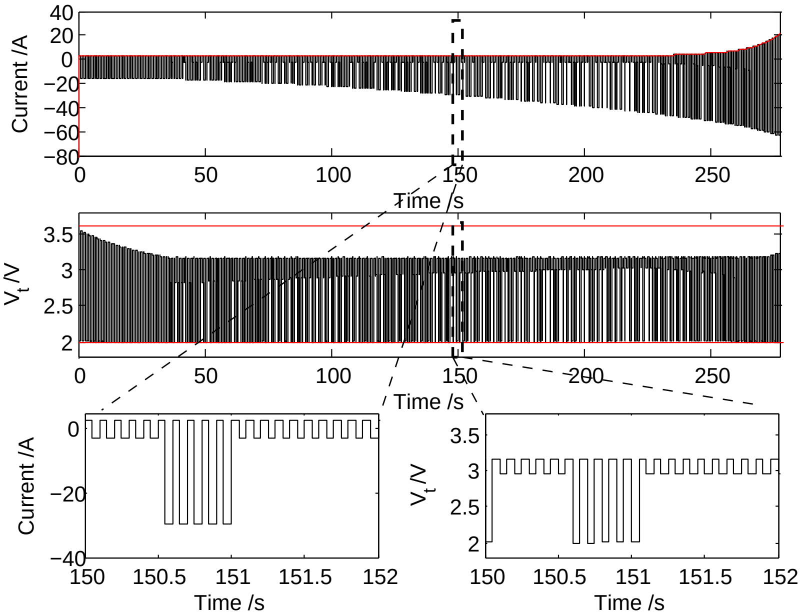

Figure 5.13: Simulated trajectory of voltage, polarization and current using Pulse Current Method, $\beta = 0.58$. The simulation was performed with the pack initialized with $SOC_0 = 0.6$ operating from −20°C with a terminal power demand, $P_{dmd} = 100$W under natural cooling conditions ($h = 5\ W/m^2K$).

Table 5.4: Impact of prediction horizon based on key indices*

Prediction Length Index	1	2	3
SOC_{loss}	1	0.99	0.98
External Storage	1	0.99	0.97
Terminal Time	1	1.01	1.03
Computational Time	1	35	107

* Entries normalized wrt. results when prediction length is one block

5.4.4 Effect of longer prediction horizons

In simulating the results presented thus far, the prediction horizon was set to be a single block consisting of five pulses. In the context of predictive control, longer prediction horizons are known to produce better approximations of the global optimal solution. In this application, owing to the linearized MPC implementation, the prediction horizon cannot be taken to be arbitrarily large without incurring errors resulting from model linearization.

To investigate the influence of prediction horizon on the optimal solution trajectory, an iterative test was performed[1] wherein the length of the prediction horizon was increased incrementally; results of which are presented in Table 5.4. The other parameters of the simulation were : $P_{dmd} = 50W$, $h = 5W/m^2K$ and $\beta = 0.57$ (the power demand is set at 50

---

[1] Simulations were performed on a computer powered by an Intel i5-2500 quad-core processor with 16GB of ram and running Windows 7 with parallelization enabled.

W in the interest of computational time).

The data presented in Table 5.4, as expected, indicates that given the same penalty on loss in energy, increasing the length of the prediction horizon decreases the total energy lost; this however does come at the expense of computational time. In fact, there appears to be a quadratic relation between decrease in loss and total operation-time. Comparing the effective increase in savings and the increase in computational and operation time, a case for the use of prediction horizon of length one block can be made.

5.5 Conclusion

In this work, a Li-ion battery warm-up strategy that increases the cell temperature to meet power demand in an energy efficient method is described. The shape of current used to shuttle energy between the cell and an external energy storage system was set to be bi-directional pulses to minimize polarization and reduce damage to electrodes. Magnitude of the pulses were determined by solving a constrained optimization problem. From simulations based on models of a 26650 LFP cell, it is noted that it is possible to reduce energy lost as heat and the size of external storage, by as much as 10% when compared against using just constant voltage discharge. There is however, a compromise to be made between reduction in size of storage, energy lost and time taken to warm-up.

CHAPTER VI

Concluding Remarks

6.1 Summary of Contributions

This dissertation is concerned with the *energy-conscious* control of battery warm-up from sub-zero temperatures and is of critical importance to the growing fleets of electrified vehicles that traverse a variety of terrains in cold weather conditions.

First, a warm-up method is developed as a solution of an energy-optimal warm-up problem that aims to increase the battery's temperature until it reaches a desired temperature set-point, whilst powering an assisting external heater. This solution is shown to resemble a sequence of constant voltage, constant current and rest phases. In addition, approximate feedback laws for warm-up are synthesized by using novel tools to address reachability problems. Using an approximate solution, it is noted that in temperature terminated problems, the impact of the rest condition can be as much as 8%. In addition, the notion of *productive warm-up* is introduced as the warm-up operation that would ensure that the battery is capable of performing work upon warm-up. The task of identifying the set of initial battery states from which *productive warm-up* is feasible is undertaken by interpreting it as a reachability verification problem.

Secondly, it is suggested that the power capability of the battery can be considered as a possible means to specify terminating conditions for battery warm-up. A model of the electro-thermal dynamics of the battery at sub-zero temperatures is characterized and is utilized to design two battery warm-up strategies. The first strategy draws bi-directional currents to effect an increase in the battery's temperature until the battery is able to deliver the desired power. This strategy assumes the presence of an external energy storage element such an ultracapacitor which can serve as a temporary reserve.

Since the two warm-up strategies devised use terminating conditions that are specified differently – (former) power capability set-point, (latter) temperature set-point; the question of whether one formulation is better than the other is answered. It is shown that under certain assumptions on the dynamics of the system, the two formulations are equivalent. However, more generally, specifying the terminating constraint in terms of power capability is seen to be more sensitive to uncertainties in the parameters of the system.

It should be noted that the baseline in the discussions on pulsed current method—constant voltage method—is a particular specialization of the optimal solution to the warm-up problem discussed in Chapter II. It is seen that the pulsed current method can be about 10% more efficient than the uni-directional current that is the solution to the problem in Chapter II. However, the cost of ultracapacitor banks needed to eke out the improvements in performance may serve as an inhibiting factor.

Finally, to help reduce the uncertainty in the model parameters, an estimator is designed. To do so, a novel method to partition the augmented state-space consisting of states and parameters to be estimated is proposed. This partitioning technique differs from standard *dual filters* in that the partitioning is based on the averaged local observability of all elements in the augmented state-space. The performance of the partitioning technique is demonstrated by designing a cascading sequence of Extended Kalman Filters that estimate the states and parameters of the coupled electro-thermal model of a battery in a HEV.

6.2 Future Directions

This dissertation explored the prospect of energy-efficient warm-up of Li-ion batteries using a reduced order electro-thermal model. The resulting optimal solution using this model was noted and shown, in some cases, to be similar to the obvious strategy. This deduction presents the following directions for future research.

6.2.1 A more physics based approach

In this dissertation, it was noted that the polarization voltage plays an important role in determining the power capability, and the battery's ability to self-warm to meet specifications after the circuit has been opened. Given that the polarization term in the equivalent circuit model is a representation of the cumulative impact of all local polarizations, it is would be interesting to undertake a study that aims to derive energy-optimal rules for warm-up when using a Single Particle Model (SPM). In this case, the manufacturer's constraints do not have to necessarily be adhered to; instead constraints on over-potential can be directly imposed.

The use of a SPM will present yet another research direction: parameterization and state estimation at sub-zero temperatures of the SPM.

6.2.2 Stochastically planned warm-up

In this dissertation, the only problem that was considered was of battery pre-warm-up. That is, suppose the ambient temperature was T_∞ °C and the desired power capability was P_{des}; we sought a policy that can drive the battery's states with $T_c(0) = T_\infty$ and no built-up initial polarization. Let the energy consumed to achieve warm-up be z^*.

Now, consider the instance when $T_c(0) = \bar{T} > T_\infty$ and the initial internal polarization was close to zero. In this case, arguably, the energy required to drive the power capability to P_{des} is less than z^*. Such a situation can arise when the battery temperature is constantly maintained around $\bar{T}$ using some control strategy, say thermostatically.

However, maintaining the battery temperature at $\bar{T} > T_\infty$ is a drain on the batteries' stored energy. If it was known that at sometime in the near future a request for warm-up was to arrive, then it might be worthwhile to maintain the temperature above the ambient. The question then is, given a distribution of possible arrival times of the next warm-up command, if one such exists, what is the optimal value of $\bar{T}$?; and how does this change as a function of time? Can such a planned warm-up be more energy efficient than the case of complete warm-up (beginning warm-up only after a command has arrived) considered in this dissertation?

6.2.3 Warm-up of a pack of self-heating batteries

In [2], the authors present a novel Li-ion battery that has a built in metal foil that serves as a low-resistance load. To warm the battery, a switch is closed that completes the circuit around this small load. The design of the resistance of this foil can be undertaken based on models of the dynamics of the cell.

Now, consider a pack of such cells, with cells connected in series and in parallel. How many of these batteries should be warmed-up to warm the entire pack (in an effort to conserve energy)? Where would these batteries be located in the pack in relation to the pack geometry? Answer to these questions will enable the design of smaller, more efficient battery packs, and better control algorithms.

Appendices

Appendix A

Appendix to Chapter II

1.1 Proofs

Proof of Theorem II.3. To assist in providing a proof, we need the following result about a feature of the optimal solution:

Lemma A.1. *The co-state trajectory associated with the optimal trajectory of T_c is positive almost everywhere in time.*

Proof. This proof follows by directly applying standard results in optimal control relating to the sensitivity interpretation of co-states.

Stated simply, if the value function of (OCP) is V, and if it were differentiable,

$$\psi_3 = -\frac{\partial V}{\partial T_c}. \tag{1.1}$$

Now, recall that the V is the cost-to-go; i.e. it is the smallest amount of SOC that will be required to reach $T_c = T_{des}$. With all other states remaining constant, increasing the battery's temperature decreases the cost-to-go. Hence $\partial V / \partial T_c$ is negative, and ψ_3 is positive.

In the event that V is not differentiable, one can use subgradients to establish similar results [110] [111]. □

By the definition of SOC, it follows that the objective function of (OCP) is equivalent to the following by the Fundamental Theorem of Calculus:

$$J = \frac{1}{3600 \cdot Q} \int_{t_0}^{t_f} I(\tau)\, d\tau. \tag{1.2}$$

Since the associated incremental cost is linear and the dynamics is quadratic in control, it follows that singular arcs do not exist.

We prove this proposition by showing that the Hamiltonian of the optimal control problem is convex in control. Then, by virtue of the fact that the control is constrained to a convex set, it follows that the optimal solution at each instant is an extreme value of the admissible set. To establish the first statement, we relax the air temperature dynamics in the following manner

$$\dot{T}_a = \gamma_1 \cdot (T_c - T_a) + \gamma_2 \cdot (w(t) - T_a) - \gamma_3 \cdot (T_\infty - T_a), \tag{1.3}$$

where $w(t)$ is an exogenous input to the system; this relaxation allows us to consider all possible admissible heater temperature trajectories. Note that when $w(t) = T_h(t)$ a.e, the dynamics reverts back to the original description. Next, observe that the with this re-written T_a dynamics, the heater's temperature as a state does not affect the optimal control problem; it is dropped from further consideration in the optimal control problem[1].

The Hamiltonian of (OCP), with the reduced set of equations, H_T, is of the following form:

$$H_T = \sum_{i=1}^{4} \psi_i f_i(x) + \sum_{i=1}^{4} \psi_i g_i(x) I + \sum_{i=1}^{4} \psi_i h_i(x) I^2 \tag{1.4}$$

where ψ_i are co-states and functions f_i, h_i are representations of the coefficients of the different monomials in I derived by simplifying the dynamics of the system whose dynamics is described by Eqns. (2.1) & (2.3); their values are presented in Tab. 1.1.

Functions f, h and ψ are indexed to match the definition of $x := [z, v_1, T_c, T_a]'$; that is, ψ_1 is the co-state corresponding to z and ψ_3 corresponds to T_c. Since H_T is quadratic in I, and if $\sum_i \psi_i h_i$ is strictly positive or strictly negative, it would imply that H_T is convex or concave in I respectively.

Next, we show that H_T is convex in I. By definition of H_T and using the definitions in Tab. 1.1,

$$\kappa := \sum_i \psi_i h_i = \psi_3 \alpha_1 R_s(T_c). \tag{1.5}$$

Now, from Lemma A.1, it follows that ψ_3 is positive and so is κ. That is, H_T is convex in I.

The set of admissible current values at any time instant is governed by the constraints on current and terminal voltage. The from these constraints, the admissible control set is

---

[1] The dynamics in Eqn. (1.3) renders the system dynamics lower triangular with T_h being an absorbing node in its graph structure.

Table 1.1: List of placeholders in Eqn. (1.4) and the values/expressions they represent.

Variable	Expression/Value	Variable	Expression/Value	Variable	Expression/Value
f_1	0	g_1	$\frac{-1}{Q \cdot 3600}$	h_1	0
f_2	$\frac{-v_1}{\tau(T_c)}$	g_2	$\frac{1}{C_1(T_c)}$	h_2	0
f_3	$\alpha_1 v_1^2 \frac{C_1(T_c)}{\tau(T_c)} + \alpha_2 T_a + \alpha_3 T_c$	g_3	0	h_3	$\alpha_1 R_s(T_c)$
f_4	$\gamma_1(T_c - T_a) + \gamma_2(w(t) - T_a) - \gamma_3(T_\infty - T_a)$	g_4	0	h_4	0

derived with ease to be

$$\mathcal{I} = \left[0, \min\left\{I_{max}, \frac{v_{oc}(z) - v_1 - v_{min}}{R_s(T_c))}\right\}\right]. \tag{1.6}$$

To maximize H_T, given that $\mathcal{I}$ is compact, the optimal control at any instant takes an extreme value.

Notice that in the above presentation, the actual trajectory of the exogenous input, $w(t)$, has not been of significance. Given that one is free to choose $w(t)$ as needed without changing the result, let $w(t) = T_h(t)$ everywhere to get the final step. ☐

Proof of Lemma II.11. Let the set of feasible initial conditions of (OCP) be denoted by F and X_0 is the largest such set that satisfies Defn. II.10. By definition, for any $x_0 \in X_0$, there exists a control sequence that is feasible with respect to (OCP); i.e. $X_0 \subset F$.

For any $\tilde{x}_0 \in F$, there exists an optimal solution that can drive the battery temperature to T_{des} by t_f without violating state and control trajectories. This by virtue of the fact that X_0 is the largest set of initial conditions such that for each initial condition, there exists a control policy that can drive the temperature to at least T_{des} without violating state constraints, $\tilde{x}_0 \subset X_0$. Thus $F \subset X_0$ and the result follows. ☐

1.2 Backwards Reachable Set Approximation

In this appendix, a methodology to estimate the *ctBRS* and *tBRS* are developed. The techniques presented herein are extensions of the methods presented in [57, 112, 113] in the following two ways: (1) all estimates account for output constraints; (2) the formulation for the inner approximation of the time-limited, free-terminal-time backwards reachable set is a first to our knowledge. The presentation herein attempts to be strike a compromise between being though and concise; only relevant assumptions and results are presented.

This appendix is organized as follows: in Section 1.2.1 some preliminaries are defined and occupation measures and their relation to the flow of system trajectories is introduced. Subsequently, a formulation of a problem to solve for the *ctBRS* is presented in Section 1.2.2. In Section 1.2.3, the numerical implementation technique employed to estimate the *ctBRS* is detailed. Finally, the problem of estimating the rest condition via the *tBRS* is discussed in Section 1.2.4.

1.2.1 Preliminaries

In this section, we introduce the notations adopted in the remainder of this appendix, re-introduce the formulation of the *ctBRS* estimation problem and present the important concept of occupations measures.

1.2.1.1 Notations

In the remainder of this text the following notation is adopted: sets are italicized and capitalized (ex. K). The boundary of a set K is denoted by ∂K. Finite truncations of the set of natural numbers are expressed as $\mathbb{N}_n \coloneqq \{1, \dots, n\}$. The set of continuous functions on a compact set K are denoted by $\mathcal{C}(K)$. The ring of polynomials in x is denoted by $\mathbb{R}[x]$, and the degree of a polynomial is equal to the degree its largest multinomial; the degree of the multinomial x^α, $\alpha \in \mathbb{N}^n$ is $|\alpha| = \|\alpha\|_1$; and $\mathbb{R}_d[x]$ is the set of polynomials in x with maximum degree d. The dual to $\mathcal{C}(K)$ is the set of Radon measures on K, denoted as $\mathcal{M}(K)$, and the pairing of $\mu \in \mathcal{M}(K)$ and $v \in \mathcal{C}(K)$ is:

$$\langle \mu, v \rangle = \int_K v(x)\, d\mu(x). \tag{1.7}$$

We denote the cone of nonnegative Radon measures by $\mathcal{M}_+(K)$. The Lebesgue measure is denoted by λ and the support of a measure, say μ, is identified as $\operatorname{spt}(\mu)$. When considering subsets of a set, we blanketed-ly consider only sets as defined by the Borel σ-algebra.

1.2.1.2 Summarizing the flow of trajectories

Consider a dynamical system whose behaviour can be described by the following ODE:

$$\dot{x} = f(t, x, u), \tag{1.8a}$$

$$y = h(t, x) \tag{1.8b}$$

with the following assumption on the vector-field such as to guarantee uniqueness of solutions and to simplify some of the forgoing developments.

Assumption A.2. *The dynamics of the system is piecewise continuous in t and Lipschitz continuous in x and u.*

This appendix is devoted to the estimation of the backwards reachable set; to do so, we need a tool to describe the flow of solution trajectories that begin in a set. In this dissertation, we relate it to on the viscosity solution of the Liouville equation. In the ensuing presentation, we present the Liouville equation using the notion of *occupation measures*.

The occupation measure $\mu(\cdot \mid x_0) \in \mathcal{M}_+(\mathcal{T} \times X \times U \mid x_0)$ is formally defined as:

$$\mu(A \times B \times C \mid x_0) = \int_0^{t_f} \mathbb{1}_{A \times B \times C}(t, x(t \mid x_0), u(t \mid x_0))\, dt, \tag{1.9}$$

where $\mathbb{1}_K(y)$ is the indicator function on the set K that returns one if $y \in K$ and zero otherwise. That is, given an initial condition, x_0, for the system, the occupation measure quantifies the amount of time spent by solution trajectories in any subset of the space. With the above definition of the occupation measure, it can be shown that:

$$\langle \mu(\cdot \mid x_0), v \rangle = \langle \lambda_t, v(t, x(t \mid x_0), u(t \mid x_0)) \rangle, \tag{1.10}$$

for all $v \in \mathcal{C}(\mathcal{T} \times X \times U)$ where λ_t is the Lebesgue measure on $\mathcal{T}$ [57].

Since we are interested in the collective behavior of a set of initial conditions, we define the *average* occupation measure as:

$$\mu(A \times B \times C) = \int\limits_{\mathcal{T} \times X \times U} \mu(A \times B \times C \mid x)\, d\mu_0, \tag{1.11}$$

where μ_0 is the un-normalized distribution of initial conditions. The value to which the *average* occupation measure evaluates over a given set in $\mathcal{T} \times X \times U$ is the cumulative time spent by all solution trajectories which begin from $\operatorname{spt}(\mu_0)$.

Suppose we were given an $x_0 \in X_0$ where X_0 is an initial set; then we define the first hitting time of a solution to the dynamical system in Eqn. (1.8), γ, of the target with initial condition x_0 as follows:

$$\tau(x_0) = \inf\{t \in \mathcal{T} \mid \gamma(t) \in X_T\}. \tag{1.12}$$

By the Fundamental Theorem of Calculus, one can evaluate a test function $v \in \mathcal{C}^1(\mathcal{T} \times X)$ at time $t = \tau$ along a solution to Eqn. (1.8) as:

$$v(\tau, x(\tau \mid x_0)) = v(0, x_0) + \int\limits_0^{\tau(x_0)} \mathcal{L}_f v(t, x(t \mid x_0), u(t \mid x_0))\, dt \tag{1.13}$$

where the linear operator $\mathcal{L}_f : C^1(\mathcal{T} \times X) \to C(\mathcal{T} \times X \times U)$ is defined as:

$$\mathcal{L}_f v(t, x) = \left(\frac{\partial v}{\partial x} \cdot f + \frac{\partial v}{\partial t} \right)(t, x, u), \tag{1.14}$$

Integrating Eqn. (1.13) with respect to μ_0, the distribution of initial conditions, and defining a new measure $\mu_T \in \mathcal{M}_+(\mathcal{T} \times X_T)$, as:

$$\mu_T(A \times B) = \int\limits_{\mathcal{T} \times X} \mathbb{1}_{A \times B}(\tau, x(\tau \mid x_0))\, d\mu_0, \tag{1.15}$$

produces the following equality

$$\langle \delta_T \otimes \mu_T, v \rangle = \langle \delta_0 \otimes \mu_0, v \rangle + \left\langle \mu, \mathcal{L}_f v \right\rangle, \tag{1.16}$$

where, with a slight abuse of notations, δ_t is used to denote a Dirac measure situated at time t. Using adjoint notations, Eqn. (1.16) can be written as:

$$\delta_T \otimes \mu_T = \delta_0 \otimes \mu_0 + \mathcal{L}_f' \mu. \tag{1.17}$$

Eqn. (1.17) is a version of Liouville's Equation and holds for all test functions $v \in \mathcal{C}^1(\mathcal{T} \times X)$; thus it summarizes the visitation information of all trajectories that emanate from $\text{spt}(\mu_0)$. Several recent papers provide a more detailed discussion on Liouville's Equation [57, 58]. One of the salient features of this equation is highlighted in the following Lemma.

Lemma A.3. *Given measures (μ_0, μ, μ_T) that satisfy the Liouville equation in Eqn.* (1.17)*, there exists a family of solution trajectories that begin in spt(μ_0) and terminates in spt(μ_T).*

Proof. To prove this Lemma, we hybridize the system. Using notions from [114], create an autonomous hybrid system with two modes – mode 1 with dynamics as in Eqn. (1.8); and mode 2 with dynamics $\dot{x} = 0$. Define the guard $G_{(1,2)}$, the condition to transition from mode 1 to mode 2 as $G_{(1,2)} \coloneqq \partial X_T$, and associate with it the identity reset map. Now the remainder of the proof follows by applying Lemma 19 in [114] with the specification that $\Theta = \{0\}$. Note that whilst [114, Lemma 19] does not consider controlled dynamical systems, that result follows with very little change. ☐

1.2.2 Identifying the feasible set

In this section, we address the problem of identifying the controlled time-limited free-terminal-time backwards reachable set. For completeness, the definition of this set is re-stated below.

$$\begin{aligned} X_0^f = \{x_0 \in X \mid \exists u : \mathcal{T} \to U, \text{ st. } \exists \zeta : \mathcal{T} \xrightarrow{dynamics,a.e.} X, \\ \text{with } \zeta(0) = x_0, \forall t \in \mathcal{T}, h(t, \zeta(t)) \in Y, \\ \exists \tau \in \mathcal{T} \text{ st. } \zeta(\tau) \in X_T\}, \end{aligned} \tag{1.18}$$

where X, Y are respectively the state and output manifolds respectively, and U is the set of admissible control values. That is, for any $x \in X_0^f$, there exists a control policy that can drive the state trajectory to the target set (X_T) before time elapses, and without violating any output constraints.

Made specific to the problem considered in Sec. 2.4, the respective sets are defined as follows.

$$
\begin{aligned}
X = \{(z, v_1, T_c, T_h, T_a) \mid\, & T_{min} \le T_h, T_a \le T_{max}, \\
& T^c_{min} \le T_c \le T^c_{max}, \\
& v_{min} \le v_t \le v_{max}, \\
& z_{min} \le z \le z_{max}\}, \\
X_T = \{(z, v_1, T_c, T_h, T_a) \mid\, & T_{min} \le T_h, T_a \le T_{max}, \\
& T_{des} \le T_c \le T^c_{max}, \\
& v_{min} \le v_t \le v_{max}, \\
& z_{limit} \le z \le z_{max}\}.
\end{aligned}
$$

Consider the following infinite dimensional optimization problem on measures

$$\sup_{\Lambda} \qquad \langle \mu_0, \mathbb{1} \rangle \qquad\qquad (P) \tag{1.19a}$$

$$\text{st.} \qquad \mu_0 + \mathcal{L}_f' \mu = \mu_T \tag{1.19b}$$

$$\mu_0 + \hat{\mu}_0 = \lambda_x \tag{1.19c}$$

$$\operatorname{spt}(h_\star \mu) \subset Y \tag{1.19d}$$

where λ_x is the Lebesgue measure supported on X,
$\Lambda := (\mu_0, \hat{\mu}_0, \mu, \mu_T) \in (\mathcal{M}_+(X))^2 \times \mathcal{M}_+(\mathcal{T} \times X \times U) \times \mathcal{M}_+(\mathcal{T} \times X_T)$ and $\mathbb{1}$ denotes the function that takes value 1 everywhere. Problem (P) aims to find the biggest X_0 (wrt. to the Lebesgue measure) as defined in Eqn. (1.18) subject to certain constraints. The constraint in Eqn. (1.19b) enforces that the solution trajectories that emanate from $\operatorname{spt}(\mu_0)$ reach X_T (refer Lemma A.3). The requirement in Eqn. (1.19c) is in place to standardize the measurement frame of reference, the Lebesgue measure. Finally, the constraint in Eqn. (1.19d) requires that output constraints be respected, always.

The following result establishes an important property of problem (P) – that the support

Lemma A.4. *The μ_0 component of the optimal solution of (P) is the restriction of λ_x to X_0^f.*

Proof. The proof of this Lemma follows from [57, Theorem 1] without significant modification. □

Remark A.5. Note that the constraint in Eqn. (1.19d) can be transformed into a constraint on the support of μ via the pullback operation. That is, Eqn. (1.19d) can be removed from (P) by modifying the support constraint on μ; the new constraint reads as

$$\operatorname{spt}(\mu) \subset h^{-1}(Y) \cap \mathcal{T} \times X \times U \tag{1.20}$$

Using Remark A.5 it can be shown that the support of μ can be altered as follows: $\mu \in \mathcal{M}_+(\mathcal{T} \times \Gamma)$ where Γ is defined as:

$$\begin{aligned}\Gamma = \{(z, v_1, T_c, T_h, T_a, I) \mid & v_{min} \leq v_t \leq v_{max}, \\ & 0 \leq I \leq I_{max}, \\ & T_{min} \leq T_h, T_a \leq T_{max}, \\ & T^c_{min} \leq T_c \leq T^c_{max} \\ & z_{min} \leq z \leq z_{max}\}.\end{aligned}$$

In Lemma A.4, it is shown that $\mathrm{spt}(\mu_0)$ is λ_x-identical to X_0; however, identifying the support of measures is nontrivial [115]. Fortunately, there is an alternative and this involves solving the dual problem to (P). The dual problem to (P), on continuous functions, is formulated using standard Infinite-dimensional Linear Program theory [116] and is presented as (D) below.

$$\inf_{w,v} \int_X w \, dx \qquad (D) \quad (1.21a)$$

$$\text{st. } \mathcal{L}_f v(t, x, I) \leq 0 \qquad \forall (t, x, I) \in \mathcal{T} \times \Gamma \quad (1.21b)$$

$$w(x) \geq 0 \qquad \forall x \in X \quad (1.21c)$$

$$w(x) - v(0, x) - 1 \geq 0 \qquad \forall x \in X \quad (1.21d)$$

$$v(t, x) \geq 0 \qquad \forall (t, x) \in \mathcal{T} \times X_T \quad (1.21e)$$

$$v \in \mathcal{C}^1(\mathcal{T} \times X) \qquad (1.21f)$$

$$0 \leq w \in \mathcal{C}(X) \qquad (1.21g)$$

A solution to (D) has the following key characteristics: (a) it is equivalent to (P) in that the optimal costs are the same (b) the w component of the optimal solution can be used to identify X_0^f; as asserted in the following results.

Lemma A.6. *There is no duality gap between problems (P) and (D).*

Proof. The proof is a direct result from duality theory; refer to [116, Theorem 3.10] and [57, Theorem 2]. □

Lemma A.7. *Let (v, w) be a feasible solution to (D). The 1-super-level set of w contains X_0^f.*

Proof. By definition, for any $x_0 \in X_0$, there exists $u(t) \in U$ such that there exists $\tau \in \mathcal{T}$ such that $x(\tau) \in X_T$. Since $v(t,x) \geq 0$ on $\mathcal{T} \times X_T$, using the constraints of (D), it follows that

$$0 \leq v(\tau, x(\tau)) = v(0, x_0) + \int_0^\tau \mathcal{L}_f v, \tag{1.22}$$

$$= v(0, x_0) \leq w(x_0) - 1. \tag{1.23}$$

Thus, the set $\{x \mid w(x) \geq 1\}$ contains X_0^f. □

The above result states that the 1-super-level-set of the w-component of the optimal solution to (D) contains X_0^f; i.e. it is an over approximation of X_0^f. In fact, it is possible to show a stronger result: that w is the indicator function on X_0^f (refer to [57]). Note that while the above result presents a direct means to get an approximation of X_0^f, it is contingent on us being to solve (D). Since (D) is infinite dimensional, in the next section, we use the Lasserre hierarchy to present a sequence of problems that generate a converging sequence of outer approximation of X_0^f.

1.2.3 Numerical implementation

In this section, a sequence of Semidefinite Programs (SDP)s that approximate the solution to the infinite dimensional primal and dual defined in Sec. 1.2.2 are introduced. This sequence of relaxations is constructed by characterizing each measure using a sequence of moments[2] and assuming the following about the description of the system's behavior and of the different sets in the problem.

Assumption A.8. *The dynamical system in Eqn.* (1.8) *is a polynomial. Moreover the domain and the target set are semi-algebraic sets.*

Note that these assumptions are satisfied by the system under considered in this dissertation.

Under this assumption, given any finite d-degree truncation of the moment sequence of all measures in the primal (P), a primal relaxation, (P_d), can be formulated over the moments of measures to construct an SDP. The dual to (P_d), (D_d), can be expressed as a sums-of-squares (SOS) program by considering d-degree polynomials in place of the continuous variables in (D).

To formalize this dual program, first note that a polynomial $p \in \mathbb{R}[x]$ is SOS or $p \in \text{SOS}$ if it can be written as $p(x) = \sum_{i=1}^m q_i^2(x)$ for a set of polynomials $\{q_i\}_{i=1}^m \subset \mathbb{R}[x]$. Note that efficient tools exist to check whether a finite dimensional polynomial is a sum-of-squares (SOS) using SDPs [117]. Next, suppose we are given a semi-algebraic set $A = \{x \in \mathbb{R}^n \mid$

---

[2] The nth moment of a measure (μ) is $y_{\mu,n} = \langle \mu, x^n \rangle$.

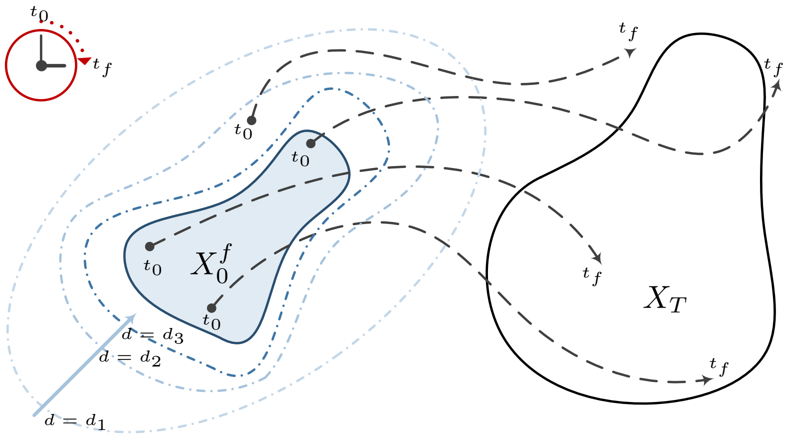

$$(d_1, d_2, d_3) \in \mathbb{N}^3,\ d_1 < d_2 < d_3$$

Figure 1.1: A visual depiction of the convergent sequence of outer approximations of the BRS. The set that is shaded in blue is the true BRS. As the degree relaxation of the approximation problem is increased, the approximations of X_0^f get tighter; they do so only from the outside.

$h_i(x) \geq 0, h_i \in \mathbb{R}[x], \forall i \in \mathbb{N}_m\}$. We define the d-degree *quadratic module* of A as:

$$Q_d(A) = \left\{ q \in \mathbb{R}_d[x] \;\middle|\; \exists \{s_k\}_{k\in\{0,1,\dots,m\}\cup\{0\}} \subset \text{SOS s.t. } q = s_0 + \sum_{k\in\{1,\dots,m\}} h_k s_k \right\} \tag{1.24}$$

The d-degree relaxation of the dual, (D_d), can be written as:

$$\inf_{\Xi_d} \int_X w_d(x)\, d\lambda_x \qquad (D_d) \tag{1.25a}$$

$$\text{st.}\ -\mathcal{L}_f v_d(t, x, \theta) \in Q_d(\mathcal{T} \times \Gamma) \tag{1.25b}$$

$$w_d - v_d(0, x) - 1 \in Q_d(X) \tag{1.25c}$$

$$w_d \in Q_d(X) \tag{1.25d}$$

$$v_d(t, x) \in Q_d(\mathcal{T} \times X_T) \tag{1.25e}$$

where $\Xi_d = \left\{ \left(v_d, w_d\right) \in \mathbb{R}_d[t, x] \times \mathbb{R}_d[x] \right\}$. A primal problem can similarly be constructed, but the solution to the dual can be used to directly generate a sequence of outer approximations to the *ctBRS*. The forthcoming Lemma follows as a direct extension of [57, Theorem 6] and states that as the degree d increases, then w_d converges to w and that we can identify X_0^f, in the limit.

Lemma A.9. *Let w_d denote the w-component of the solution to (D_d). Then $X^c_{(0,d)} = \{x \in X \mid w_d(x) \geq 1\}$ is an outer approximation of X_0^c and $\lim_{d\to\infty} \lambda_x(X^c_{(0,d)} \backslash X_0^f) \searrow 0$.*

Figure 1.1 presents a diagrammatic representation of the convergence of estimates of X_0^f. Lemma A.9 states that as the degree of the polynomial approximation of functions v and w increases, the difference between the volumes of the approximated set $\hat{X}_0^f$ and X_0^f decreases by becoming less positive. In Fig. 1.1, this is represented by the dot-dashed contours that enclose X_0^f, the true *ctBRS* in blue. The progression in degree relaxations is depicted as labels on the contours.

Thus, using a finite-degree truncation of the infinite dimensional problem presented above, one can solve for a sequence of convergent outer approximations of X_0^f.

1.2.4 Identifying the rest condition

In the previous sections, we presented a formulation of an optimization problem that be used to generate outer approximations of the *ctBRS*. In this section, we address the problem of approximating the rest condition, and the associated set, the *tBRS*.

Recall the definition of X_0^r, the time-limited free-terminal-time backwards reachable set, from Sec. 2.3 (re-produced below for convenience)

$$\begin{aligned} X_0^r = \{x_0 \in X \mid \exists \zeta : [0, t_f] \xrightarrow{\text{dynamics a.e.}} X,\, \zeta(0) = x_0, \\ \exists \tau \in [0, t_f],\, \zeta(\tau) \in X_T\}, \end{aligned} \tag{1.26}$$

where ζ is a solution trajectory, X is the state-space and X_T is the target set through which we require solutions pass.

While one might be tempted to solve for X_0^r by making requisite changes to the definition of problem (P) introduced in Appendix 1.2.2, and using the methodology described in Appendix 1.2.3, this will not generate the desired result. In fact, as an extension to Lemma II.5, an outer approximate of X_0^r can be shown to not generate a control trajectory that is feasible with respect to the optimal control problem (OCP) introduced in Sec. 2.2. To ensure that the approximate solution remain feasible (wrt. (OCP)), it is necessary that we derive an inner-approximation of X_0^r, the *tBRS*.

The key observation that we leverage in this section is the following: an *inner approximation* of the X_0^r is the *outer approximation* of $X \backslash X_0^r$, its relative complement. That is, if we could negate all the requirements in Section 1.2.1 and 1.2.2, we would get the inner approximation.

Let the relative complement of X_0^r in Eqn. (1.26), be defined as

$$\begin{aligned} X_0^u = \{x_0 \in X \mid \exists \zeta : \mathcal{T} \xrightarrow{dynamics,a.e.} X, \text{ with } \zeta(0) = x_0, \\ \nexists\, \tau \in \mathcal{T} \text{ st. } \zeta(\tau) \in X_T\}. \end{aligned} \tag{1.27}$$

That is, X_0^u is the set of initial conditions of the system from which the state trajectory during natural relaxation, does not, at any time, enter X_T, but remain in X for all $t \in \mathcal{T}$. Note that X_0^r is not the exact relative complement of X_0^r since it does not include initial conditions that can leave the space X, at some time $\tau < t_f$. The decision to define X_0^u like so was made in view of issues related to numerics. To ensure that trajectories do not 'escape' the space at some time, we need the following assumption:

Assumption A.10. *The set $X \backslash X_0^r$ is t_f-invariant.*

Now, similar to problem (P), the problem to estimate $\bar{X}_0^r$ is formulated as follows:

$$\begin{aligned}
\sup_{\Lambda} \quad & \langle \mu_0, \mathbb{1} \rangle && (P^{rest}) \quad (1.28a)\\
\text{st.} \quad & \mu_0 + \mathcal{L}_f' \mu = \mu_T && (1.28b)\\
& \mu_0 + \hat{\mu}_0 = \lambda_x && (1.28c)\\
& \operatorname{spt}(h_\star \mu) \subset Y && (1.28d)
\end{aligned}$$

where λ_x is the Lebesgue measure supported on X,
$\Lambda := (\mu_0, \hat{\mu}_0, \mu, \mu_T) \in (\mathcal{M}_+(X))^2 \times \mathcal{M}_+(\mathcal{T} \times X \backslash X_T) \times \mathcal{M}_+(\mathcal{T} \times X \backslash X_T)$ and $\mathbb{1}$ denotes the function that takes value 1 everywhere. The sets X and X_T to identify X_0^r such as to extract the rest condition are defined as

$$\begin{aligned}
X = \{(z, v_1, T_c, T_h, T_a) \,|\, & T_{min} \le T_h, T_a \le T_{max},\\
& T_{min} \le T_c \le T_{max}^c,\\
& z_{min} \le z \le z_{max}\},\\
X_T = \{(z, v_1, T_c, T_h, T_a) \,|\, & T_{min} \le T_h, T_a \le T_{max},\\
& T_{des} \le T_c \le T_{max}^c,\\
& z_{limit} \le z \le z_{max}\}.
\end{aligned}$$

Problem (P^{rest}) aims to find the biggest X_0^u (wrt. to the Lebesgue measure) as defined in Eqn. (1.27) subject to the usual constraints. The constraint in Eqn. (1.28b) enforces that the solution trajectories that emanate from $\operatorname{spt}(\mu_0)$ remain in $X \backslash X_T$ for all time $t \in \mathcal{T}$. The requirement in Eqn. (1.28c) is in place to standardize the measurement frame of reference, the Lebesgue measure. Finally, the constraint in Eqn. (1.28d) requires that output constraints be respected, always. Note that Remark A.5 is still relevant.

The dual to (P^{rest}), is derived using standard techniques and is presented below.

$$\begin{aligned}
&\inf_{w,v} \int_X w\,dx && (D^{rest}) \quad (1.29a)\\
&\text{st. } \mathcal{L}_f v(t,x) \le 0 && \forall (t,x) \in \mathcal{T} \times X \backslash X_T \quad (1.29b)\\
&w(x) \ge 0 && \forall x \in X \quad (1.29c)\\
&w - v(0,\cdot) - 1 \ge 0 && \forall x \in X \quad (1.29d)\\
&v(t,x) \ge 0 && \forall (t,x) \in \mathcal{T} \times X \backslash X_T \quad (1.29e)\\
&v \in \mathcal{C}^1(\mathcal{T} \times X) && (1.29f)\\
&0 \le w \in \mathcal{C}(X) && (1.29g)
\end{aligned}$$

where $x = [z, v_1, T_c, T_a, T_h]'$.

A solution to (D^{rest}) has the following characteristics: (a) the optimal cost is the volume of the complement of the largest *tBRS*; (b) $w = 0$ on the *tBRS* and 1 elsewhere. That is, given the optimal solution to (D^{rest}), its w-component, w^*, defines the *tBRS* of X_T as follows:

$$X_0^r = \{x \mid w(x)^* < 1\}. \tag{1.30}$$

Recall that X_0^r is the set of initial conditions from which the self-driven system reaches the desired cell temperature by the specified time. Thus, the boundary of X_0^u serves as the switching surface.

Results analogous to Lemmas A.4—A.7 still hold in this case; with the primary difference being that the support of μ_0 is now $\bar{X}_0^u$ and that the 1-super-level-set of the w component of (D^{rest}) is an outer approximation of $\bar{X}_0^u$ and hence an inner approximation of X_0^r.

Lemma A.11. *Under Assumption A.10, the μ_0 component of the optimal solution to (P^{rest}) is the restriction of λ_x to X_0^u.*

Lemma A.12. *The electro-thermal model described in Sec. 2.1 satisfies Assumption A.10.*

Numerical approximations of the solution to w are derived as discussed in Section 1.2.3, and the similar results exist for this problem formulation as well; these are omitted for brevity. Figure 1.2 presents a summary of the numerical estimation strategy employed to identify X_0^r. Using the estimate of X_0^r, the rest condition is identified as the zero set of $w - 1$.

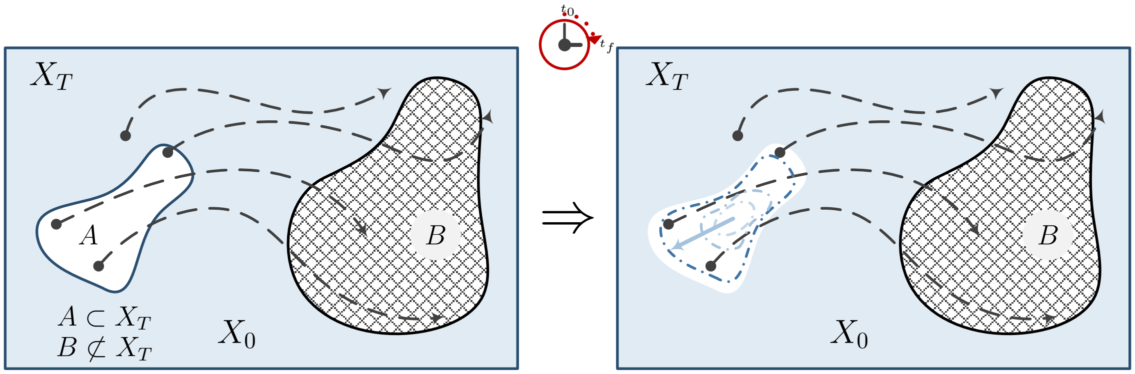

(a)

(b)

Figure 1.2: How to generate inner approximations of the BRS. Subplot (a) presents the complement problem – where the pattern-ed set, which once was the target set, is to be avoided at all times, and the new target set is the set in blue and white. This formulation is equivalent to finding the largest set of initial conditions such that the safe set is invariant. The set A is such that trajectories that begin in it reach the avoid set at some before $t = t_f$; it is not a part of the solution to the complement problem. The solution to the complement problem is $X_T \backslash A$. Thus, using a version of Lemma A.9, the solution to (P^{rest}) is approximated from outside; i.e. inside of A. This produces an inner approximation of A.

Appendix B

Appendix to Chapter IV

2.1 The Significance Metric

In this section, a basis for defining the significance metric as was done in Sec. 4.3 is provided.

2.1.1 Metric definition

The significance metric used in this study to the partition the aSP is based on the notion of relative estimability. Consider $N+1$ sequential measurements of the terminal voltage stacked into a vector Y defined without loss of generality as

$$Y = [V_{t,k}, \dots, V_{t,k+N}]'. \tag{2.1}$$

The relative estimability of the states and parameters of the electrical model — SOC, R_s, v, R_1, C_1 — can be measured by the quantitatively comparing the significance of perturbations to each member of the aSP on the output. If the initial conditions (values of states and parameters at instant k) are denoted as $\theta \in \mathbb{R}^5$, then the sensitivity matrix—which satisfies the relation

$$\delta Y = \mathbf{S}\delta\theta, \tag{2.2}$$

where δY is the resulting perturbation in output from a $\delta\theta$ perturbation in initial conditions—is given by

$$\mathbf{S} = \begin{bmatrix} \frac{\partial V_{t,k}}{\partial \theta_1} & \cdots & \frac{\partial V_{t,1}}{\partial \theta_k} \\ \cdots & \ddots & \vdots \\ \frac{\partial V_{t,k+N}}{\partial \theta_1} & \cdots & \frac{\partial V_{t,k+N}}{\partial \theta_k} \end{bmatrix}. \tag{2.3}$$

Since the states and parameters are not all of the same units and magnitudes, we first normalize the sensitivity matrix, S, about a nominal value of initial conditions (θ_{nom}) and the resulting voltages (Y_{nom}). Further, define the unit normalized sensitivity matrix $\mathbf{H}$ as follows.

$$\mathbf{H} = [\text{diag}(Y_{nom})]^{-1}\,\mathbf{S}[\text{diag}(\theta_{nom})] \tag{2.4}$$

We define the influence of each parameter θ_i on the output as the amplification of the natural basis in the perturbed aSP through the linear operator $\mathbf{H}$. That is, the influence of parameter i, $\bar{\bar{\zeta}}_i$, on the output is measured as

$$\bar{\bar{\zeta}}_i = \|\mathbf{H}e_i\|_2^2 \tag{2.5}$$

where e_i is the $i$the natural basis of the perturbed parameter space. This expression can be reduced as follows:

$$\begin{aligned}\bar{\bar{\zeta}}_i &= \|\mathbf{H}e_i\|_2^2 && (2.6a)\\ &= ||\mathbf{U\Sigma V}^T e_i||_2^2 && (2.6b)\\ &= ||\mathbf{\Sigma V}^T e_i||_2^2 && (2.6c)\\ &= \sum_{j=1}^{N}\left(\sigma_j^2 c_{j,i}\right)^2 && (2.6d)\end{aligned}$$

where

$$\mathbf{H} = \mathbf{U}\Sigma\mathbf{V}^T = \mathbf{U}\begin{bmatrix} \sigma_1^2 & \cdots & 0 \\ \vdots & \ddots & \vdots \\ 0 & \cdots & \sigma_5^2 \\ 0 & \cdots & 0 \\ \vdots & \ddots & \vdots \\ 0 & \cdots & 0 \end{bmatrix}\begin{bmatrix} | & | & | \\ c_1 & \cdots & c_5 \\ | & | & | \end{bmatrix}^T \tag{2.7}$$

is the Singular Value Decomposition (SVD) of $\mathbf{H}$ with c_i being columns in $\mathbf{V}$. For ease of comparison, the values of the significance metrics are normalized to arrive at the following expression for the normalized significance metric:

$$\bar{\zeta}_i = \frac{\sum_{j=1}^{N}\left(\sigma_j^2 c_{j,i}\right)^2}{\sum_{j=1}^{N}(\sigma_j^2)^2}. \tag{2.8}$$

Another variant of the above expression can be derived by loosely using the equivalence of norms in finite dimensional spaces to convert expression form the 2-norm to 1-norm; this expression of the normalized significance metric is given by

$$\bar{\eta}_i = \frac{\sum_{j=1}^{N} |\sigma_j^2 c_{j,i}|}{\sum_{j=1}^{N} \sigma_j^2}. \tag{2.9}$$

For any two distinct parameters, θ_i and θ_j, based on the above definition of the significance metric, θ_i is a more significant parameter on the output and hence is more estimable than θ_j if $\bar{\zeta}_i > \bar{\zeta}_j$ or $\bar{\eta}_i > \bar{\eta}_j$.

2.1.2 A heuristic EKF tuning technique

The EKF is arguably one order of complexity higher than the Linear Quadratic Estimator (LQE) and consists of a sequence of update laws that are executed at every sampling instant. The update laws are based on the idea that a nonlinear dynamical system can be locally approximated by a linear system, and hence designing a LQE for the local linear system is usually adequate to guarantee boundedness of estimation errors. The general presentation of the update laws of the EKF are delineated in Sec. 2.2.

The EKF has two tunable parameters: $\mathbf{Q}$ and $\mathbf{R}$ representing the 'covariance' of the process and measurement uncertainties respectively. These parameters require tuning owing to modeling uncertainty introduced in having assumed that the dynamics of a nonlinear system by linear equations, and because the true process noise's characteristic is seldom known. It is standard practice to fix on the these matrices and tune the other, often preferring diagonal matrices. In the following discussion we suggest that the value of $\mathbf{Q}$ be fixed and present a method to compute this value.

The tuning parameters $\mathbf{Q}$ and $\mathbf{R}$ can be interpreted as weighting matrices that express the relative confidence in either the systems dynamics and on the measurements. In this section, we suggest that $\mathbf{Q}$ be chosen with entries to reflect the relative confidence in each model state/parameter. Suppose parameter i is more estimable from output measurements than parameter j, then to reflect this expectation, we set $\mathbf{Q}_{j,j} > \mathbf{Q}_{i,i} > 0$. The actual values of each diagonal entry and their relative difference is chosen to be dictated by the Cramér-rao bound.

The Cramér-rao bound (CRB) provides a lower bound on the variance that any unbiased estimator can achieve from a given data. This matrix can be computed from the sensitivity matrix [88]; in this paper, we use the normalized sensitivity matrix $\mathbf{H}$.

$$\mathbf{\Sigma}_{CRB} = (\mathbf{H}^T \mathbf{H})^{-1} \tag{2.10}$$

Using the SVD decomposition of $\mathbf{H}$ as presented in Eqn.(2.7), Σ_{CRB} can be expressed as

$$\begin{aligned} \mathbf{\Sigma}_{CRB} &= (\mathbf{V}\mathbf{\Sigma}^T\mathbf{U}^T\mathbf{U}\mathbf{\Sigma}\mathbf{V}^T)^{-1} && \text{(2.11a)} \\ &= (\mathbf{V}\mathbf{\Sigma}^T\mathbf{\Sigma}\mathbf{V}^T)^{-1} && \text{(2.11b)} \\ &= \mathbf{V}(\mathbf{\Sigma}^T\mathbf{\Sigma})^{-1}\mathbf{V}^T && \text{(2.11c)} \end{aligned}$$

Suppose now that $\mathbf{\Sigma}_{CRB}$ was diagonal, i.e. estimates of every state did not affect the other states, then the lower bound on achievable variance corresponding to each parameter i is given by

$$\begin{aligned} \hat{\sigma}_i^2 &= e_i^T \mathbf{\Sigma}_{CRB}\, e_i && \text{(2.12a)} \\ &= e_i^T \mathbf{V}(\mathbf{\Sigma}^T\mathbf{\Sigma})^{-1}\mathbf{V}^T e_i && \text{(2.12b)} \\ &= (\|\mathbf{V}\Sigma e_i\|_2^2)^{-1} && \text{(2.12c)} \\ &= \frac{1}{\bar{\bar{\zeta}}_i} && \text{(2.12d)} \end{aligned}$$

Thus, we set each diaginal entry in $\mathbf{Q}$ according to the relative significance metric (since the absolute value is not important).

$$q_{i,i} = \frac{1}{\bar{\zeta}_i} \tag{2.13}$$

In the case of the 2ECM, since the relative significance does not change considerably, the averaged significance metric is used to build $\mathbf{Q}$. With $\mathbf{Q}$ defined thus, $\mathbf{R}$ is tuned with the following form

$$\mathbf{R} = \gamma\,\mathbf{I}_5 \tag{2.14}$$

where $\gamma > 0$ is the tuning parameter and $\mathbf{I}_5$ is the dimension 5 identity matrix.

As a review, $\zeta_i, \forall i \in \{1, \ldots, 5\}$ were computed from $\mathbf{H}$, a normalized version of $\mathbf{S}$. To be able to use $\mathbf{Q}$ in the original system, the effect of normalizing $\mathbf{S}$ has to be undone. For example, the EKF on group 1, $\mathbf{Q}$ is defined as

$$\mathbf{Q}_1 = \begin{bmatrix} \zeta_{SOC} \cdot SOC_{nom}^2 & 0 & 0 \\ 0 & \zeta_{nom} \cdot v_{nom}^2 & 0 \\ 0 & 0 & \zeta_{R_s} \cdot R_{s,nom}^2 \end{bmatrix}. \tag{2.15}$$

2.2 Overview of the Extended Kalman Filter

A brief summary of the EKF methodology used in Section 4.4 is provided in this appendix. Considering a dynamical system described by

$$\begin{aligned}\tilde{x}_{k+1} &= f(\tilde{x}_k, u_k) + v_k,\\ y_k &= g(\tilde{x}_k, u_k) + w_k,\end{aligned}$$

with the process and measurement noises, v_k and w_k respectively, define the following

$$\mathbf{A}_{k-1} = \left.\frac{\partial f}{\partial \tilde{x}}\right|_{\left\{\begin{array}{c}\tilde{x} = \hat{\tilde{x}}^{+}_{k-1}\\ u = u_{k-1}\end{array}\right\}}, \mathbf{C}_k = \left.\frac{dg}{d\tilde{x}}\right|_{\left\{\begin{array}{c}\tilde{x} = \hat{\tilde{x}}^{-}_{k}\\ u = u_{k}\end{array}\right\}}.$$

The design of each EKF estimator is given as the following update processes assuming that the covariances of the process and measurements noises are defined as $\mathbf{Q} := E\{v_k' v_k\}$ and $\mathbf{R} := E\{w_k' w_k\}$ respectively.
Time update for the state filter:

$$\begin{aligned}\hat{\tilde{x}}^{-}_{k} &= \mathbf{A}_{k-1}\hat{\tilde{x}}^{+}_{k-1} + \mathbf{B}_{k-1}u_{k-1},\\ \mathbf{P}^{-}_{k} &= \mathbf{A}_{k-1}\mathbf{P}^{+}_{k-1}\mathbf{A}^{T}_{k-1} + \mathbf{Q}.\end{aligned}$$

Measurement update for the state filter:

$$\begin{aligned}\mathbf{K}_k &= \mathbf{P}^{-}_{k}\mathbf{C}_k{}^{T}\left[\mathbf{C}_k\mathbf{P}^{-}_{k}\mathbf{C}_k{}^{T} + \mathbf{R}\right]^{-1},\\ \hat{\tilde{x}}^{+}_{k} &= \hat{\tilde{x}}^{-}_{k} + \mathbf{K}_k\left[y_k - f_{u_k}(\hat{\tilde{x}}^{-}_{k})\right],\\ \mathbf{P}^{+}_{k} &= \left[\mathbf{I} - \mathbf{K}_k\mathbf{C}_k\right]\mathbf{P}^{-}_{k}.\end{aligned}$$

BIBLIOGRAPHY

BIBLIOGRAPHY

[1] B. Dunn, H. Kamath, and J.-M. Tarascon, "Electrical energy storage for the grid: a battery of choices," *Science*, vol. 334, no. 6058, pp. 928–935, 2011.

[2] C.-Y. Wang, G. Zhang, S. Ge, T. Xu, Y. Ji, X.-G. Yang, and Y. Leng, "Lithium-ion battery structure that self-heats at low temperatures," *Nature*, 2016.

[3] S. Mohan, J. B. Siegel, A. G. Stefanopoulou, and R. Vasudevan, "An Energy-Optimal Warm-Up Strategy for Li-ion Batteries and its Approximations," in preparation.

[4] E. Gies, "Can wind and solar fuel africa's future?" *Nature*, vol. 539, no. 7627, p. 20, 2016.

[5] "Electricity energy storage technology options," Electric Power Research Institute, Tech. Rep., 2010.

[6] S. Mohan, A. Hooshmand, S. A. P. Kani, and R. Sharma, "Bss sizing and economic benefit analysis in grid-scale application," in *IEEE PES Innovative Smart Grid Technologies (ISGT) North America*, 2016.

[7] Extreme temperatures affect electric vehicle driving range. (2014, March) http://newsroom.aaa.com/2014/03/extreme-temperatures-affect-electric-vehicle-driving-range-aaa-says. AAA. Online. Accessed on 2/21/2016.

[8] A. Affanni, A. Bellini, G. Franceschini, P. Guglielmi, and C. Tassoni, "Battery choice and management for new-generation electric vehicles," *IEEE Trans. Ind. Electron.*, vol. 52, no. 5, pp. 1343–1349, Oct 2005.

[9] H. Rahimi-Eichi, U. Ojha, F. Baronti, and M. Chow, "Battery management system: An overview of its application in the smart grid and electric vehicles," *IEEE Trans. Ind. Electron.*, vol. 7, no. 2, pp. 4–16, June 2013.

[10] R. Huggins, *Advanced Batteries: Materials Science Aspects, first edition.* Springer, 2008.

[11] Z. Rao and S. Wang, "A review of power battery thermal energy management," *Renewable and Sustainable Energy Reviews*, vol. 15, no. 9, pp. 4554–4571, 2011.

[12] J. Vetter, P. Novák, M. Wagner, C. Veit, K.-C. Möller, J. Besenhard, M. Winter, M. Wohlfahrt-Mehrens, C. Vogler, and A. Hammouche, "Ageing mechanisms in lithium-ion batteries," *Journal of power sources*, vol. 147, no. 1, pp. 269–281, 2005.

[13] S. Zhang, K. Xu, and T. Jow, "Low temperature performance of graphite electrode in Li-ion cells," *Electrochimica Acta*, vol. 48, no. 3, pp. 241–246, 2002.

[14] ——, “The low temperature performance of Li-ion batteries,” *Journal of Power Sources*, vol. 115, no. 1, pp. 137–140, 2003.

[15] S. Zhang, K. Xu, J. Allen, and T. Jow, “Effect of propylene carbonate on the low temperature performance of li-ion cells,” *Journal of power sources*, vol. 110, no. 1, pp. 216–221, 2002.

[16] C. K. Huang, J. S. Sakamoto, J. Wolfenstine, and S. Surampudi, “The limits of low-temperature performance of Li-Ion cells,” *Journal of The Electrochemical Society*, vol. 147, no. 8, pp. 2893–2896, 2000.

[17] T. Waldmann, M. Wilka, M. Kasper, M. Fleischhammer, and M. Wohlfahrt-Mehrens, “Temperature dependent ageing mechanisms in lithium-ion batteries–a post-mortem study,” *Journal of Power Sources*, vol. 262, pp. 129–135, 2014.

[18] J. Jaguemont, L. Boulon, and Y. Dubé, “A comprehensive review of lithium-ion batteries used in hybrid and electric vehicles at cold temperatures,” *Applied Energy*, vol. 164, pp. 99–114, 2016.

[19] S. Herreyre, O. Huchet, S. Barusseau, F. Perton, J. Bodet, and P. Biensan, “New li-ion electrolytes for low temperature applications,” *Journal of power sources*, vol. 97, pp. 576–580, 2001.

[20] E. Plichta and W. Behl, “A low-temperature electrolyte for lithium and lithium-ion batteries,” *Journal of Power Sources*, vol. 88, no. 2, pp. 192 – 196, 2000.

[21] E. Plichta, M. Hendrickson, R. Thompson, G. Au, W. Behl, M. Smart, B. Ratnakumar, and S. Surampudi, “Development of low temperature li-ion electrolytes for nasa and dod applications,” *Journal of power sources*, vol. 94, no. 2, pp. 160–162, 2001.

[22] M. C. Smart and B. V. Ratnakumar, “Effect of cell design parameters on lithium plating in lithium-ion cells,” *Journal of the Electrochemical Society*, vol. 158(4), pp. 279–389, 2011.

[23] Y. Ji, Y. Zhang, and C.-Y. Wang, “Li-ion cell operation at low temperatures,” *Journal of The Electrochemical Society*, vol. 160(4), pp. 636–649, 2013.

[24] N. Gunawardhana, N. Dimov, M. Sasidharan, G.-J. Park, H. Nakamura, and M. Yoshio, “Suppression of lithium deposition at sub-zero temperatures on graphite by surface modification,” *Electrochemistry Communications*, vol. 13, no. 10, pp. 1116–1118, 2011.

[25] A. Pesaran, A. Vlahinos, and T. STUART, “Cooling and preheating of batteries in hybrid electric vehicles,” in *The 6th ASME-JSME Thermal Engineering Joint Conference*, 2003.

[26] T. Stuart and A. Hande, “HEV battery heating using ac currents,” *Journal of Power Sources*, vol. 129, no. 2, pp. 368 – 378, 2004.

[27] E. A. Muller, A. G. Stefanopoulou, and L. Guzzella, “Optimal power control of hybrid fuel cell systems for an accelerated system warm-up,” *Control Systems Technology, IEEE Transactions on*, vol. 15, no. 2, pp. 290 –305, march 2007.

[28] Y. Ji, Y. Zhang, and C.-Y. Wang, "Li-Ion cell operation at low temperatures," *Journal of The Electrochemical Society*, vol. 160, no. 4, pp. A636–A649, 2013.

[29] H.-S. Song, J.-B. Jeong, B.-H. Lee, D.-H. Shin, B.-H. Kim, T.-H. Kim, and H. Heo, "Experimental study on the effects of pre-heating a battery in a low-temperature environment," in *2012 IEEE Vehicle Power and Propulsion Conference.* IEEE, 2012, pp. 1198–1201.

[30] H. Baba, K. Kawasaki, and H. Kawachi, "Battery heating system for electric vehicles," SAE Technical Paper, Tech. Rep., 2015.

[31] S. Al Hallaj and J. R. Selman, "A novel thermal management system for electric vehicle batteries using phase change material," *Journal of The Electrochemical Society*, vol. 147, no. 9, pp. 3231–3236, 2000.

[32] T. F. Fuller, M. Doyle, and J. Newman, "Simulation and optimization of the dual lithium ion insertion cell," *Journal of The Electrochemical Society*, vol. 141, no. 1, pp. 1–10, 1994.

[33] J. C. Forman, S. Bashash, J. L. Stein, and H. K. Fathy, "Reduction of an electrochemistry-based Li-Ion battery model via quasi-linearization and padé approximation," *Journal of The Electrochemical Society*, vol. 158, no. 2, pp. A93–A101, 2011.

[34] L. Song and J. W. Evans, "Electrochemical-thermal model of lithium polymer batteries," *Journal of The Electrochemical Society*, vol. 147, no. 6, pp. 2086–2095, 2000.

[35] B. S. Haran, B. N. Popov, and R. E. White, "Determination of the hydrogen diffusion coefficient in metal hydrides by impedance spectroscopy," *Journal of Power Sources*, vol. 75, no. 1, pp. 56–63, 1998.

[36] G. Ning and B. N. Popov, "Cycle life modeling of lithium-ion batteries," *Journal of The Electrochemical Society*, vol. 151, no. 10, pp. A1584–A1591, 2004.

[37] T. R. Tanim, C. D. Rahn, and C.-Y. Wang, "A temperature dependent, single particle, lithium ion cell model including electrolyte diffusion," *Journal of Dynamic Systems, Measurement, and Control*, vol. 137, no. 1, p. 011005, 2015.

[38] Y. Hu and S. Yurkovich, "Linear parameter varying battery model identification using subspace methods," *Journal of Power Sources*, vol. 196, no. 5, pp. 2913–2923, 2011.

[39] S. Tippmann, D. Walper, L. Balboa, B. Spier, and W. G. Bessler, "Low-temperature charging of lithium-ion cells part I: Electrochemical modeling and experimental investigation of degradation behavior," *Journal of Power Sources*, vol. 252, pp. 305 – 316, 2014.

[40] S. Mohan, Y. Kim, A. Stefanopoulou, and Y. Ding, "On the warmup of li-ion cells from sub-zero temperatures," in *American Control Conference (ACC), 2014*, June 2014, pp. 1547–1552.

[41] X. Lin, H. E. Perez, S. Mohan, J. B. Siegel, A. G. Stefanopoulou, Y. Ding, and M. P. Castanier, "A lumped-parameter electro-thermal model for cylindrical batteries," *Journal of Power Sources*, vol. 257, no. 0, pp. 1 – 11, 2014.

[42] M. Allen. (2014, Jan.) Cold Weather Fuel Efficiency : Electric Versus Gasoline Showdown. Online. Accessed on 11/12/2016. [Online]. Available: http://www.fleetcarma.com/cold-weather-fuel-efficiency/

[43] Y. Kim, S. Mohan, N. A. Samad, J. B. Siegel, and A. G. Stefanopoulou, "Optimal power management for a series hybrid electric vehicle cognizant of battery mechanical effects," in *American Control Conference (ACC), 2014*, June 2014, pp. 3832–3837.

[44] S. Mohan, Y. Kim, J. B. Siegel, N. A. Samad, and A. G. Stefanopoulou, "A phenomenological model of bulk force in a li-ion battery pack and its application to state of charge estimation," *Journal of the Electrochemical Society*, vol. 161, no. 14, pp. A2222–A2231, 2014.

[45] S. Mohan, Y. Kim, and A. G. Stefanopoulou, "Energy-conscious warm-up of li-ion cells from subzero temperatures," *IEEE Transactions on Industrial Electronics*, vol. 63, no. 5, pp. 2954–2964, May 2016.

[46] ——, "Estimating the Power Capability of Li-ion Batteries Using Informationally Partitioned Estimators," *IEEE Transactions on Control Systems Technology*, vol. 24, no. 5, pp. 1643–1654, Sept 2016.

[47] S. Mohan, V. Shia, and R. Vasudevan. (2016, January) Convex computation of the reachable set for hybrid systems with parametric uncertainty. Online, arxiv. ArXiv:1601.01019.

[48] S. M. J. B. Siegel and A. G. Stefanopoulou, "Comparing optimal warm-up strategies of li-ion batteries," 2017, in Preparation.

[49] P. Holmes, S. Kousik, S. Mohan, and R. Vasudevan, "Convex Estimation of the α-level Reachable Sets of Systems with Parametric Uncertainty," in *2016 IEEE 55nd Annual Conference on Decision and Control (CDC)*, 2016.

[50] S. Mohan, J. B. Siegel, A. G. Stefanopoulou, M. Castanier, and Y. Ding, "Synthesis of an energy-optimal self-heating strategy for li-ion batteries," in *2016 IEEE 55nd Annual Conference on Decision and Control (CDC)*. IEEE, 2016.

[51] S. Mohan, Y. Kim, J. B. Siegel, and A. G. Stefanopoulou, "On improving battery state of charge estimation using bulk force measurements," in *ASME Dynamic Systems and Control Conference*, 2015.

[52] S. Mohan and R. Vasudevan, "Convex computation of the reachable set for hybrid systems with parametric uncertainty," in *2016 American Control Conference (ACC)*, July 2016, pp. 5141–5147.

[53] Military Batteries & Systems. http://www.navitassys.com/products-systems/military-batteries-systems/. Navitas Systems. Online. Accessed on 11/9/2016.

[54] W. B. Gu and C. Y. Wang, "Thermal-electrochemical modeling of battery systems," *Journal of The Electrochemical Society*, vol. 147, no. 8, pp. 2910–2922, 2000.

[55] Y. Ji and C. Y. Wang, "Heating strategies for Li-ion batteries operated from subzero temperatures," *Electrochimica Acta*, vol. 107, no. 0, pp. 664–674, 2013.

[56] I. M. Mitchell, A. M. Bayen, and C. J. Tomlin, "A time-dependent hamilton-jacobi formulation of reachable sets for continuous dynamic games," *IEEE Transactions on automatic control*, vol. 50, no. 7, pp. 947–957, 2005.

[57] D. Henrion and M. Korda, "Convex computation of the region of attraction of polynomial control systems," *IEEE Transactions on Automatic Control*, vol. 59, no. 2, pp. 297–312, 2014.

[58] S. Mohan, Y. Kim, and A. G. Stefanopoulou, "Energy-conscious warm-up of li-ion cells from subzero temperatures," *IEEE Transactions on Industrial Electronics*, vol. 63, no. 5, pp. 2954–2964, May 2016.

[59] C. Forgez, D. Vinh Do, G. Friedrich, M. Morcrette, and C. Delacourt, "Thermal modeling of a cylindrical $\mathrm{LiFePO_4}$/graphite lithium-ion battery," *Journal of Power Sources*, vol. 195, no. 9, pp. 2961–2968, 2010.

[60] Y. Kim, J. B. Siegel, and A. G. Stefanopoulou, "A computationally efficient thermal model of cylindrical battery cells for the estimation of radially distributed temperatures," in *Proceedings of the American Control Conference*, Jun 17-19 2013, pp. 698–703.

[61] P. Zhao, S. Mohan, and R. Vasudevan. (2016) Convex synthesis of solutions to hybrid nonlinear optimal control problems. In preparation.

[62] I. M. Ross and M. Karpenko, "A review of pseudospectral optimal control: from theory to flight," *Annual Reviews in Control*, vol. 36, no. 2, pp. 182–197, 2012.

[63] M. A. Patterson and A. V. Rao, "GPOPS-II: A MATLAB software for solving multiple-phase optimal control problems using hp-adaptive gaussian quadrature collocation methods and sparse nonlinear programming," *ACM Transactions on Mathematical Software (TOMS)*, vol. 41, no. 1, p. 1, 2014.

[64] I. M. Mitchell and C. J. Tomlin, "Overapproximating reachable sets by hamilton-jacobi projections," *journal of Scientific Computing*, vol. 19, no. 1-3, pp. 323–346, 2003.

[65] J.-P. Aubin and A. Cellina, *Differential inclusions: set-valued maps and viability theory.* Springer Science & Business Media, 2012, vol. 264.

[66] S. Margolis and W. Vogt, "Control engineering applications of v. i. zubov's construction procedure for lyapunov functions," *IEEE Transactions on Automatic Control*, vol. 8, no. 2, pp. 104–113, Apr 1963.

[67] S. Mohan, A. G. Stefanopoulou, and R. Vasudevan, "Feedback synthesis and reachability verification of controlled polynomial stochastic differential systems," in preparation.

[68] S. Mohan, J. B. Siegel, A. G. Stefanopoulou, M. Castanier, and Y. Ding, "Synthesis of an energy-optimal self-heating strategy for li-ion batteries," in *2016 IEEE 55nd Annual Conference on Decision and Control (CDC).* IEEE, 2016.

[69] J. Shim, R. Kostecki, T. Richardson, X. Song, and K. Striebel, "Electrochemical analysis for cycle performance and capacity fading of a lithium-ion battery cycled at elevated temperature," *Journal of Power Sources*, vol. 112, no. 1, pp. 222–230, 2002.

[70] R. Spotnitz and J. Franklin, “Abuse behavior of high-power, lithium-ion cells,” *Journal of Power Sources*, vol. 113, no. 1, pp. 81–100, 2003.

[71] G. Plett, “High-performance battery-pack power estimation using a dynamic cell model,” *Vehicular Technology, IEEE Transactions on*, vol. 53, no. 5, pp. 1586–1593, 2004.

[72] M. Verbrugge and B. Koch, “Generalized recursive algorithm for adaptive multiparameter regression: Application to lead acid, nickel metal hydride, and lithium-ion batteries,” *Journal of The Electrochemical Society*, vol. 153, no. 1, pp. A187–A201, 2006.

[73] R. D. Anderson, Y. Zhao, X. Wang, X. G. Yang, and Y. Li, “Real time battery power capability estimation,” in *Proceedings of the American Control Conference*, June 2012, pp. 592–597.

[74] R. Xiong, H. He, F. Sun, X. Liu, and Z. Liu, “Model-based state of charge and peak power capability joint estimation of lithium-ion battery in plug-in hybrid electric vehicles,” *Journal of Power Sources*, vol. 229, no. 0, pp. 159–169, 2013.

[75] K. Smith, C. Rahn, and C.-Y. Wang, “Model-based electrochemical estimation and constraint management for pulse operation of lithium ion batteries,” *Control Systems Technology, IEEE Transactions on*, vol. 18, no. 3, pp. 654–663, 2010.

[76] H. Perez, N. Shahmohammadhamedani, and S. Moura, “Enhanced performance of Li-Ion batteries via modified reference governors and electrochemical models,” *Mechatronics, IEEE/ASME Transactions on*, vol. PP, no. 99, pp. 1–10, 2015.

[77] G. L. Plett, “Extended Kalman filtering for battery management systems of LiPB-based HEV battery packs: Part 3. state and parameter estimation,” *Journal of Power Sources*, vol. 134, no. 2, pp. 277–292, 2004.

[78] K. Schittkowski, “Experimental design tools for ordinary and algebraic differential equations,” *Industrial & Engineering Chemistry Research*, vol. 46, no. 26, pp. 9137–9147, 2007.

[79] B. R. Jayasankar, A. Ben-Zvi, and B. Huang, “Identifiability and estimability study for a dynamic solid oxide fuel cell model,” *Computers & Chemical Engineering*, vol. 33, no. 2, pp. 484–492, 2009.

[80] A. P. Schmidt, M. Bitzer, Áprád W. Imre, and L. Guzzella, “Experiment-driven electrochemical modeling and systematic parameterization for a lithium-ion battery cell,” *Journal of Power Sources*, vol. 195, no. 15, pp. 5071 – 5080, 2010.

[81] J. C. Forman, S. J. Moura, J. L. Stein, and H. K. Fathy, “Genetic identification and fisher identifiability analysis of the Doyle–Fuller–Newman model from experimental cycling of a LiFePO4 cell,” *Journal of Power Sources*, vol. 210, no. 0, pp. 263–275, 2012.

[82] X. Hu, S. Li, and H. Peng, “A comparative study of equivalent circuit models for Li-ion batteries,” *Journal of Power Sources*, vol. 198, pp. 359–367, 2012.

[83] Y. Kim, S. Mohan, J. Siegel, A. Stefanopoulou, and Y. Ding, "The estimation of temperature distribution in cylindrical battery cells under unknown cooling conditions," *Control Systems Technology, IEEE Transactions on*, vol. 22, no. 6, pp. 2277–2286, 2014.

[84] E. A. Wan and A. T. Nelson, "Dual Kalman Filtering methods for nonlinear prediction, smoothing, and estimation," in *In Advances in Neural Information Processing Systems 9*, 1997.

[85] M. C. VanDyke, J. L. Schwartz, and C. D. Hall, "Unscented Kalman filtering for spacecraft attitude state and parameter estimation," in *Proceedings of the 14th AAS/AIAA Space Flight Mechanics Meeting*, Feburary 2004, pp. 217–228.

[86] R. Li, M. Henson, and M. Kurtz, "Selection of model parameters for off-line parameter estimation," *Control Systems Technology, IEEE Transactions on*, vol. 12, no. 3, pp. 402–412, May 2004.

[87] P. Moraal and J. Grizzle, "Observer design for nonlinear systems with discrete-time measurements," *Automatic Control, IEEE Transactions on*, vol. 40, no. 3, pp. 395–404, Mar 1995.

[88] C. Jauffret, "Observability and fisher information matrix in nonlinear regression," *Aerospace and Electronic Systems, IEEE Transactions on*, vol. 43, no. 2, pp. 756–759, 2007.

[89] G. H. Dunteman, *Principal components analysis.* Sage, 1989, no. 69.

[90] Y. Kim, A. Salvi, A. Stefanopoulou, and T. Ersal, "Reducing soot emissions in a diesel series hybrid electric vehicle using a power rate constraint map," *Vehicular Technology, IEEE Transactions on*, vol. 64, no. 1, pp. 2–12, 2015.

[91] D. Aeyels, "On the number of samples necessary to achieve observability," *Systems & Control Letters*, vol. 1, no. 2, pp. 92 – 94, 1981.

[92] X. Hu, R. Xiong, and B. Egardt, "Model-based dynamic power assessment of lithium-ion batteries considering different operating conditions," *Industrial Informatics, IEEE Transactions on*, vol. 10, no. 3, pp. 1948–1959, Aug 2014.

[93] N. A. Samad, J. B. Siegel, and A. G. Stefanopoulou, "Parameterization and validation of a distributed coupled electro-thermal model for prismatic cells," in *ASME 2014 Dynamic Systems and Control Conference.* American Society of Mechanical Engineers, 2014, pp. V002T23A006–V002T23A006.

[94] W. Waag, S. Käbitz, and D. U. Sauer, "Experimental investigation of the lithium-ion battery impedance characteristic at various conditions and aging states and its influence on the application," *Applied Energy*, vol. 102, pp. 885–897, 2013.

[95] Y. Kim, S. Mohan, J. B. Siegel, A. G. Stefanopoulou, and Y. Ding, "The estimation of radial temperature distribution in cylindrical battery cells under unknown cooling conditions," in *IEEE Conference on Decision and Control*, Firenze, Italy, Dec 10-13 2013, pp. 5680–5685.

[96] Y.-H. Liu and Y.-F. Luo, "Search for an optimal rapid-charging pattern for li-ion batteries using the taguchi approach," *IEEE Trans. Ind. Electron.*, vol. 57, no. 12, pp. 3963–3971, Dec 2010.

[97] J. Jiang, Q. Liu, C. Zhang, and W. Zhang, "Evaluation of acceptable charging current of power li-ion batteries based on polarization characteristics," *IEEE Trans. Ind. Electron.*, vol. 61, no. 12, pp. 6844–6851, Dec 2014.

[98] J. Fan and S. Tan, "Studies on charging lithium-ion cells at low temperatures," *Journal of The Electrochemical Society*, vol. 153 (6), pp. A1081–A1092, 2006.

[99] S. Zhang, K. Xu, and T. Jow, "A new approach toward improved low temperature performance of li-ion battery," *Electrochemistry Communications*, vol. 4, no. 11, pp. 928 – 932, 2002.

[100] L.-R. Chen, S.-L. Wu, D.-T. Shieh, and T.-R. Chen, "Sinusoidal-ripple-current charging strategy and optimal charging frequency study for li-ion batteries," *IEEE Trans. Ind. Electron.*, vol. 60, no. 1, pp. 88–97, Jan 2013.

[101] M. Doyle, T. F. Fuller, and J. Newman, "Modeling of galvanostatic charge and discharge of the lithium/polymer/insertion cell," *Journal of Electrochemical Society*, vol. 140(6), pp. 1526–1533, 1993.

[102] W. Huang and J. Qahouq, "An online battery impedance measurement method using dc-dc power converter control," *IEEE Trans. Ind. Electron.*, vol. 61, no. 11, pp. 5987–5995, Nov 2014.

[103] L.-R. Chen, J.-J. Chen, C.-M. Ho, S.-L. Wu, and D.-T. Shieh, "Improvement of li-ion battery discharging performance by pulse and sinusoidal current strategies," *IEEE Trans. Ind. Electron.*, vol. 60, no. 12, pp. 5620–5628, Dec 2013.

[104] S. Burer and A. N. Letchford, "Non-convex mixed-integer nonlinear programming: A survey," *Surveys in Operations Research and Management Science*, vol. 17, no. 2, pp. 97 – 106, 2012. [Online]. Available: http://www.sciencedirect.com/science/article/pii/S1876735412000037

[105] R. Horst, "On the global minimization of concave functions," *Operations-Research-Spektrum*, vol. 6, no. 4, pp. 195–205, 1984. [Online]. Available: http://dx.doi.org/10.1007/BF01720068

[106] H. P. Benson and R. Horst, "A branch and bound-outer approximation algorithm for concave minimization over a convex set," *Computers & Mathematics with Applications*, vol. 21, no. 67, pp. 67 – 76, 1991. [Online]. Available: http://www.sciencedirect.com/science/article/pii/089812219190161V

[107] R. T. Rockafellar, *Convex analysis.* Princeton university press, 1997.

[108] The Idaho National Laboratory, *Battery Test Manual For Plug-In Hybrid Electric Vehicles*, 2nd ed., U.S. Department of Energy Vehicle Technologies Program, December 2010.

[109] C. Muller, D. E. Quevedo, and G. C. Goodwin, “How good is quantized model predictive control with horizon one?” *IEEE Trans. Autom. Control*, vol. 56, no. 11, pp. 2623–2638, 2011.

[110] F. H. Clarke and R. B. Vinter, “The relationship between the maximum principle and dynamic programming,” *SIAM Journal on Control and Optimization*, vol. 25, no. 5, pp. 1291–1311, 1987.

[111] P. Bettiol and R. B. Vinter, “Sensitivity interpretations of the costate variable for optimal control problems with state constraints,” *SIAM Journal on Control and Optimization*, vol. 48, no. 5, pp. 3297–3317, 2010.

[112] M. Korda, D. Henrion, and C. N. Jones, “Inner approximations of the region of attraction for polynomial dynamical systems,” *IFAC Proceedings Volumes*, vol. 46, no. 23, pp. 534–539, 2013.

[113] ——, “Convex computation of the maximum controlled invariant set for polynomial control systems,” *SIAM Journal on Control and Optimization*, vol. 52, no. 5, pp. 2944–2969, 2014.

[114] S. Mohan, V. Shia, and R. Vasudevan. (2016, January) Convex computation of the reachable set for hybrid systems with parametric uncertainty. Online, arxiv. ArXiv:1601.01019.

[115] M. Claeys and R. Sepulchre, “Reconstructing trajectories from the moments of occupation measures,” in *53rd IEEE Conference on Decision and Control*, Dec 2014, pp. 6677–6682.

[116] E. Anderson and P. Nash, *Linear programming in infinite-dimensional spaces: theory and applications*, ser. Wiley-Interscience series in discrete mathematics and optimization. Wiley, 1987. [Online]. Available: https://books.google.com/books?id=XGVRAAAAMAAJ

[117] P. A. Parrilo, “Structured semidefinite programs and semialgebraic geometry methods in robustness and optimization,” Ph.D. dissertation, Citeseer, 2000.